

---

# RAM-H1200: A Unified Evaluation and Dataset on Hand Radiographs for Rheumatoid Arthritis

---

Songxiao Yang<sup>1\*</sup> Haolin Wang<sup>2\*</sup> Yao Fu<sup>2\*</sup> Junmu Peng<sup>2</sup>  
 Lin Fan<sup>3</sup> Hongruixuan Chen<sup>4</sup> Jian Song<sup>4</sup> Masayuki Ikebe<sup>2</sup>  
 Shinya Takamaeda-Yamazaki<sup>4,5</sup> Masatoshi Okutomi<sup>1</sup> Tamotsu Kamishima<sup>2</sup> Yafei Ou<sup>4†</sup>

<sup>1</sup> Institute of Science Tokyo, Tokyo, Japan

<sup>2</sup> Hokkaido University, Sapporo, Japan


<sup>3</sup> Southwest Jiaotong University, Chengdu, China


<sup>4</sup> RIKEN, Tokyo, Japan

<sup>5</sup> The University of Tokyo, Tokyo, Japan

## Abstract

Rheumatoid arthritis (RA) assessment from hand radiographs requires multi-level analysis and modeling of anatomical structures and fine-grained local pathological changes. However, existing public resources do not support such unified multi-level analysis, often lacking full-hand coverage, fine-grained annotations, and consistent integration with clinical scoring systems. In particular, annotations that enable quantitative analysis of bone erosion (BE) remain scarce. RAM-H1200 contains 1,200 hand radiographs collected from six medical centers, with multi-level annotations including (i) whole-hand bone structure instance segmentation, (ii) pixel-level BE masks, (iii) SvdH-defined joint regions of interest, and (iv) joint-level SvdH scores for both BE and joint space narrowing (JSN). It is designed to evaluate whether models can jointly capture anatomical structure, localized erosive pathology, and clinically standardized RA severity from hand radiographs. The proposed BE masks enable, for the first time, quantitative BE analysis beyond coarse categorical grading by providing explicit spatial supervision for lesion extent and morphology. To our knowledge, RAM-H1200 is the first public large-scale benchmark that jointly supports whole-hand bone structure instance segmentation, pixel-level BE delineation, and clinically grounded joint-level SvdH scoring for both BE and JSN. Results across benchmark tasks show that anatomical modeling is substantially more mature than quantitative BE analysis: whole-hand bone segmentation achieves strong performance, whereas BE segmentation remains a major open challenge. By unifying anatomical structure modeling, quantitative lesion analysis, and clinically grounded SvdH scoring, RAM-H1200 provides a single benchmark for comprehensive RA analysis on hand radiographs.

 **Benchmark & Code:** [github.com/YSongxiao/RAM-H1200](https://github.com/YSongxiao/RAM-H1200)

 **Dataset Repository:** [huggingface.co/datasets/TokyoTechMagicYang/RAM-H1200-v1](https://huggingface.co/datasets/TokyoTechMagicYang/RAM-H1200-v1)

## 1 Introduction

Rheumatoid arthritis (RA) is a chronic autoimmune disease that frequently affects the small joints of the hands at an early stage, leading to progressive structural damage and functional impairment [55, 29, 59]. Hand radiographs remain a cornerstone for assessing disease severity and monitoring longitudinal progression in RA [1], where bone erosion (BE) and joint space narrowing (JSN) are widely recognized as key radiographic manifestations of structural damage [54, 50]. Clinically, these changes are commonly evaluated using standardized scoring systems such as the Sharp/van der

---

\*Equal Contribution.

†Corresponding Author: [yafei.ou@riken.jp](mailto:yafei.ou@riken.jp)

Table 1: Comparison between RAM-H1200 and publicly available hand/wrist radiograph datasets. **Ann/Img**: Annotations per image; **F**, **C**, and **UR** denote segmentation annotations; **BE** and **JSN** denote score annotations.

Dataset	Images (Ann/Img)		Age (Mean±SD)	Centers	Patients	Purpose	RA-related Annotation				
	Seg	Score					F	C	UR	BE	JSN
DHA [13]	-	1400 (1)	-	1	-	BAA					
MURA [51]	-	40561 (1)	-	1	12173	Abnormality					
RSNA Bone Age [16]	-	14236 (1)	10.59	2	-	BAA					
GRAZPEDWRI-DX [45]	20327 (2)	-	10.9	1	6091	Trauma					
RA2-DREAM [62]	-	674 (31)	-	-	562	RA				✓	✓
RAM-W600 [76]	618 (14)	800 (6)	49.86±20.26	6	388	RA		✓	✓	△	
RAM-H1200 (Ours)	1200 (30+3)	1200 (31)	57.70±13.76	6	291	RA	✓	✓	✓	✓	✓

**F**: Finger bones; **C**: Carpal and metacarpal bones; **UR**: Radius and ulna.

**BAA**: Bone Age Assessment;  $\triangle$ : Partially available annotation.

Heijde (SvdH) score [66]. Nevertheless, conventional evaluation of hand radiographs largely depends on expert-driven visual inspection, which is inherently subjective, labor-intensive, and prone to inter-observer variability [56], especially when identifying subtle or early-stage abnormalities. These limitations have motivated increasing efforts toward the development of automated computer-aided diagnosis (CAD) approaches [60, 27], aiming to provide more consistent, efficient, and sensitive assessment of pathological changes in hand imaging [69, 70, 47, 46, 71, 48].

Automated RA analysis from hand radiographs involves a hierarchical pipeline ranging from anatomical structure modeling to lesion quantification and clinically standardized scoring. At the anatomical level, accurate identification of individual hand bones provides the spatial foundation for localizing clinically relevant joints and cortical surfaces [11]. At the pathological level, pixel-level BE segmentation enables quantitative characterization of erosive lesions, including their location, extent, and morphology [73, 5]. At the clinical level, SvdH-based BE and JSN scoring summarize structural damage into standardized ordinal grades. These levels are closely connected: BE analysis depends on anatomical context because erosions predominantly occur near cortical margins and joint interfaces, while JSN assessment relies on the relative configuration of adjacent bones and joint geometry [54, 65, 43]. Therefore, comprehensive RA radiograph understanding requires jointly modeling anatomical structure, localized pathology, and clinically grounded scoring within a unified framework [42].

However, existing hand and wrist radiograph datasets provide limited support for this unified analysis paradigm [35]. As summarized in Table 1, large-scale hand or wrist radiograph datasets such as DHA [13], RSNA Bone Age [16], and MURA [51] mainly provide global labels or abnormality annotations, without fine-grained structural or pathological masks. Datasets with richer annotations, such as GRAZPEDWRI-DX [45], focus on trauma rather than RA. RA-specific datasets such as RA2-DREAM [62] provide joint-level severity scores but lack pixel-wise annotations, while RAM-W600 [76] includes segmentation and scoring annotations but is limited to the wrist region. Consequently, datasets that jointly provide full-hand coverage, RA-specific annotations, pixel-level masks, SvdH-based scoring, and multi-center data remain scarce [35].

This lack of comprehensive data support further compounds the inherent difficulty of RA radiograph analysis across multiple levels [10]. Hand bone segmentation requires distinguishing numerous small and overlapping anatomical structures in high-resolution radiographs. Building upon this, BE segmentation introduces additional complexity, as erosive lesions are often tiny, low-contrast, and easily confounded with normal anatomical variations, imaging noise, or projection artifacts [57, 67, 54, 8]. Furthermore, SvdH scoring requires translating these subtle and heterogeneous image patterns into clinically meaningful ordinal grades, where BE and JSN follow distinct visual cues but share the same anatomical basis [4]. In the absence of datasets that jointly support these interconnected tasks, models are forced to implicitly infer missing structural or pathological context, thereby amplifying error propagation across stages [49]. As a result, reliable RA assessment from hand radiographs remains challenging, particularly when attempting to bridge structure-aware modeling, lesion-level quantification, and clinically standardized scoring within a unified framework.

In this paper, we introduce **R**heumatoid **A**rthritis **M**odeling-**H**and 1200 (RAM-H1200), a multi-center evaluation and dataset for comprehensive RA analysis in hand radiographs, as illustrated in Fig. 1. RAM-H1200 contains 1,200 high-resolution hand radiographs collected from six medical

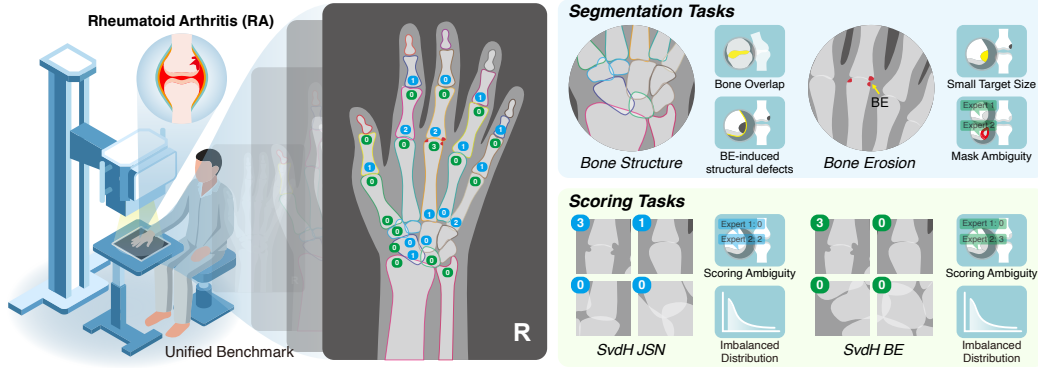


Figure 1: Overview of the proposed RAM-H1200 dataset. The dataset supports three hierarchically organized tasks: (i) hand bone structure modeling via instance-level segmentation, (ii) quantitative bone erosion (BE) analysis with pixel-level annotations, and (iii) standardized SvdH-based scoring for BE and joint space narrowing (JSN).

centers, covering diverse imaging conditions and patient populations. The dataset provides multi-level annotations, including instance-level segmentation masks for hand bone structures, pixel-level BE masks, and joint-level SvdH scores for both BE and JSN. This design enables systematic evaluation of RA radiograph analysis across anatomical, pathological, and clinical levels [58].

- **A unified multi-task evaluation and dataset for RA analysis:** RAM-H1200 establishes the first large-scale evaluation and dataset that systematically supports three hierarchically organized aspects of RA analysis: (i) **quantitative BE analysis**, representing the first attempt to explicitly model and evaluate bone erosion in a quantitative manner rather than through coarse grading; (ii) **hand bone structure modeling** via instance-level segmentation of the entire hand, providing the first systematic investigation of instance segmentation for all hand bone structures; and (iii) **standardized SvdH-based scoring** for both BE and JSN, forming a publicly available large-scale dataset for clinically grounded scoring. This unified design connects lesion-level quantification, structure-aware modeling, and clinical assessment.
- **Fine-grained and anatomically consistent annotations:** We provide high-quality pixel-level annotations for both anatomical structures and erosion regions across the hand, together with joint-level SvdH scores. The annotations are carefully designed to preserve anatomical consistency and support both local lesion analysis and global structural modeling.
- **A multi-task benchmark for evaluating RA radiograph analysis:** We construct a multi-task hierarchical analysis framework that integrates segmentation and joint-level scoring, evaluating distinct capabilities from anatomical structure modeling to lesion-level BE quantification and joint-level SvdH scoring. For each sub-task in the pipeline, we establish standardized benchmarks with unified evaluation metrics, enabling systematic evaluation and consistent cross-model comparison of intermediate task models.

## 2 Overview of Dataset

**Ethical Considerations** RAM-H1200 dataset is in compliance with the guidelines of the Declaration of Helsinki and obtained approval from the Ethics Committee of Hokkaido University (approval number: 24-104) and Institute of Science Tokyo (approval number: A24672). All radiographs included in this dataset were collected with informed consent for research use and public release.

### 2.1 Image and Annotation

The dataset consists of 1,200 hand posteroanterior projection (PA) radiographs from 241 patients with RA and 50 non-RA patients. The images were collected from six institutions in Sapporo, Japan: Hokkaido Medical Center for Rheumatic Diseases (HMCRD), Sapporo City General Hospital

(SCGH), Sagawa Akira Rheumatology Clinic (SARC), and three affiliated sites of Hokkaido University (HU1, HU2, and HU3). Each institution used its own CR system, and all data were managed in digital imaging and communications in medicine (DICOM) format. Imaging parameters are provided in Table 8 of Appendix C.3.

We applied standardized preprocessing procedures to ensure consistency across the dataset. All radiographs were resampled to a uniform spatial resolution of 0.175 mm/pixel. Furthermore, left-hand images were horizontally flipped to match right-hand orientation, providing a unified anatomical coordinate system for subsequent analysis. Annotation was performed by a dedicated team consisting of three radiological technologists and two clinically experienced experts, including a board-certified radiologist with 26 years of experience and an orthopedic doctor with 7 years of clinical practice. This multidisciplinary expertise ensured that the annotations were both medically accurate and clinically relevant. For segmentation tasks, initial contours were delineated by the radiological technologists. For score classification tasks, three radiological technologists and the orthopedic doctor participated in labeling. Each image was independently annotated by at least two annotators, and any discrepancies were resolved through discussion and consensus. All annotations were subsequently verified by the radiologist. Based on this protocol, the annotation comprised three principal components:

- **Bone Structure Annotation:** Precise contour delineation was performed for 30 anatomically defined structures spanning the entire hand, including the first to fifth proximal phalanges (PP1–5), middle phalanges (MP2–5), distal phalanges (DP1–5), metacarpals (MC1–5), and sesamoid bones (Ses). Carpal bones were annotated individually, including the trapezium (Tm), trapezoid (Td), scaphoid (Sca), lunate (Lu), capitate (Cap), hamate (Ham), and pisiform and triquetrum (Pis & Tri). In addition, the distal radius (Radius) and distal ulna (Ulna) were included. Surrounding soft tissue regions were also delineated to provide additional anatomical context for structure-aware analysis. A multi-label annotation strategy was implemented to independently mark each structure.
- **BE Annotation:** Pixel-level annotations were performed for BE regions across the hand. Following SvdH scoring principles, lesions were grouped into three categories by morphology and diagnostic certainty: high-confidence SvdH BE, moderate-confidence SvdH BE, and non-SvdH BE, referring to erosive patterns that are considered true bone erosion but do not fully meet the standard SvdH criteria.
- **SvdH-defined Joint ROIs for BE / JSN Scoring:** Anatomical locations for both BE and JSN were defined at the joint level following the SvdH scoring protocol, comprising 16 joints for BE assessment and 15 joints for JSN assessment. We performed ROI annotations on these areas.
- **SvdH BE / JSN Scoring Annotation:** Based on the predefined joint locations, SvdH scores for both BE and JSN were assigned at the joint level following the SvdH scoring protocol. Each joint was independently evaluated to quantify the severity of structural damage.

In addition, common external objects and imaging artifacts, such as rings, intravenous lines, and metallic implants, were annotated with pixel-level masks to reflect real-world clinical variability. These masks were excluded from the benchmark tasks and provided only for optional robust model development. Further details of data division and annotation are provided in Appendix C.

## 2.2 Statistics of RAM-H1200

We present statistical analyses of the RAM-H1200 dataset to characterize data sources, patient demographics, disease severity, longitudinal progression, and lesion distributions. Key attributes, including institutional distribution, age and gender, total SvdH scores, follow-up intervals, and lesion-level measurements, are summarized in Fig. 2. Fig. 2 (A) shows the institutional distribution of the dataset, which comprises 1,200 hand radiographs collected from six medical centers. Most samples originate from HMCRD and SARC, while the remaining centers provide smaller but complementary subsets, introducing variability in imaging conditions. Fig. 2 (B) and (C) illustrate the demographic and severity distributions. The cohort spans a wide age range, with most samples concentrated between 40 and 70 years old. The gender distribution is strongly skewed toward female patients, consistent with RA epidemiology. Total SvdH scores are dominated by low-to-moderate ranges, while high-severity cases are relatively limited. Fig. 2 (D) shows the relationship between adjacent follow-up intervals and radiographic progression ( $\Delta$ SvdH). Most intervals fall within 1–4 years, and progression

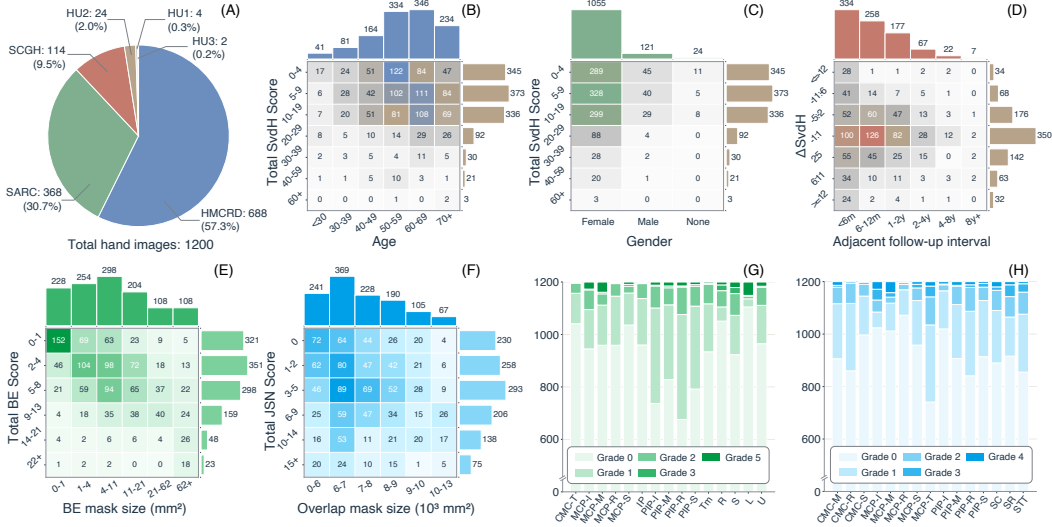


Figure 2: Distribution and Statistics for the RAM-H1200 dataset. (A) Data distribution by center. (B) Age vs. total SvdH score. (C) Gender vs. total SvdH score. (D) Adjacent follow-up interval vs. radiographic progression ( $\Delta$ SvdH). (E) BE mask size vs. total BE score (correlation: Spearman’s  $\rho = 0.532$ ,  $p < 0.001$ ). (F) Overlap mask size vs. total JSN score (correlation: Spearman’s  $\rho = 0.046$ ,  $p = 0.109$ ). (G) Joint-level BE score burden. (H) Joint-level JSN score burden. All analyses were performed at the hand-image level, treating left and right hands as independent samples.

values are concentrated around small changes, indicating generally slow and incremental disease progression. Fig. 2 (E) and (F) present lesion-level statistics. Larger BE mask sizes correspond to higher BE scores, and overlap regions increase with higher JSN scores, showing consistency between pixel-level annotations and clinical grading. We further assessed initial inter-annotator reliability before consensus discussion using the intraclass correlation coefficient (ICC), obtaining ICC(1,1) values of 0.5682 for BE, 0.4502 for JSN, and 0.5176 for the combined BE and JSN scores, broadly consistent with prior RA radiographic scoring studies [12]. Discrepant cases were then reviewed and resolved through consensus discussion to produce the final annotations, with detailed analysis provided in Table 10 in Appendix C.6. Fig. 2 (G) and (H) show joint-level score distributions. Most joints are assigned grade 0, while higher grades appear only in a small subset, resulting in a highly imbalanced distribution. Such skewed distributions are commonly reported in clinical cohorts [6, 24]. This pattern is consistent with prior observations that advances in medical care and early intervention have reduced the prevalence of late-stage RA, making high severity scores increasingly rare in modern cohorts [76].

### 3 Experiments and Benchmarks

**Experimental Setup** All experiments were conducted using patient-level train/validation/test splits to prevent data leakage across subsets. All models were trained using the AdamW optimizer with cosine annealing learning rate scheduling. Unless otherwise specified, the initial learning rate was set to  $1 \times 10^{-4}$ . Standard data augmentation techniques were applied during training. All experiments were conducted with a fixed random seed (2026) to ensure reproducibility. Training was performed on a server with four NVIDIA A100 40GB GPUs, while inference was carried out on an NVIDIA Quadro RTX 8000 GPU with 48GB memory. For segmentation tasks, we report Dice similarity coefficient (DSC), normalized surface Dice (NSD), volumetric overlap error (VOE), mean surface distance (MSD), recall (REC), and precision (PREC). For SvdH score classification, we report quadratic weighted kappa (QWK), mean absolute error (MAE), balanced accuracy (BACC), accuracy (ACC), within-one accuracy (W1-ACC), positive/negative sensitivity (P/N-SEN), and positive/negative accuracy (P/N-ACC). Task-specific implementation details are provided in Appendix E.

Table 2: Hand bone structure segmentation results obtained on the Test set. The best results in each column are highlighted in **bold**, and the second-best values are underlined.

Model	DSC (%)	NSD (%)	DSC <sub>O</sub> (%)	NSD <sub>O</sub> (%)	VOE (%)	MSD (pix)	#P (M)	Time (ms)
<b>Supervised Models</b>								
Unet [53]	96.37±2.68	90.41±5.82	73.71±7.77	73.12±10.78	6.44±3.74	2.85±2.98	7.94	325.21
Unet++ [79]	97.21±1.36	92.54±4.05	75.37±6.80	75.66±10.04	5.13±2.11	2.85±3.79	2.41	842.49
SegFormer [74]	96.65±1.48	89.85±4.40	71.59±6.63	69.39±9.70	6.13±2.10	2.51±1.64	21.88	272.00
TransUNet [7]	97.22±1.15	92.87±3.88	76.12±6.41	76.59±10.08	5.10±1.85	2.10±1.15	105.92	893.21
SwinUNETR [18]	<b>97.32±1.18</b>	93.07±3.96	<u>76.27±7.07</u>	77.04±10.49	<u>4.93±1.90</u>	<b>1.67±1.11</b>	25.14	748.16
UMambaEnc [39]	<b>97.32±1.32</b>	93.21±4.08	76.19±6.80	<u>77.06±10.22</u>	<u>4.93±2.08</u>	1.90±3.26	4.59	783.94
SwinUMamba [37]	97.31±1.23	<b>93.44±3.86</b>	<b>76.32±6.83</b>	<b>77.68±10.09</b>	<b>4.91±1.93</b>	<u>1.91±1.31</u>	59.89	1261.96
MambaVision [17]	96.41±1.35	87.10±4.48	66.43±5.93	60.87±8.97	6.61±2.02	2.16±1.33	62.43	1140.82
<b>Foundation Models</b>								
SAM(Box) [28]	90.76±2.51	78.01±4.72	5.90±3.37	4.24±3.03	13.93±3.07	4.05±1.22	641.09	1478.79
SAM(Point) [28]	75.45±9.21	59.18±8.81	3.44±1.72	2.89±2.05	34.34±9.91	39.68±29.82	641.09	1414.99
MedSAM(Box) [38]	80.61±4.42	33.52±8.37	10.81±4.74	7.79±3.37	30.95±5.99	10.33±2.10	93.74	839.35

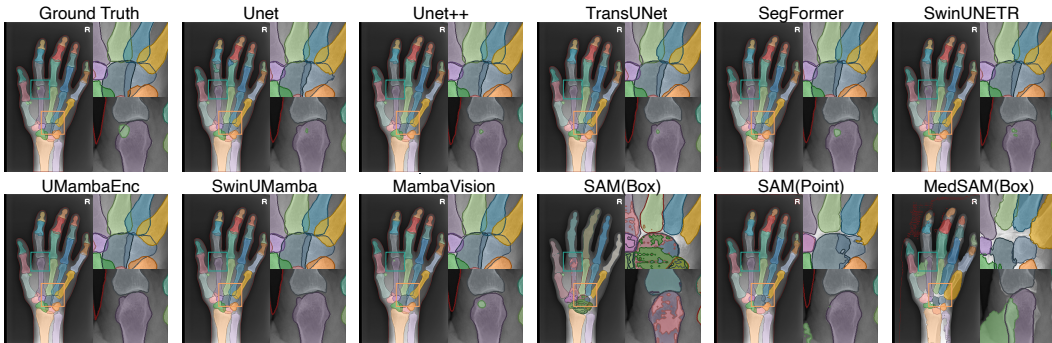


Figure 3: Hand bone structure segmentation visualization results.

### 3.1 Hand Bone Structure Segmentation

To better assess performance in anatomically overlapping regions, we additionally report overlap-aware metrics (DSC<sub>O</sub> and NSD<sub>O</sub>) following [76, 77], where evaluation is restricted to projection-induced bone overlap regions. As shown in Table 2, supervised models achieve consistently strong performance on hand bone structure segmentation, with DSC exceeding 96% for most architectures. Among them, SwinUMamba achieves the best overall results, obtaining the highest NSD (93.44%), DSC<sub>O</sub> (76.32%), and NSD<sub>O</sub> (77.68%), while SwinUNETR and UMambaEnc remain competitive across both region-based and boundary-aware metrics. Despite similar DSC scores, clearer differences emerge in overlap-aware metrics, indicating that the main challenge lies in anatomically complex regions rather than global localization. Projection overlap introduces ambiguous boundaries, making precise separation of adjacent bones difficult. This limitation is more pronounced for MambaVision and SegFormer, which show larger degradation in overlap regions. In contrast, foundation models such as SAM and MedSAM perform substantially worse across all metrics, suggesting that prompt-based segmentation is insufficient for accurate anatomical delineation. Qualitative results in Fig. 3 are consistent with these observations. While most supervised models produce anatomically coherent segmentations in non-overlapping regions, errors concentrate around bone junctions and overlap areas. Models with stronger overlap-aware performance, such as SwinUMamba and SwinUNETR, better preserve boundary continuity, whereas weaker models exhibit boundary inconsistency and missing fine structures. Foundation models show more severe failures, including coarse and fragmented masks. Detailed bone-wise results, overlap-region analyses, qualitative examples, and statistical evaluations are provided in Appendix F.1.

### 3.2 Hand BE Segmentation

As shown in Table 3, BE segmentation remains a highly challenging task, with all models achieving relatively low DSC scores (below 20%), reflecting the difficulty of detecting small and sparse

Table 3: Hand BE segmentation results obtained on the Test set. The best results in each column are highlighted in **bold**, and the second-best values are underlined.

Model	DSC (%)	NSD (%)	REC (%)	PREC (%)	VOE (%)	MSD (pix)	#P (M)	Time (ms)
Unet [53]	17.25±12.09	17.81±14.25	23.68±23.47	14.11±13.56	90.07±7.45	<b>182.17±121.50</b>	7.94	365.42
Unet++ [79]	17.57±12.93	17.61±14.30	23.22±23.54	14.37±13.94	89.79±8.26	196.17±116.29	2.41	772.82
nnUnet [23]	12.64±17.80	14.11±20.02	8.79±15.74	<b>23.50±31.57</b>	92.07±12.68	212.00±143.98	160.14	274.58
TransUNet [7]	<u>18.80±13.44</u>	18.51±14.81	<u>25.10±23.24</u>	14.92±14.97	<u>88.98±8.72</u>	190.06±124.17	105.32	849.10
SegFormer [74]	12.58±9.37	12.42±10.38	23.93±23.49	8.84±8.99	93.01±5.57	213.47±118.76	21.88	272.00
SwinUNETR [18]	15.57±10.77	15.34±12.46	24.97±23.89	11.69±11.48	91.19±6.45	211.72±118.84	25.14	826.32
UMambaEnc [39]	18.76±13.54	18.76±14.93	24.23±23.66	15.53±14.72	89.01±8.67	196.61±111.87	4.58	780.26
SwinUMamba [37]	<b>19.59±13.40</b>	<b>19.93±15.28</b>	<b>25.30±23.95</b>	<u>16.23±15.24</u>	<b>88.50±8.73</b>	<u>183.68±112.02</u>	59.89	1361.45

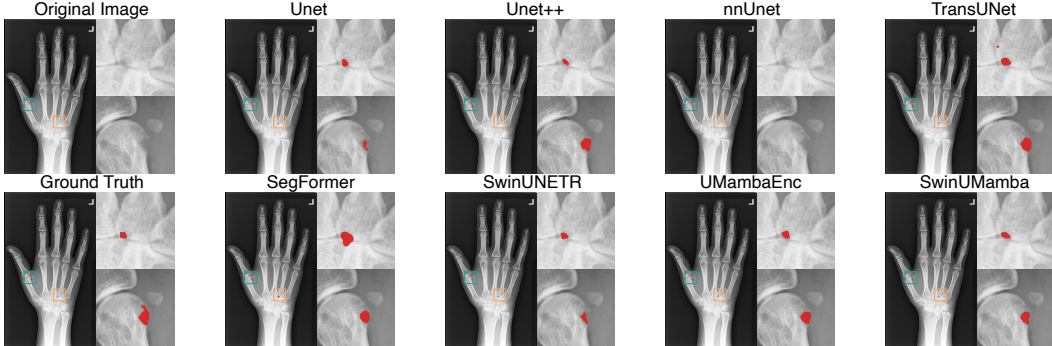


Figure 4: Hand BE segmentation visualization results.

lesion regions. Among the evaluated methods, SwinUMamba achieves the best overall performance, obtaining the highest DSC (19.59%), NSD (19.93%), and REC (25.30%), while TransUNet and UMambaEnc also show competitive results with comparable DSC and recall values. In contrast to bone structure segmentation, the performance gap between models is less pronounced, and improvements are limited across all metrics. Notably, nnUnet achieves the highest precision (23.50%) but suffers from extremely low recall (8.79%), indicating a conservative prediction behavior, whereas most other models show relatively higher recall but lower precision, reflecting a tendency to over-segment uncertain regions. These results suggest that BE segmentation is dominated by the trade-off between sensitivity and false positives, and that existing segmentation architectures struggle to simultaneously achieve accurate localization and reliable boundary delineation for small lesions. Qualitative analysis in Fig. 4 reveals three common failure patterns: (i) missed detections of small or low-contrast erosions, (ii) false positives around visually ambiguous cortical regions, and (iii) coarse or fragmented masks with imprecise boundaries. These errors reflect the intrinsic difficulty of BE segmentation, where lesions are tiny and sparse, boundaries are often unclear, and appearances vary with projection and local bone morphology. Annotation can also be subjective because lesion extent is not always sharply defined. Stronger models such as SwinUMamba and TransUNet show better sensitivity to small lesions, but still suffer from boundary imprecision and occasional over-segmentation, while weaker models such as SegFormer and nnUnet often miss lesions or produce unstable fragments. Overall, even the best models struggle to achieve both accurate localization and clean boundary delineation. Additional multi-class BE segmentation results, lesion-level analyses, and statistical evaluations are provided in Appendix F.2.

### 3.3 Scoring of SvdH BE

As shown in Table 4, SvdH BE score classification remains challenging, with all models showing limited ordinal agreement and balanced accuracy. MedMamba achieves the best overall agreement with the ground truth, obtaining the highest QWK (0.4522) and the strongest positive sensitivity (38.73%), while ResNet shows competitive performance with the best balanced accuracy (35.87%) and high within-one accuracy. DenseNet obtains the lowest MAE (0.3701) and the highest ACC (73.08%), but its relatively low positive sensitivity indicates a tendency to favor negative or low-score predictions. This discrepancy suggests that ACC alone can be misleading for BE scoring, since the label distribution is highly skewed toward low grades. The confusion matrices in Fig. 5 further

Table 4: SvdH BE score classification results obtained on the Test set. The best results in each column are highlighted in **bold**, and the second-best values are underlined.

Model	QWK	MAE	BACC (%)	ACC (%)	W1-ACC (%)	P/N-SEN (%)	P/N-ACC (%)	#P (M)	Time (ms)
ResNet [19]	0.4408	0.3904	<b>35.87</b>	69.71	92.81	<u>37.00</u>	73.78	21.28	0.25
DenseNet [22]	0.3905	<b>0.3701</b>	33.06	<b>73.08</b>	91.60	<u>15.77</u>	<u>75.12</u>	6.95	0.61
EfficientNetV2 [63]	0.3358	0.3937	30.67	71.30	91.71	23.48	74.11	20.18	0.63
MobileViT [41]	0.3920	0.4050	31.88	69.41	<b>92.25</b>	35.53	73.50	4.94	0.56
LeViT [14]	0.2346	0.4239	25.66	70.25	90.94	23.22	72.92	7.01	2.65
EfficientFormer [33]	0.3504	0.3951	27.32	70.46	<u>92.13</u>	25.22	73.97	3.25	0.54
ConvNeXtV2 [72]	0.3058	0.4127	28.15	70.04	91.39	22.62	72.87	27.87	1.13
MedMamba [78]	<b>0.4522</b>	0.3961	<u>34.91</u>	70.13	92.11	<b>38.73</b>	74.72	14.45	1.39
MambaVision [17]	0.3667	<u>0.3804</u>	30.59	<u>72.85</u>	91.15	17.94	<b>75.14</b>	31.16	0.73

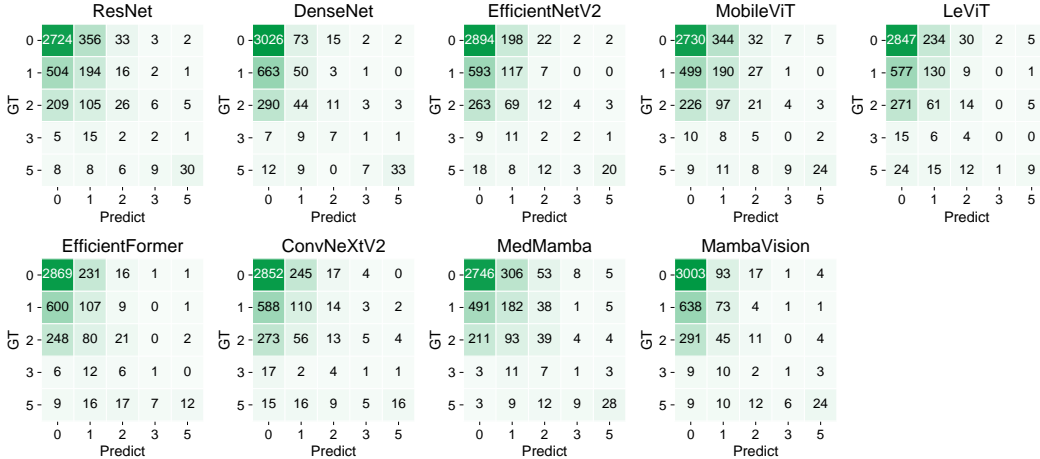


Figure 5: Confusion matrices for SvdH BE scoring across models.

show that predictions are concentrated at lower BE scores, with only partial diagonal alignment across severity levels. Higher-grade erosions are rarely predicted correctly, and many positive cases are shifted toward lower scores, reflecting the small, sparse, and visually ambiguous nature of BE lesions and the subjective boundaries between adjacent grades. Thus, beyond detecting erosion presence, estimating its progression level remains difficult. Overall, although several models achieve reasonable ACC and W1-ACC, their inconsistent BACC and P/N-SEN indicate that reliable BE scoring still requires better handling of subtle lesion patterns, ordinal severity, and severe class imbalance. Detailed joint-wise results, confusion-matrix analyses, and statistical evaluations are provided in Appendix F.3.

### 3.4 Scoring of SvdH JSN

As shown in Table 5, SvdH JSN score classification is relatively easier than BE scoring, but the overall performance is still not fully satisfactory. MobileViT achieves the best ordinal agreement and balanced classification performance, with the highest QWK (0.5967) and BACC (42.80%). EfficientFormer obtains the lowest MAE (0.2769), the highest ACC (76.75%), and the best P/N-ACC (80.97%), while ResNet also shows strong within-one accuracy (96.33%). These results suggest that the models can capture many coarse JSN patterns and often make predictions close to the ground truth. However, the gap between high ACC/W1-ACC and more moderate QWK/BACC indicates that correct fine-grained severity classification remains difficult. In addition, the variation in P/N-SEN across models shows that identifying positive JSN cases is still unstable under the imbalanced label distribution. The confusion matrices in Fig. 6 further support this observation. Most predictions are concentrated in the lower JSN scores, and many errors occur between neighboring grades rather than across distant classes. This explains the high W1-ACC, but it also shows that the models often struggle to make precise score-level decisions. Compared with BE, JSN changes are more structurally visible, so the overall agreement is better. Nevertheless, early narrowing remains difficult to grade: mild joint-space narrowing at scores 1–2 can be hard to distinguish by visual inspection, especially

Table 5: SvdH JSN score classification results obtained on the Test set. The best results in each column are highlighted in **bold**, and the second-best values are underlined.

Model	QWK	MAE	BACC (%)	ACC (%)	W1-ACC (%)	P/N-SEN (%)	P/N-ACC (%)	#P (M)	Time (ms)
ResNet [19]	0.5884	<u>0.2824</u>	39.51	76.03	<b>96.33</b>	46.32	80.37	21.28	0.31
DenseNet [22]	0.5829	0.3031	36.44	74.08	96.13	<b>48.13</b>	78.88	6.95	0.67
EfficientNetV2 [63]	<u>0.5393</u>	0.3011	32.83	75.43	95.18	41.45	80.15	20.18	0.71
MobileViT [41]	<b>0.5967</b>	0.2871	<b>42.80</b>	76.01	95.98	<u>46.89</u>	80.25	4.94	0.63
LeViT [14]	0.5445	0.3006	<u>40.62</u>	75.53	95.48	41.90	79.35	7.01	2.65
EfficientFormer [33]	<u>0.5919</u>	<b>0.2769</b>	39.25	<b>76.75</b>	<u>96.23</u>	45.53	<b>80.97</b>	3.25	0.56
ConvNeXtV2 [72]	0.5151	0.2941	32.51	<u>76.13</u>	95.36	32.50	79.95	27.87	1.16
MedMamba [78]	0.5738	0.2934	38.66	75.46	95.86	43.49	79.53	14.45	1.47
MambaVision [17]	0.5457	0.2899	34.62	76.01	95.88	44.05	<u>80.45</u>	31.16	0.80

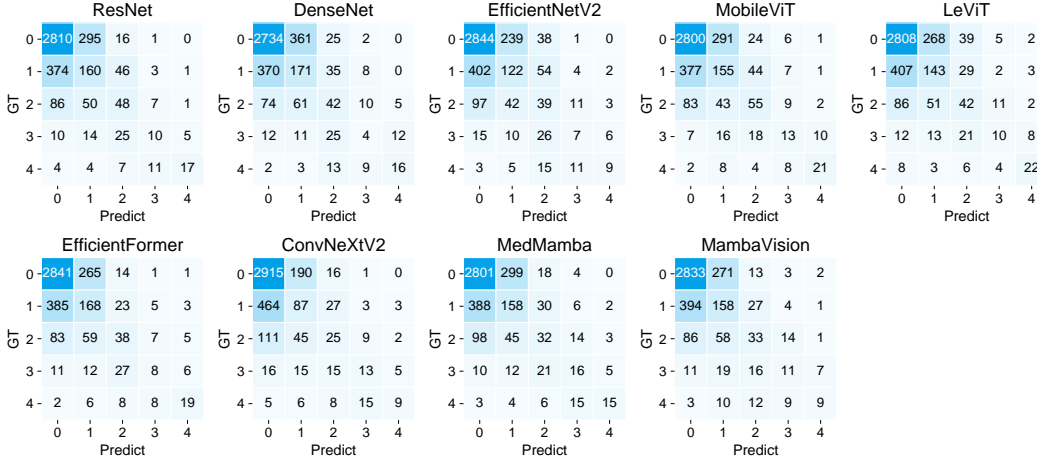


Figure 6: Confusion matrices for SvdH JSN scoring across models.

when the joint margins show slight irregularity. Moreover, the SvdH system requires fine-grained grading of narrowing severity from 0 to 4, which depends heavily on clinical reading experience and can introduce inter-observer variability. These factors make JSN progression difficult to model reliably, particularly for positive and higher-grade cases under class imbalance. Detailed joint-wise results, confusion-matrix analyses, and statistical evaluations are provided in Appendix F.4.

## 4 Conclusion and Limitations

In this paper, we introduced RAM-H1200, a large-scale multi-task benchmark for RA assessment from hand radiographs, extending prior wrist-focused studies to a comprehensive whole-hand setting. The dataset integrates three clinically relevant tasks and provides high-quality annotations at multiple levels, including hand bone structure segmentation, BE segmentation, and standardized SvdH-based scoring, enabling unified evaluation of both anatomical structure and pathological severity. Notably, this work represents one of the first attempts to explicitly formulate and benchmark quantitative BE analysis at scale, moving beyond coarse severity grading toward more fine-grained characterization of erosive progression. Benchmark results demonstrate that, although state-of-the-art models achieve strong performance in global hand bone segmentation, their performance degrades substantially in regions affected by bone overlap. In addition, the detection and segmentation of small, sparsely distributed erosive lesions remain particularly challenging [36]. Similarly, SvdH-based scoring continues to present significant difficulties, with overall performance still falling short of clinical applicability. These limitations are fundamentally associated with the intrinsic characteristics of RA pathology and radiographic imaging. In bone structure segmentation, projection-induced overlap in two-dimensional radiographs obscures critical anatomical boundaries, thereby increasing task complexity. For BE segmentation, lesions are typically small, irregular, and locally ambiguous, making consistent and precise annotation difficult even for experienced clinicians. Furthermore, the SvdH scoring system inherently relies on subjective assessment and involves relatively ambiguous grading boundaries, which further constrain annotation consistency and model robustness. These

challenges highlight the need for future research to incorporate structural priors, multi-scale modeling, and uncertainty-aware learning in order to improve robustness in subtle lesion scenarios while mitigating the impact of subjective annotation variability.

## References

- [1] Daniel Aletaha and Josef S Smolen. Diagnosis and management of rheumatoid arthritis: a review. *Jama*, 320(13):1360–1372, 2018.
- [2] Alix Bird, Lauren Oakden-Rayner, Katrina Chakradeo, Ranjey Thomas, Drishti Gupta, Suyash Jain, Rohan Jacob, Shonket Ray, Mihir D Wechalekar, Susanna Proudman, et al. Ai automated radiographic scoring in rheumatoid arthritis: Shedding light on barriers to implementation through comprehensive evaluation. In *Seminars in Arthritis and Rheumatism*, volume 74, page 152761. Elsevier, 2025.
- [3] Zhiyan Bo, Laura C Coates, and Bartłomiej W Papież. Deep learning models to automate the scoring of hand radiographs for rheumatoid arthritis. In *Annual Conference on Medical Image Understanding and Analysis*, pages 398–413. Springer, 2024.
- [4] S Boini and F Guillemain. Radiographic scoring methods as outcome measures in rheumatoid arthritis: properties and advantages. *Annals of the rheumatic diseases*, 60(9):817–827, 2001.
- [5] Camilo G Borrero, James M Mountz, and John D Mountz. Emerging mri methods in rheumatoid arthritis. *Nature Reviews Rheumatology*, 7(2):85–95, 2011.
- [6] Karin Bruynesteyn, Désirée van der Heijde, Maarten Boers, Ariane Saudan, Paul Peloso, Harold Paulus, Harry Houben, Bridget Griffiths, John Edmonds, Barry Bresnihan, et al. Determination of the minimal clinically important difference in rheumatoid arthritis joint damage of the sharp/van der heijde and larsen/scott scoring methods by clinical experts and comparison with the smallest detectable difference. *Arthritis & Rheumatism: Official Journal of the American College of Rheumatology*, 46(4):913–920, 2002.
- [7] Jieneng Chen, Yongyi Lu, Qihang Yu, Xiangde Luo, Ehsan Adeli, Yan Wang, Le Lu, Alan L Yuille, and Yuyin Zhou. Transunet: Transformers make strong encoders for medical image segmentation. *arXiv preprint arXiv:2102.04306*, 2021.
- [8] Uffe Møller Døhn, Bo J Ejbjerg, Maria Hasselquist, Eva Narvestad, Jakob Møller, Henrik S Thomsen, and Mikkel Østergaard. Detection of bone erosions in rheumatoid arthritis wrist joints with magnetic resonance imaging, computed tomography and radiography. *Arthritis research & therapy*, 10(1):R25, 2008.
- [9] Hongbo Du, Hai Wang, Chunlai Yang, Luyando Kabalata, Henian Li, and Changfu Qiang. Hand bone extraction and segmentation based on a convolutional neural network. *Biomedical Signal Processing and Control*, 89:105788, 2024.
- [10] Bo Ejbjerg, Eva Narvestad, Egill Rostrup, Marcin Szkudlarek, Søren Jacobsen, Henrik S Thomsen, and Mikkel Østergaard. Magnetic resonance imaging of wrist and finger joints in healthy subjects occasionally shows changes resembling erosions and synovitis as seen in rheumatoid arthritis. *Arthritis & Rheumatism: Official Journal of the American College of Rheumatology*, 50(4):1097–1106, 2004.
- [11] Emilio Filippucci, Luca Di Geso, and Walter Grassi. Progress in imaging in rheumatology. *Nature Reviews Rheumatology*, 10(10):628–634, 2014.
- [12] Motoshi Fujimori, Tamotsu Kamishima, Masaru Kato, Yumika Seno, Kenneth Sutherland, Hiroyuki Sugimori, Mutsumi Nishida, and Tatsuya Atsumi. Composite assessment of power doppler ultrasonography and mri in rheumatoid arthritis: a pilot study of predictive value in radiographic progression after one year. *The British Journal of Radiology*, 91(1086):20170748, 2018.
- [13] Arkadiusz Gertych, Aifeng Zhang, James Sayre, Sylwia Pospiech-Kurkowska, and HK Huang. Bone age assessment of children using a digital hand atlas. *Computerized medical imaging and graphics*, 31(4-5):322–331, 2007.

- [14] Benjamin Graham, Alaaeldin El-Nouby, Hugo Touvron, Pierre Stock, Armand Joulin, Hervé Jégou, and Matthijs Douze. Levit: a vision transformer in convnet’s clothing for faster inference. In *Proceedings of the IEEE/CVF international conference on computer vision*, pages 12259–12269, 2021.
- [15] Lilla Gunkl-Tóth, Iain B McInnes, and György Nagy. Bridging the gap: combining treat-to-target and difficult-to-treat strategies in the management of rheumatoid arthritis. *Nature Reviews Rheumatology*, pages 1–9, 2026.
- [16] Safwan S Halabi, Luciano M Prevedello, Jayashree Kalpathy-Cramer, Artem B Mamonov, Alexander Bilbily, Mark Cicero, Ian Pan, Lucas Araújo Pereira, Rafael Teixeira Sousa, Nitamar Abdala, et al. The rsna pediatric bone age machine learning challenge. *Radiology*, 290(2):498–503, 2019.
- [17] Ali Hatamizadeh and Jan Kautz. Mambavision: A hybrid mamba-transformer vision backbone. In *Proceedings of the Computer Vision and Pattern Recognition Conference*, pages 25261–25270, 2025.
- [18] Ali Hatamizadeh, Vishwesh Nath, Yucheng Tang, Dong Yang, Holger R Roth, and Daguang Xu. Swin unetr: Swin transformers for semantic segmentation of brain tumors in mri images. In *International MICCAI brainlesion workshop*, pages 272–284. Springer, 2021.
- [19] Kaiming He, Xiangyu Zhang, Shaoqing Ren, and Jian Sun. Deep residual learning for image recognition. In *Proceedings of the IEEE conference on computer vision and pattern recognition*, pages 770–778, 2016.
- [20] Yuri Hioki, Koji Makino, Kensuke Koyama, Hirotaka Haro, and Hidetsugu Terada. Evaluation method of rheumatoid arthritis by the x-ray photograph using deep learning. In *2021 IEEE 3rd Global Conference on Life Sciences and Technologies (LifeTech)*, pages 444–447. IEEE, 2021.
- [21] Toru Hirano, Masayuki Nishide, Naoki Nonaka, Jun Seita, Kosuke Ebina, Kazuhiro Sakurada, and Atsushi Kumanogoh. Development and validation of a deep-learning model for scoring of radiographic finger joint destruction in rheumatoid arthritis. *Rheumatology advances in practice*, 3(2):rkz047, 2019.
- [22] Gao Huang, Zhuang Liu, Laurens Van Der Maaten, and Kilian Q Weinberger. Densely connected convolutional networks. In *Proceedings of the IEEE conference on computer vision and pattern recognition*, pages 4700–4708, 2017.
- [23] Fabian Isensee, Paul F Jaeger, Simon AA Kohl, Jens Petersen, and Klaus H Maier-Hein. nnu-net: a self-configuring method for deep learning-based biomedical image segmentation. *Nature methods*, 18(2):203–211, 2021.
- [24] LMA Jansen, IE Van der Horst-Bruinsma, D Van Schaardenburg, PD Bezemer, and BAC Dijkmans. Predictors of radiographic joint damage in patients with early rheumatoid arthritis. *Annals of the rheumatic diseases*, 60(10):924–927, 2001.
- [25] Bo-kyeong Kang, Yelin Han, Jaehoon Oh, Jongwoo Lim, Jongbin Ryu, Myeong Seong Yoon, Juncheol Lee, and Soorack Ryu. Automatic segmentation for favourable delineation of ten wrist bones on wrist radiographs using convolutional neural network. *Journal of Personalized Medicine*, 12(5):776, 2022.
- [26] JA Kauffman, Cornelis H Slump, and HJ Bernelot Moens. Segmentation of radiographs of hands with joint damage using customized active appearance models. In *15th Annual Workshop on Circuits, Systems and Signal Processing, ProRisc 2004*, 2004.
- [27] Kathryn M Kingsmore, Christopher E Puglisi, Amrie C Grammer, and Peter E Lipsky. An introduction to machine learning and analysis of its use in rheumatic diseases. *Nature Reviews Rheumatology*, 17(12):710–730, 2021.
- [28] Alexander Kirillov, Eric Mintun, Nikhila Ravi, Hanzi Mao, Chloe Rolland, Laura Gustafson, Tete Xiao, Spencer Whitehead, Alexander C Berg, Wan-Yen Lo, et al. Segment anything. In *Proceedings of the IEEE/CVF international conference on computer vision*, pages 4015–4026, 2023.

- [29] Noriko Komatsu and Hiroshi Takayanagi. Mechanisms of joint destruction in rheumatoid arthritis—immune cell–fibroblast–bone interactions. *Nature Reviews Rheumatology*, 18(7):415–429, 2022.
- [30] Georg Langs, Philipp Peloschek, Horst Bischof, and Franz Kainberger. Model-based erosion spotting and visualization in rheumatoid arthritis. *Academic radiology*, 14(10):1179–1188, 2007.
- [31] Georg Langs, Philipp Peloschek, Horst Bischof, and Franz Kainberger. Automatic quantification of joint space narrowing and erosions in rheumatoid arthritis. *IEEE transactions on medical imaging*, 28(1):151–164, 2008.
- [32] Hyungeun Lee, Ung Hwang, Seungwon Yu, Chang-Hun Lee, and Kijung Yoon. Osteoporosis prediction from hand and wrist x-rays using image segmentation and self-supervised learning. *arXiv preprint arXiv:2311.06834*, 2023.
- [33] Yanyu Li, Geng Yuan, Yang Wen, Ju Hu, Georgios Evangelidis, Sergey Tulyakov, Yanzhi Wang, and Jian Ren. Efficientformer: Vision transformers at mobilenet speed. *Advances in Neural Information Processing Systems*, 35:12934–12949, 2022.
- [34] Chung-Yueh Lien, Hao-Jan Wang, Cheng-Kai Lu, Tzu-Hsuan Hsu, Woei-Chyn Chu, and Chien-Chih Lai. Deep learning with an attention mechanism for enhancing automated modified total sharp/van der heijde scoring of hand x-ray images in rheumatoid arthritis. *Journal of Medical and Biological Engineering*, pages 1–9, 2025.
- [35] Chung MA Lin, Faye AH Cooles, and John D Isaacs. Precision medicine: the precision gap in rheumatic disease. *Nature Reviews Rheumatology*, 18(12):725–733, 2022.
- [36] Tsung-Yi Lin, Priya Goyal, Ross Girshick, Kaiming He, and Piotr Dollár. Focal loss for dense object detection. In *Proceedings of the IEEE international conference on computer vision*, pages 2980–2988, 2017.
- [37] Jiarun Liu, Hao Yang, Hong-Yu Zhou, Yan Xi, Lequan Yu, Cheng Li, Yong Liang, Guangming Shi, Yizhou Yu, Shaoting Zhang, et al. Swin-umamba: Mamba-based unet with imagenet-based pretraining. In *International Conference on Medical Image Computing and Computer-Assisted Intervention*, pages 615–625. Springer, 2024.
- [38] Jun Ma, Yuting He, Feifei Li, Lin Han, Chenyu You, and Bo Wang. Segment anything in medical images. *Nature Communications*, 15:654, 2024.
- [39] Jun Ma, Feifei Li, and Bo Wang. U-mamba: Enhancing long-range dependency for biomedical image segmentation. *arXiv preprint arXiv:2401.04722*, 2024.
- [40] Krzysztof Maziarz, Anna Krason, and Zbigniew Wojna. Deep learning for rheumatoid arthritis: Joint detection and damage scoring in x-rays. *arXiv preprint arXiv:2104.13915*, 2021.
- [41] Sachin Mehta and Mohammad Rastegari. Mobilevit: light-weight, general-purpose, and mobile-friendly vision transformer. *arXiv preprint arXiv:2110.02178*, 2021.
- [42] Ioanna Minopoulou, Arnd Kleyer, Melek Yalcin-Mutlu, Filippo Fagni, Stefan Kemenes, Christian Schmidkonz, Armin Atzinger, Milena Pachowsky, Klaus Engel, Lukas Folle, et al. Imaging in inflammatory arthritis: progress towards precision medicine. *Nature Reviews Rheumatology*, 19(10):650–665, 2023.
- [43] Kazuki Miyama, Ryoma Bise, Satoshi Ikemura, Kazuhiro Kai, Masaya Kanahori, Shinkichi Arisumi, Taisuke Uchida, Yasuharu Nakashima, and Seiichi Uchida. Deep learning-based automatic-bone-destruction-evaluation system using contextual information from other joints. *Arthritis Research & Therapy*, 24(1):227, 2022.
- [44] Seiichi Murakami, Kazuhiro Hatano, JooKooi Tan, Hyoungeop Kim, and Takatoshi Aoki. Automatic identification of bone erosions in rheumatoid arthritis from hand radiographs based on deep convolutional neural network. *Multimedia tools and applications*, 77(9):10921–10937, 2018.

- [45] Eszter Nagy, Michael Janisch, Franko Hržić, Erich Sorantin, and Sebastian Tschauner. A pediatric wrist trauma x-ray dataset (grazpedwri-dx) for machine learning. *Scientific data*, 9(1):222, 2022.
- [46] Yafei Ou, Prasoon Ambalathankandy, Ryunosuke Furuya, Seiya Kawada, Tianyu Zeng, Yujie An, Tamotsu Kamishima, Kenichi Tamura, and Masayuki Ikebe. A sub-pixel accurate quantification of joint space narrowing progression in rheumatoid arthritis. *IEEE Journal of Biomedical and Health Informatics*, 27(1):53–64, 2022.
- [47] Yafei Ou, Prasoon Ambalathankandy, Takeshi Shimada, Tamotsu Kamishima, and Masayuki Ikebe. Automatic radiographic quantification of joint space narrowing progression in rheumatoid arthritis using poc. In *2019 IEEE 16th International Symposium on Biomedical Imaging (ISBI 2019)*, pages 1183–1187. IEEE, 2019.
- [48] Yafei Ou, Wahyu Rahmaniari, Dichao Liu, Hiroko Oshibe, Ze Jin, Tamotsu Kamishima, and Kenji Suzuki. Computer-aided diagnosis and monitoring of rheumatoid arthritis in conventional radiography: Advancements and future opportunities. In *Artificial Intelligence in Diagnostics and Imaging Technologies in Healthcare: In honour of Professor Dr. George A. Tsibrantzis for his Invaluable Contributions*, pages 137–154. Springer, 2025.
- [49] Aridaman Pandit and Timothy RDJ Radstake. Machine learning in rheumatology approaches the clinic. *Nature Reviews Rheumatology*, 16(2):69–70, 2020.
- [50] Raj Ponnusamy, Ming Zhang, Zhiheng Chang, Yue Wang, Carmine Guida, Samantha Kuang, Xinyue Sun, Jordan Blackadar, Jeffrey B Driban, Timothy McAlindon, et al. Automatic measuring of finger joint space width on hand radiograph using deep learning and conventional computer vision methods. *Biomedical signal processing and control*, 84:104713, 2023.
- [51] Pranav Rajpurkar, Jeremy Irvin, Aarti Bagul, Daisy Ding, Tony Duan, Hershel Mehta, Brandon Yang, Kaylie Zhu, Dillon Laird, Robyn L Ball, et al. Mura: Large dataset for abnormality detection in musculoskeletal radiographs. *arXiv preprint arXiv:1712.06957*, 2017.
- [52] Janick Rohrbach, Tobias Reinhard, Beate Sick, and Oliver Dürr. Bone erosion scoring for rheumatoid arthritis with deep convolutional neural networks. *Computers & Electrical Engineering*, 78:472–481, 2019.
- [53] Olaf Ronneberger, Philipp Fischer, and Thomas Brox. U-net: Convolutional networks for biomedical image segmentation. In *Medical image computing and computer-assisted intervention—MICCAI 2015: 18th international conference, Munich, Germany, October 5-9, 2015, proceedings, part III 18*, pages 234–241. Springer, 2015.
- [54] Georg Schett and Ellen Gravallese. Bone erosion in rheumatoid arthritis: mechanisms, diagnosis and treatment. *Nature Reviews Rheumatology*, 8(11):656–664, 2012.
- [55] Kassem Sharif, Alaa Sharif, Fareed Jumah, Rod Oskouian, and R Shane Tubbs. Rheumatoid arthritis in review: Clinical, anatomical, cellular and molecular points of view. *Clinical Anatomy*, 31(2):216–223, 2018.
- [56] John T Sharp, Frederick Wolfe, Marissa Lassere, Maarten Boers, Désirée Van Der Heijde, Arvi Larsen, Harold Paulus, Rolf Rau, and Vibeke Strand. Variability of precision in scoring radiographic abnormalities in rheumatoid arthritis by experienced readers. *The Journal of rheumatology*, 31(6):1062–1072, 2004.
- [57] John T Sharp, Donald Y Young, Gilbert B Bluhm, Andrew Brook, Anne C Brower, Mary Corbett, John L Decker, Harry K Genant, J Philip Gofton, Neal Goodman, et al. How many joints in the hands and wrists should be included in a score of radiologic abnormalities used to assess rheumatoid arthritis? *Arthritis & Rheumatism: Official Journal of the American College of Rheumatology*, 28(12):1326–1335, 1985.
- [58] Josef S Smolen and Daniel Aletaha. Rheumatoid arthritis therapy reappraisal: strategies, opportunities and challenges. *Nature Reviews Rheumatology*, 11(5):276–289, 2015.

- [59] Josef S. Smolen, Daniel Aletaha, Anne Barton, Gerd R. Burmester, Paul Emery, Gary S. Firestein, Arthur Kavanaugh, Iain B. McInnes, Daniel H. Solomon, Vibeke Strand, and Kazuhiko Yamamoto. Rheumatoid arthritis. *Nature Reviews Disease Primers*, 4(1):18001, 2018.
- [60] Berend C Stoel, Marius Staring, Monique Reijniere, and Annette HM van der Helm-van Mil. Deep learning in rheumatological image interpretation. *Nature Reviews Rheumatology*, 20(3):182–195, 2024.
- [61] Alexander Stolpovsky, Elizaveta Dakhova, Polina Druzhinina, Polina Postnikova, Daniil Kudinsky, Alexander Smirnov, Anastasia Sukhinina, Alexander Lila, and Anvar Kurmukov. Rheumavit: Transformer-based model for automated scoring of hand joints in rheumatoid arthritis. In *Proceedings of the IEEE/CVF International Conference on Computer Vision*, pages 2522–2531, 2023.
- [62] Dongmei Sun, Thanh M Nguyen, Robert J Allaway, Jelai Wang, Verena Chung, Thomas V Yu, Michael Mason, Isaac Dimitrovsky, Lars Ericson, Hongyang Li, et al. A crowdsourcing approach to develop machine learning models to quantify radiographic joint damage in rheumatoid arthritis. *JAMA network open*, 5(8):e2227423–e2227423, 2022.
- [63] Mingxing Tan and Quoc Le. Efficientnetv2: Smaller models and faster training. In *International conference on machine learning*, pages 10096–10106. PMLR, 2021.
- [64] Hans Henrik Thodberg. Hands-on experience with active appearance models. In *Medical Imaging 2002: Image Processing*, volume 4684, pages 495–506. SPIE, 2002.
- [65] Desiree MFM Van der Heijde. Plain x-rays in rheumatoid arthritis: overview of scoring methods, their reliability and applicability. *Bailliere’s clinical rheumatology*, 10(3):435–453, 1996.
- [66] DMFM Van der Heijde. How to read radiographs according to the sharp/van der heijde method. *The Journal of rheumatology*, 27(1):261–263, 2000.
- [67] Richard J Wakefield, Wayne W Gibbon, Philip G Conaghan, Philip O’Connor, Dennis McGonagle, Colin Pease, Michael J Green, Douglas J Veale, John D Isaacs, and Paul Emery. The value of sonography in the detection of bone erosions in patients with rheumatoid arthritis: a comparison with conventional radiography. *Arthritis & Rheumatism*, 43(12):2762–2770, 2000.
- [68] Hao-Jan Wang, Chi-Ping Su, Chien-Chih Lai, Wun-Rong Chen, Chi Chen, Liang-Ying Ho, Woei-Chyn Chu, and Chung-Yueh Lien. Deep learning-based computer-aided diagnosis of rheumatoid arthritis with hand x-ray images conforming to modified total sharp/van der heijde score. *Biomedicines*, 10(6):1355, 2022.
- [69] Haolin Wang, Yafei Ou, Prasoon Ambalathankandy, Gen Ota, Pengyu Dai, Masayuki Ikebe, Kenji Suzuki, and Tamotsu Kamishima. Bls-gan: A deep layer separation framework for eliminating bone overlap in conventional radiographs. In *Proceedings of the AAAI Conference on Artificial Intelligence*, volume 39, pages 7674–7681, 2025.
- [70] Haolin Wang, Yafei Ou, Prasoon Ambalathankandy, Gen Ota, Pengyu Dai, Masayuki Ikebe, Kenji Suzuki, and Tamotsu Kamishima. Layer separation: Towards adjustable joint space width images synthesis. In *Proceedings of the 33rd ACM International Conference on Multimedia*, pages 8273–8282, 2025.
- [71] Haolin Wang, Yafei Ou, Wanxuan Fang, Prasoon Ambalathankandy, Naoto Goto, Gen Ota, Taichi Okino, Jun Fukae, Kenneth Sutherland, Masayuki Ikebe, et al. A deep registration method for accurate quantification of joint space narrowing progression in rheumatoid arthritis. *Computerized Medical Imaging and Graphics*, 108:102273, 2023.
- [72] Sanghyun Woo, Shoubhik Debnath, Ronghang Hu, Xinlei Chen, Zhuang Liu, In So Kweon, and Saining Xie. Convnext v2: Co-designing and scaling convnets with masked autoencoders. In *Proceedings of the IEEE/CVF conference on computer vision and pattern recognition*, pages 16133–16142, 2023.

- [73] Thasia G Woodworth, Olga Morgacheva, Olga L Pimienta, Orrin M Troum, Veena K Ranganath, and Daniel E Furst. Examining the validity of the rheumatoid arthritis magnetic resonance imaging score according to the omeract filter—a systematic literature review. *Rheumatology*, 56(7):1177–1188, 2017.
- [74] Enze Xie, Wenhai Wang, Zhiding Yu, Anima Anandkumar, Jose M Alvarez, and Ping Luo. Segformer: Simple and efficient design for semantic segmentation with transformers. *Advances in neural information processing systems*, 34:12077–12090, 2021.
- [75] Fan Yang, Xin Weng, Yuehong Miao, Yuhui Wu, Hong Xie, and Pinggui Lei. Deep learning approach for automatic segmentation of ulna and radius in dual-energy x-ray imaging. *Insights into Imaging*, 12:1–9, 2021.
- [76] Songxiao Yang, Haolin Wang, Yao Fu, Ye Tian, Tamotsu Kamishima, Masayuki Ikebe, Yafei Ou, and Masatoshi Okutomi. Ram-w600: A multi-task wrist dataset and benchmark for rheumatoid arthritis. In *Advances in Neural Information Processing Systems 38 (NeurIPS 2025)*, 2025.
- [77] Songxiao Yang, Haolin Wang, Masayuki Ikebe, Tamotsu Kamishima, Yafei Ou, and Okutomi Masatoshi. Ap-dpm: A dual-path merging network via adversarial anatomical prior guidance for wrist bone segmentation. In *2025 IEEE International Conference on Bioinformatics and Biomedicine (BIBM)*, pages 4335–4340. IEEE, 2025.
- [78] Yubiao Yue and Zhenzhang Li. Medmamba: Vision mamba for medical image classification. *arXiv preprint arXiv:2403.03849*, 2024.
- [79] Zongwei Zhou, Md Mahfuzur Rahman Siddiquee, Nima Tajbakhsh, and Jianming Liang. Unet++: A nested u-net architecture for medical image segmentation. In *Deep learning in medical image analysis and multimodal learning for clinical decision support: 4th international workshop, DLMIA 2018, and 8th international workshop, ML-CDS 2018, held in conjunction with MICCAI 2018, Granada, Spain, September 20, 2018, proceedings 4*, pages 3–11. Springer, 2018.

## A RAM-H1200 Data Access and Format

The data can be accessed on HuggingFace at <https://huggingface.co/datasets/TokyoTechMagicYang/ram-h1200-v1>. The benchmark and code can be accessed on GitHub at <https://github.com/YSongxiao/ram-h1200>.

The dataset is organised into two main components (Segmentation/ and SvdH\_Scoring/), corresponding to segmentation and SvdH scoring related tasks, respectively. The dataset structure is shown as follows:

```
RAM-H1200-v1/
|-- Segmentation/
|   |-- train/
|   |   |-- JP_HMCRD_P0001_20210203_6791_L.bmp
|   |   |-- JP_HMCRD_P0001_20210203_6791_R.bmp
|   |   |-- ...
|   |   |-- _annotations_bone_rle.coco.json # COCO annotations for
|   |   ↪ bone segmentation
|   |   |-- _annotations_be_rle.coco.json # COCO annotations for
|   |   ↪ bone erosion segmentation
|   |-- val/
|   |   |-- JP_HMCRD_P0026_20201122_5221_L.bmp
|   |   |-- JP_HMCRD_P0026_20201122_5221_R.bmp
|   |   |-- ...
|   |   |-- _annotations_bone_rle.coco.json
|   |   |-- _annotations_be_rle.coco.json
|   |-- test/
|   |   |-- JP_HMCRD_P0007_20140629_6951_L.bmp
|   |   |-- JP_HMCRD_P0007_20140629_6951_R.bmp
|   |   |-- ...
|   |   |-- _annotations_bone_rle.coco.json
|   |   |-- _annotations_be_rle.coco.json
|-- SvdH_Scoring/
|   |-- SvdH_BE_Scoring/
|   |   |-- train/
|   |   |   |-- JP_HMCRD_P0001_20210203_6791_L/
|   |   |   |   |-- CMC-T.bmp
|   |   |   |   |-- IP.bmp
|   |   |   |   |-- L.bmp
|   |   |   |   |-- MCP-I.bmp
|   |   |   |   |-- ...
|   |   |   |-- ...
|   |   |   |-- _annotations_be_joint_detection.coco.json
|   |   |   |-- _annotation_be_scores.json
|   |   |-- val/
|   |   |   |-- ...
|   |   |   |-- _annotations_be_joint_detection.coco.json
|   |   |   |-- _annotation_be_scores.json
|   |   |-- test/
|   |   |   |-- ...
|   |   |   |-- _annotations_be_joint_detection.coco.json
|   |   |   |-- _annotation_be_scores.json
|   |-- SvdH_JSN_Scoring/
|   |   |-- train/
|   |   |   |-- JP_HMCRD_P0001_20210203_6791_L/
|   |   |   |   |-- CMC-M.bmp
|   |   |   |   |-- CMC-R.bmp
|   |   |   |   |-- CMC-S.bmp
|   |   |   |   |-- MCP-I.bmp
|   |   |   |   |-- ...
|   |   |   |-- ...
|   |   |   |-- _annotations_jsn_joint_detection.coco.json
|   |   |   |-- _annotation_jsn_scores.json
|   |   |-- val/
|   |   |   |-- ...
```

```

|-- _annotations_jsn_joint_detection.coco.json
|-- _annotation_jsn_scores.json
|-- test/
|-- ...
|-- _annotations_jsn_joint_detection.coco.json
|-- _annotation_jsn_scores.json
|-- Metadata.xlsx

```

- Segmentation/train/val/test/: Contains hand radiographs in BMP format. Each image file follows a naming convention similar to JP\_[Center]\_P[PatientID]\_[StudyDate]\_[ImageID]\_[L/R].bmp, where L and R indicate the left or right hand, respectively. The StudyDate field is de-identified via a consistent temporal offset applied per patient.
- Segmentation/\_annotations\_bone\_rle.coco.json: COCO-format annotations for hand bone structure segmentation. Masks are stored using run-length encoding (RLE) in the segmentation field. The categories correspond to anatomical structures and related objects, such as Capitate, Lunate, Scaphoid, Radius, Ulna, MC1-MC5, PP1-PP5, DP1-DP5, as well as some non-bone objects such as Metal Implant, Ring, and SoftTissue. The format of entries in the JSON file is shown as follows:

```

{
  "images": [
    {
      "id": 0,
      "file_name": "JP_SCGH_P0024_20130727_1661_L.bmp",
      "height": 1431,
      "width": 893
    },
    ...
  ],
  "annotations": [
    {
      "id": 1,
      "image_id": 0,
      "category_id": 30,
      "bbox": [14.0, 198.0, 852.0, 1233.0],
      "area": 515212.0,
      "segmentation": {
        "size": [1431, 893],
        "counts": "... "
      }
    },
    ...
  ],
  "categories": [
    {
      "id": 1,
      "name": "Capitate",
      "supercategory": "bone"
    },
    {
      "id": 9,
      "name": "Lunate",
      "supercategory": "bone"
    },
    ...
  ]
}

```

- Segmentation/\_annotations\_be\_rle.coco.json: COCO-format annotations for bone erosion related segmentation. The masks are also stored in RLE format. The categories include Non-SvdH-BE, SvdH-BE-50, and SvdH-BE-90.

- SvdH\_Scoring/SvdH\_BE\_Scoring/train/val/test/: Each subset contains folders named by case identifiers, e.g., JP\_HMCRD\_P0001\_20210203\_6791\_L. Inside each folder are ROI images in BMP format for bone erosion scoring. A typical folder contains 16 ROI images corresponding to joints/surfaces such as CMC-T, IP, L, Tm, R, U, MCP-T, MCP-I, MCP-M, MCP-R, MCP-S, PIP-I, PIP-M, PIP-R, and PIP-S.
- SvdH\_Scoring/SvdH\_BE\_Scoring/\_annotations\_be\_joint\_detection.coco.json: A COCO-format JSON file containing joint detection annotations for BE-related ROIs. Each image entry represents a hand radiograph, and the annotations provide bounding boxes for the corresponding joints. The categories section maps category IDs to joint names such as R, U, L, CMC-T, S, Tm, PIP-S, and MCP-T.
- SvdH\_Scoring/SvdH\_BE\_Scoring/\_annotation\_be\_scores.json: A JSON file containing ground-truth BE scores, indexed by full image filename. The format of entries in the JSON file is shown as follows:

```
{
  "JP_HMCRD_P0167_20111230_3497_L.bmp": {
    "BE_MCP-T": 0,
    "BE_MCP-I": 1,
    "BE_MCP-M": 0,
    "BE_MCP-R": 0,
    "BE_MCP-S": 0,
    "BE_IP": 0,
    "BE_PIP-I": 0,
    "BE_PIP-M": 0,
    "BE_PIP-R": 1,
    "BE_PIP-S": 1,
    "BE_CMC-T": 0,
    "BE_Tm": 1,
    "BE_S": 0,
    "BE_L": 0,
    "BE_U": 0,
    "BE_R": 0
  }
}
```

- SvdH\_Scoring/SvdH\_JSN\_Scoring/train/val/test/: Each subset contains folders named by case identifiers. Inside each folder are ROI images in BMP format for joint space narrowing (JSN) scoring. A typical folder contains 15 ROI images corresponding to CMC-M, CMC-R, CMC-S, SC, SR, STT, MCP-T, MCP-I, MCP-M, MCP-R, MCP-S, PIP-I, PIP-M, PIP-R, and PIP-S.
- SvdH\_Scoring/SvdH\_JSN\_Scoring/\_annotations\_jsn\_joint\_detection.coco.json: A COCO-format JSON file containing joint detection annotations for JSN-related ROIs. The categories include carpal joints such as CMC-M, CMC-R, CMC-S, SC, SR, STT, as well as finger joints such as MCP-T, MCP-I, MCP-M, MCP-R, MCP-S, PIP-I, PIP-M, PIP-R, and PIP-S.
- SvdH\_Scoring/SvdH\_JSN\_Scoring/\_annotation\_jsn\_scores.json: A JSON file containing ground-truth JSN scores, indexed by full image filename. The format of entries in the JSON file is shown as follows:

```
{
  "JP_HMCRD_P0167_20111230_3497_L.bmp": {
    "JSN_MCP-T": 2,
    "JSN_MCP-I": 0,
    "JSN_MCP-M": 0,
    "JSN_MCP-R": 0,
    "JSN_MCP-S": 0,
    "JSN_PIP-I": 0,
    "JSN_PIP-M": 0,
    "JSN_PIP-R": 0,
    "JSN_PIP-S": 0,
    "JSN_STT": 0,
  }
}
```

```

    "JSN_SC": 0,
    "JSN_SR": 0,
    "JSN_CMC-M": 0,
    "JSN_CMC-R": 0,
    "JSN_CMC-S": 0
  }
}

```

- **Metadata.xlsx**: An Excel file containing study-level metadata. The main columns include:
  - **Mapped Image Stem**: A normalized image or study identifier.
  - **StudyID**: A patient-specific study index indicating the chronological order of examinations for the same individual. It is used to distinguish different follow-up time points within a patient.
  - **Normalized PatientID**: Normalized anonymized patient identifier.
  - **isRA**: Binary indicator of rheumatoid arthritis status.
  - **Sex**: Patient sex.
  - **Age**: Patient age.
  - **Center**: Source center or institution.
  - **PixelSpacing**: In-plane image resolution.
  - **ImageSize**: Image size in pixels.
  - **LR**: Hand side indicator.

## B Related Works

### B.1 Hand Bone Structure Segmentation

Table 6: Summary of representative works on hand/wrist bone structure segmentation. Ann/Img: Annotations per image.

Works	Year	Method	Dataset	Images (Ann/Img)	Patients	Objects			
						F	MC	C	UR
Thodberg et al. [64]	2002	AAM	Private	99 (-)	-	✓	✓		✓
Kauffman et al. [26]	2004	AAM	Private	50 (20)	-	✓	✓		
Yang et al. [75]	2021	ResNet	Private	720 (2)	360				✓
Kang et al. [25]	2022	CNN	Private	702 (10)	702			✓	✓
Lee et al. [32]	2023	SAM	Private	192 (7)	192		✓		✓
Du et al. [9]	2024	GRU-Unet	Private	2000 (13)	-	✓	✓		✓
Yang et al. [77]	2025	SwinUMamba	[76]	618 (14)	388		✓	✓	✓

**F**: Finger bones; **MC**: Metacarpals; **C**: Carpal bones; **UR**: Radius and ulna.  
**AAM**: Active Appearance Model.

As summarized in Table 6, early studies on hand/wrist radiographs mainly relied on model-driven approaches such as active appearance models (AAMs), which explicitly encode shape and appearance priors for bone localization and segmentation [64, 26]. However, these methods were typically evaluated on small private datasets and focused on limited anatomical structures.

Recent work has shifted toward deep learning-based segmentation. Methods based on ResNet, CNN, SAM, GRU-Unet, and SwinUMamba have been applied to segment different hand/wrist structures, including the radius/ulna, carpal bones, metacarpals, and phalanges [75, 25, 32, 9, 77]. Although these approaches improve segmentation performance, most were developed on private datasets, and many remain restricted to partial anatomical regions, especially the wrist.

Large-scale hand/wrist radiograph datasets such as RSNA Bone Age [16] and DHA [13] provide substantial data volume but only global labels, limiting their use for pixel-wise structural learning. Other datasets, such as GRAZPEDWRI-DX [45], provide detection-oriented annotations rather than segmentation. More recent RA-oriented datasets, such as RAM-W600 [76], introduce bone-level annotations but remain limited to the wrist region.

## B.2 Hand BE Segmentation

Bone erosion (BE) in radiographs remains challenging to characterize due to its typically small lesion size, low contrast, and the difficulty of obtaining precise annotations. Existing studies have predominantly focused on quantitative analyses of BE, whereas pixel-wise segmentation has received comparatively limited attention. Most prior work emphasizes clinically relevant tasks such as detection, grading, or severity assessment, rather than dense delineation of erosion regions. Consequently, BE is commonly analyzed at the image-, joint-, or region-level, rather than being explicitly formulated as a segmentation problem. To the best of our knowledge, there remains a paucity of research directly addressing BE segmentation in radiographs, which in turn hinders the development of anatomically consistent and interpretable models for pixel-level BE assessment.

## B.3 Qualitative Evaluation of BE and JSN

Table 7: Summary of representative works related to SvdH-based joint space narrowing (JSN) and bone erosion (BE) analysis. Ann/Img: Annotations per image.

Works	Year	Method	Dataset	Images (Ann/Img)	Patients	Scoring	Task	
							BE	JSN
Langs et al. [30]	2007	Appearance model	Private	17 (-)	8	Binary	✓	
Langs et al. [31]	2008	ASM	Private	57 (-)	28	Modified Sharp	✓	✓
Murakami et al. [44]	2018	DCNN	Private	159 (-)	159	Binary	✓	
Rohrbach et al. [52]	2019	VGG	Private	-	-	Ratingen	✓	
Hirano et al. [21]	2019	CNN	Private	216 (-)	108	SvdH	✓	✓
Maziarz et al. [40]	2021	CNN	[62]	674 (-)	562	SvdH	✓	✓
Hioki et al. [20]	2021	YOLO V3	Private	50 (20)	-	SvdH	✓	
Miyama et al. [43]	2022	VGG	Private	226 (31)	40	SvdH	✓	✓
Wang et al. [68]	2022	EfficientNet	Private	915 (30)	400	mTSS		✓
Stolpovsky et al. [61]	2023	ViT	Public	330 (42)	330	Modified Sharp	✓	✓
Bo et al. [3]	2024	ResNet + MobileNetV2	Private	3818 (-)	-	SvdH	✓	✓
Bird et al. [2]	2025	DenseNet	Private	2059 (-)	410	SvdH	✓	✓
Lien et al. [34]	2025	EfficientNetV2	Private	823 (30)	-	mTSS		✓

ASM: Active Shape Model; mTSS: Modified Total Sharp Score.

Qualitative evaluation of BE and JSN in RA is typically performed at predefined joint sites based on expert interpretation of radiographic abnormalities, and remains an important component of clinical image assessment. As summarized in Table 7, most existing studies formulate these tasks as joint-level grading, classification, or score prediction, with the goal of estimating the severity of structural damage from local joint appearances rather than learning spatially explicit lesion representations.

Early studies mainly relied on model-based methods for BE analysis or combined BE / JSN assessment on small private datasets [30, 31]. These approaches incorporated structural priors and handcrafted representations to capture radiographic changes, but their evaluation was limited by dataset scale and restricted clinical variability. More recent work has shifted toward deep learning-based frameworks. Representative studies use CNNs, VGG, EfficientNet, and ViT models to predict BE and/or JSN grades from cropped joints or regional image patches [44, 52, 21, 40, 43, 68, 61, 3, 2, 34]. These methods have improved automated radiographic evaluation and enabled more scalable qualitative assessment, but they generally focus on joint-level outputs and formulate the problem as grading or scoring rather than dense prediction.

## C Detailed Information of Dataset

### C.1 License and Attribution

The conventional radiographs and associated annotations (bone structure segmentation masks, BE segmentation masks, SvdH-defined joint ROIs for BE / JSN scoring, and SvdH BE / JSN scores) in the dataset are licensed under the Creative Commons Attribution 4.0 International License (CC BY 4.0).

For proper attribution when using this dataset in any publications or research outputs, please cite with the DOI.

Table 8: Radiographic imaging configuration parameters

	HMCRD	SCGH	SARC	HU1	HU2	HU3
Model	Radnext 32	KXO-50G	CS-7	-	-	-
Manufacturer	HITACHI	TOSHIBA	KONICA MINOLTA	FUJIFILM	FUJIFILM	FUJIFILM
Aluminum filter (mm)	0.5	NO	-	-	-	-
Tube voltage (kV)	50	45	-	-	-	-
Tube current (mA)	100	250	-	-	-	-
Exposure time (mSec)	25	14	-	-	-	-
Source to image (cm)	100	100	-	-	-	-
Resolution (mm/pixel)	0.15	0.15	0.175	0.15	0.15	0.15
Image size (pixel)	2010×1490	2010×1490	1430×1722	2010×1670	2010×1670	2010×1670
Bit depth (bit)	10	10	12	10	12	12

**HMCRD:** Hokkaido Medical Center for Rheumatic Diseases, Japan.

**SCGH:** Sapporo City General Hospital, Japan.

**SARC:** Sagawa Akira Rheumatology Clinic, Japan.

**HU1-3:** Faculty of Health Sciences, Hokkaido University, Japan.

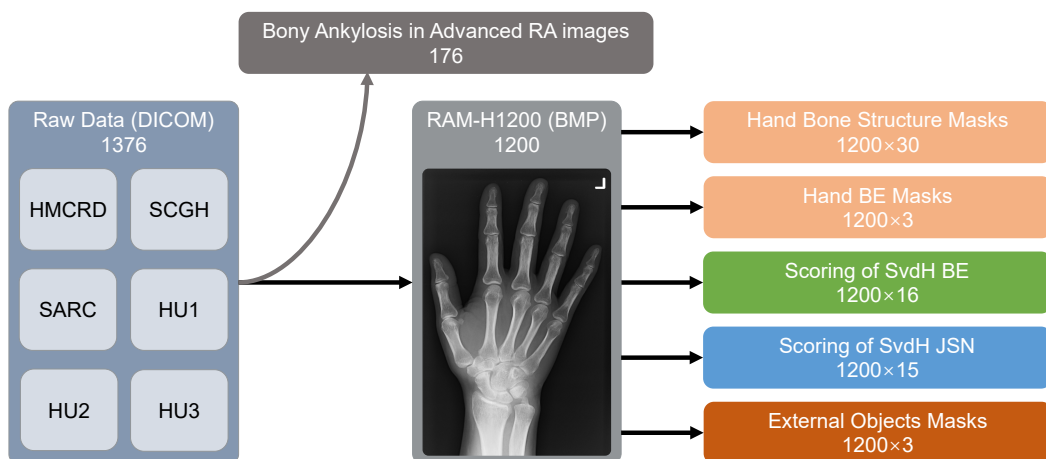


Figure 7: Overview of the data collection and processing pipeline for RAM-H1200. A total of 1376 DICOM-format hand radiographs were collected from six institutions. After excluding 176 advanced RA cases with bony ankylosis, 1200 images were retained and converted to BMP format. The dataset supports multiple tasks, including hand bone structure segmentation ( $1200 \times 30$  masks), bone erosion (BE) segmentation ( $1200 \times 3$  masks), SvdH BE scoring ( $1200 \times 16$  joints), SvdH JSN scoring ( $1200 \times 15$  joints), and external object segmentation ( $1200 \times 3$  masks, covering catheters, implants, and rings).

**Suggested Citation:** Yang, S., Wang, H., Fu, Y., Peng, J., Fan, L., Chen, H., Song, J., Ikebe, M., Takamaeda-Yamazaki, S., Okutomi, M., Kamishima, T., & Ou, Y.(2026). RAM-H1200: A Unified Evaluation and Dataset on Hand Radiographs for Rheumatoid Arthritis. <https://doi.org/10.57967/hf/8548>

## C.2 Data Rights Compliance and Issue Reporting

We are committed to complying data protection rights in accordance with relevant regulations, including but not limited to the General Data Protection Regulation (GDPR). All personally identifiable information (PII) has been removed through anonymization techniques. If any individual represented in the dataset wishes to have their data removed, we provide a clear and accessible process for issue reporting and resolution via our GitHub repository. Concerned parties are encouraged to contact the authors directly through the contact form linked on the GitHub page. Upon receiving a request, we will engage with the individual to verify their identity and promptly remove the relevant data entries from the dataset.

Table 9: Score distributions across centers in train, valid, and test sets.

(a) <i>Hand Bone Structure Segmentation</i>							(b) <i>Hand BE Segmentation</i>						
SvdH	HMCRD	SARC	SCGH	HU1	HU2	HU3	SvdH BE	HMCRD	SARC	SCGH	HU1	HU2	HU3
<i>Train Set</i>							<i>Train Set</i>						
0-4	153	68	19	0	4	1	0-4	204	165	82	2	5	2
5-9	106	86	40	2	1	1	5-9	104	84	19	0	3	0
10-19	51	108	39	0	3	0	10-14	35	36	5	0	0	0
20-29	33	28	7	0	0	0	15-19	17	8	1	0	0	0
30-39	21	6	2	0	0	0	20-24	6	3	0	0	0	0
40-59	13	1	0	0	0	0	25-29	7	1	0	0	0	0
60+	0	0	0	0	0	0	30+	4	0	0	0	0	0
<i>Valid Set</i>							<i>Valid Set</i>						
0-4	28	1	0	1	5	0	0-4	53	6	1	2	8	0
5-9	36	1	0	1	3	0	5-9	30	12	1	0	0	0
10-19	37	13	1	0	0	0	10-14	21	4	0	0	0	0
20-29	3	7	1	0	0	0	15-19	1	0	0	0	0	0
30-39	1	0	0	0	0	0	20-24	1	0	0	0	0	0
40-59	1	0	0	0	0	0	25-29	0	0	0	0	0	0
60+	0	0	0	0	0	0	30+	0	0	0	0	0	0
<i>Test Set</i>							<i>Test Set</i>						
0-4	54	0	0	0	1	0	0-4	110	0	3	0	2	0
5-9	72	17	1	0	1	0	5-9	64	21	1	0	5	0
10-19	58	22	2	0	6	0	10-14	17	21	0	0	1	0
20-29	11	5	1	0	0	0	15-19	8	2	1	0	0	0
30-39	7	0	0	0	0	0	20-24	3	1	0	0	0	0
40-59	1	4	1	0	0	0	25-29	1	3	0	0	0	0
60+	2	1	0	0	0	0	30+	2	1	0	0	0	0
<b>(c) Scoring of SvdH BE</b>							<b>(d) Scoring of SvdH JSN</b>						
SvdH BE	HMCRD	SARC	SCGH	HU1	HU2	HU3	SvdH JSN	HMCRD	SARC	SCGH	HU1	HU2	HU3
<i>Train Set</i>							<i>Train Set</i>						
0	4716	3681	1477	32	107	32	0	4758	3277	992	21	92	22
1	887	796	168	0	18	0	1	491	802	482	4	24	5
2	275	212	46	0	3	0	2	202	286	112	5	1	3
3	21	34	18	0	0	0	3	85	60	16	0	3	0
5	133	29	3	0	0	0	4	119	30	3	0	0	0
<i>Valid Set</i>							<i>Valid Set</i>						
0	1307	242	24	30	113	0	0	1280	215	11	23	100	0
1	288	78	7	2	15	0	1	248	52	5	6	20	0
2	69	29	1	0	0	0	2	44	43	14	1	0	0
3	7	3	0	0	0	0	3	13	20	0	0	0	0
5	25	0	0	0	0	0	4	5	0	0	0	0	0
<i>Test Set</i>							<i>Test Set</i>						
0	2540	426	63	0	89	0	0	2422	594	30	0	76	0
1	440	232	9	0	36	0	1	426	84	32	0	42	0
2	251	94	3	0	3	0	2	153	30	7	0	2	0
3	8	14	3	0	0	0	3	53	7	4	0	0	0
5	41	18	2	0	0	0	4	21	20	2	0	0	0

### C.3 Data Acquisition

Radiographs were collected from six institutions with varying imaging configurations, including differences in equipment models, acquisition settings, and image resolutions, as shown in Table 8.

### C.4 Data Pre-Processing

As illustrated in Fig. 7, a total of 1376 DICOM-format hand radiographs were initially collected from six institutions. Compared to [76], the collected cohort includes a larger proportion of moderate-to-advanced RA cases, which increases annotation complexity due to severe anatomical deformation and structural overlap. However, cases with advanced RA exhibiting bony ankylosis were excluded, as extensive bone fusion and joint deformation limit their clinical relevance for fine-grained structural analysis. In total, 176 such cases were filtered out, resulting in 1200 images retained for further processing.

Table 10: Detailed annotation reliability statistics for BE, JSN, and their combined scores. Reliability was quantified using the intraclass correlation coefficient under the one-way random-effects single-measure setting, ICC(1,1). MSB and MSW denote the mean square between subjects and the mean square within subjects, respectively.

Task	MSB	MSW	ICC(1,1)
SvdH BE Score	0.9700	0.2671	0.5682
SvdH JSN Score	1.4466	0.5485	0.4502
SvdH BE + JSN Score	1.2686	0.4032	0.5176

All selected radiographs were converted from DICOM format to BMP format to facilitate standardized data handling and compatibility with common deep learning pipelines. The resulting dataset forms the basis for multiple downstream tasks, including hand bone structure segmentation, BE segmentation, and SvdH-based scoring for both BE and JSN.

### C.5 Dataset Split

To avoid patient-level data leakage, the train, validation, and test sets were split at the patient level, ensuring that all radiographs from the same patient, including bilateral hands and longitudinal follow-up studies, were assigned to the same subset. Table 9 details the institution-wise distribution across the four related tasks. Table 9a summarizes the institution-wise distribution for the hand bone structure segmentation dataset, while Table 9b presents the corresponding distribution for the BE segmentation dataset. Table 9c and Table 9d further show the score distributions for the SvdH BE scoring and SvdH JSN scoring datasets, respectively. This breakdown highlights the contribution of each collaborating institution and illustrates how score imbalance manifests across different sources and subsets.

### C.6 Annotation Reliability Analysis

We report the detailed annotation reliability statistics in Table 10. The intraclass correlation coefficient (ICC) was calculated using the ICC(1,1) formulation, where MSB and MSW denote the mean square between subjects and the mean square within subjects, respectively. The ICC values were computed from the initial independent annotations before consensus discussion, and therefore reflect the baseline inter-annotator agreement of the scoring process.

The obtained ICC values indicate moderate initial agreement for BE and the combined BE/JSN annotations, while JSN shows relatively lower agreement. This trend is expected because JSN scoring depends on subtle differences in joint space width and alignment, which can be affected by projection variation, anatomical overlap, and adjacent-grade ambiguity. The observed initial agreement is broadly consistent with prior RA radiographic scoring studies, where SvdH-based intra- and interobserver ICC values were reported in a similar range [12]. After this initial assessment, discrepant cases were reviewed and resolved through consensus discussion to produce the final annotations used in RAM-H1200. These results suggest that the annotation process provides a reasonable and clinically meaningful reference, while also reflecting the inherent subjectivity of fine-grained radiographic scoring.

### C.7 Dataset Maintenance

As the authors and maintainers of this dataset, we affirm that while the dataset is self-contained and does not depend on any external links or content, we may provide future updates, such as adding new cases or incorporating additional tasks. These potential updates aim to enhance the dataset’s value while maintaining its long-term usability.

## D Detailed Information of Tasks

RAM-H1200 is designed as a unified multi-task benchmark for comprehensive analysis of RA from hand radiographs. As illustrated in Fig. 8 and Table 11, the dataset supports multiple levels of analysis. At the structure level, it provides instance-level annotations for all hand bone structures, enabling hand bone structure segmentation. At the lesion level, pixel-wise annotations of BE are provided to

Table 11: Summary of RAM-H1200 benchmark tasks.

Task	Input	Output	Primary metric	What it evaluates	Challenges
Hand bone structure segmentation	Whole-hand radiograph	30 bone structure masks	DSC / NSD / DSC <sub>O</sub> / NSD <sub>O</sub>	Anatomical structure modeling	Projection-induced overlap ambiguity
Hand BE segmentation	Whole-hand radiograph / local patch	Pixel-level BE mask	DSC / REC / PREC	Quantitative lesion localization	Tiny, sparse, and low-contrast lesions
Scoring of SvdH BE	SvdH-defined joint ROI	Ordinal score 0/1/2/3/5	QWK / MAE / BACC	Clinical erosion severity	Class imbalance and subjective adjacent grades
Scoring of SvdH JSN	SvdH-defined joint ROI	Ordinal score 0/1/2/3/4	QWK / MAE / BACC	Structural narrowing severity	Adjacent-grade ambiguity and joint-dependent variation

**BE**: bone erosion; **JSN**: joint space narrowing; **SvdH**: Sharp/van der Heijde; **DSC**: Dice similarity coefficient; **NSD**: normalized surface Dice; **REC**: recall; **PREC**: precision; **QWK**: quadratic weighted kappa; **MAE**: mean absolute error; **BACC**: balanced accuracy. Subscript *O* denotes overlap-aware evaluation.

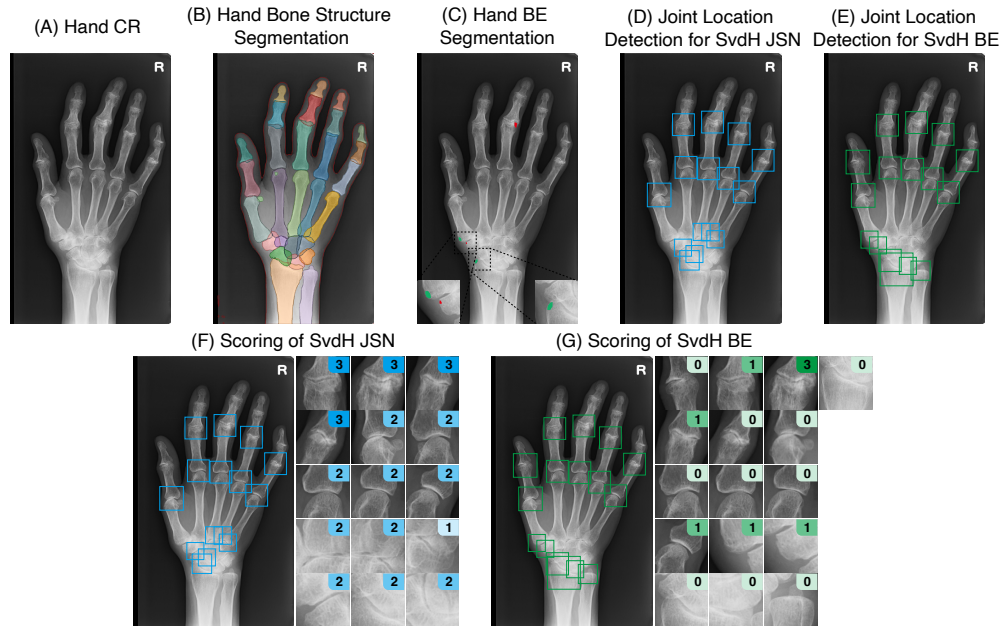


Figure 8: Overview of the tasks supported in RAM-H1200. (A) Original hand radiograph (CR). (B) Instance-level segmentation of hand bone structures across the entire hand. (C) Pixel-wise segmentation of BE regions. (D,E) Joint localization for SvdH scoring, where predefined joint regions are detected for JSN and BE assessment, respectively. (F,G) Joint-level SvdH scoring for JSN and BE, where each detected joint is assigned an ordinal severity score based on cropped regions. This figure illustrates the multi-level nature of the benchmark, spanning structure-level modeling, lesion-level analysis, and clinically grounded scoring.

facilitate fine-grained pathological analysis. At the clinical level, the dataset follows the standardized SvdH protocol, where predefined joint regions are first localized and then assigned ordinal severity scores for both BE and JSN. These tasks are defined in a unified framework, allowing the study of

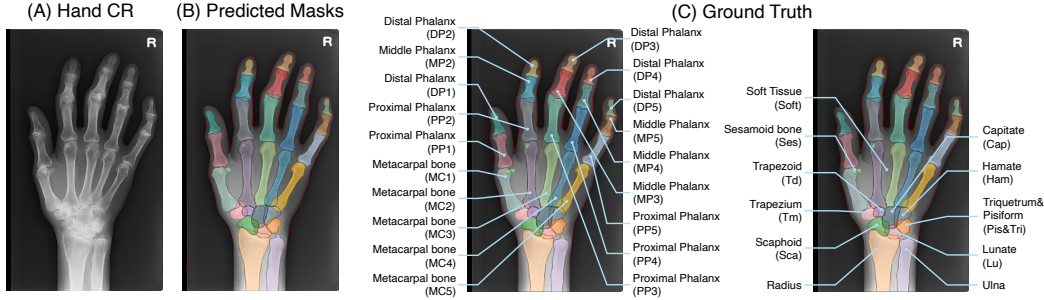


Figure 9: Hand bone structure segmentation task on radiographs. (A) Input hand CR image. (B) Model predictions. (C) Ground truth annotations with fine-grained instance-level labels. The task requires comprehensive segmentation of all hand bones, including phalanges, metacarpals, and carpal structures, as well as surrounding tissues, under strong projection-induced overlap and complex anatomical configurations.

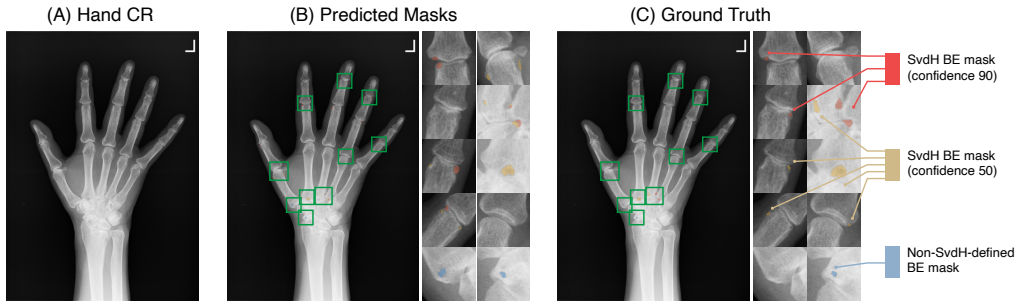


Figure 10: Illustration of the hand BE segmentation task on hand radiographs. (A) Input hand CR image. (B) Representative predicted BE masks with corresponding regions of interest (green boxes), highlighting localized erosion patterns. (C) Ground truth annotations, including SvdH-defined BE regions with different confidence levels (e.g., 90 and 50) and additional non-SvdH-defined erosion regions. The task focuses on detecting and delineating small and subtle erosive lesions under severe class imbalance and ambiguous appearance, particularly in early-stage RA.

relationships between anatomical structures, localized lesions, and clinically interpretable scoring outcomes.

## D.1 Hand Bone Structure Segmentation

Hand bone structure segmentation aims to delineate all bone instances across the entire hand from radiographs, as illustrated in Fig. 9. This task serves as the structural foundation for subsequent analysis, including joint localization, morphological assessment, and clinically grounded scoring.

Compared to wrist-focused settings, hand bone structure segmentation introduces increased complexity due to the larger number of anatomical structures, diverse bone shapes, and extensive projection overlap, particularly in the carpal region. The task requires distinguishing fine-grained boundaries between adjacent bones while maintaining global anatomical consistency across the hand.

Accurate segmentation enables explicit modeling of bone geometry and spatial relationships, which are essential for both structure-oriented tasks such as JSN assessment and lesion-oriented tasks such as BE analysis. The provided annotations support instance-level segmentation of all hand bones, allowing models to jointly capture local details and global structural organization.

## D.2 Hand BE Segmentation

Hand BE segmentation focuses on pixel-level delineation of erosive lesions in hand radiographs (Fig. 10). This task enables direct and quantitative assessment of structural damage, providing spatially explicit information beyond traditional grading-based approaches.

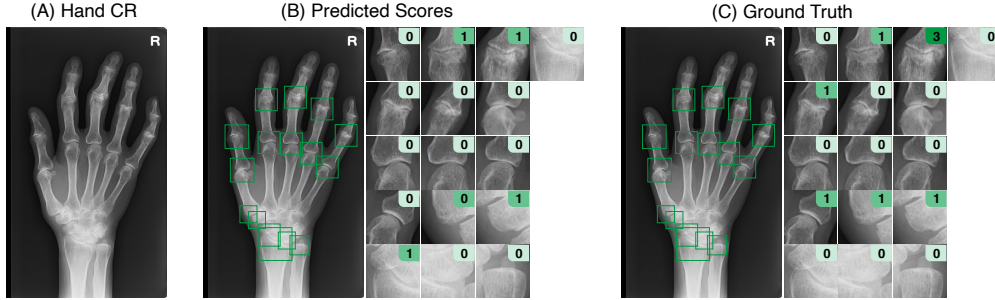


Figure 11: SvdH-based BE scoring task on hand radiographs. (A) Input CR image. (B) Predicted ordinal scores at predefined joint regions, shown with corresponding joint crops. (C) Ground truth scores. Each joint is assigned a discrete SvdH score reflecting the severity of erosion. The task is formulated as an ordinal classification problem, focusing on joint-level assessment rather than explicit delineation of lesion boundaries.

Hand BE segmentation is particularly challenging due to the extremely small size of lesions, severe class imbalance, and low contrast between erosion regions and surrounding bone structures. In early-stage RA, erosive changes often manifest as subtle cortical irregularities, making them difficult to distinguish from normal anatomical variations and imaging artifacts.

Furthermore, erosion patterns are closely associated with anatomical structures, typically occurring along bone surfaces and near joint interfaces. As a result, accurate BE segmentation inherently relies on structural context, and benefits from joint modeling of anatomy and pathology.

The dataset provides pixel-level BE annotations categorized according to SvdH principles, enabling fine-grained and anatomically consistent evaluation of erosion detection and delineation.

### D.3 Scoring of SvdH BE

SvdH BE scoring is a key component of the SvdH scoring system, widely adopted in CAD systems for evaluating the severity of joint damage in RA. As illustrated in Fig. 11, this task focuses on assessing the degree of bone erosion at predefined joint locations from radiographs, rather than delineating the exact lesion boundaries. Each joint is assigned a discrete severity level based on the extent of structural damage, reflecting progressive stages of erosion.

In our setting, BE is evaluated at **16 predefined joint locations per hand**, following the SvdH standard. These include *four proximal interphalangeal (PIP) joints (digits 2–5), four metacarpophalangeal (MCP) joints (digits 2–5), the interphalangeal (IP) joint of the thumb, and seven wrist-related joint regions (including radiocarpal and intercarpal articulations)*. Each joint surface is annotated with one of five ordinal classes corresponding to the raw SvdH BE scores of (0, 1, 2, 3, 5). Accordingly, the task is formulated as a joint-level severity prediction problem.

Unlike segmentation-based approaches that aim to localize erosion regions, SvdH BE scoring requires the model to infer the overall severity of damage from the radiographic appearance of a given joint ROI. Since the score labels are inherently ordered, this task is more appropriately modeled as an ordinal classification problem rather than a standard multi-class classification task.

In our implementation, we adopt an ordinal classification strategy, where the model predicts a series of ordered binary thresholds. Specifically, for a 5-class problem, the model outputs 4 binary decisions, each indicating whether the true score exceeds a given threshold. The final score is obtained by counting the number of positive predictions, allowing the model to preserve the ordinal relationships among severity levels while maintaining a simple and effective formulation.

The task is particularly challenging due to the subtle visual differences between adjacent severity levels. Early-stage erosion often manifests as mild cortical irregularities that are difficult to distinguish from normal anatomical variation. In addition, factors such as image quality, projection differences, and complex anatomical overlap in the wrist further hinder consistent assessment. As a result, SvdH BE scoring constitutes a clinically meaningful yet challenging fine-grained ordinal prediction task.

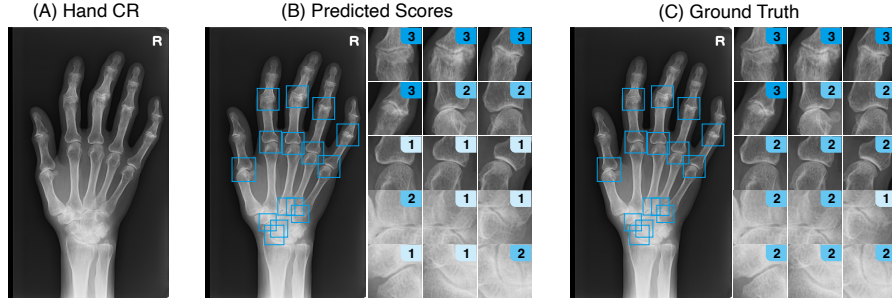


Figure 12: Illustration of the SvdH JSN scoring task. (A) Input hand radiograph. (B) Predicted JSN scores at predefined joint locations, with corresponding cropped regions of interest. (C) Ground truth annotations. Each joint is assigned an ordinal score according to the SvdH system, reflecting the degree of joint space narrowing. Unlike lesion-based analysis, this task focuses on structural assessment of inter-bone spacing at the joint level.

#### D.4 Scoring of SvdH JSN

SvdH JSN scoring is a key component of the SvdH scoring system, widely adopted in CAD systems for evaluating the progression of joint space narrowing in RA. As illustrated in Fig. 12, this task focuses on assessing the degree of joint space narrowing progression at predefined joint locations from radiographs, reflecting structural changes associated with disease development over time.

In our setting, JSN is evaluated at **15 predefined joint locations per hand**, following the SvdH standard. These include: *four proximal interphalangeal (PIP) joints (digits 2–5), four metacarpophalangeal (MCP) joints (digits 2–5), the interphalangeal (IP) joint of the thumb, and six wrist joint regions (including the radiocarpal and intercarpal articulations)*. Each joint is assigned one of five ordinal classes corresponding to the raw SvdH JSN scores of (0, 1, 2, 3, 4). Accordingly, the task is formulated as a joint-level severity prediction problem rather than lesion localization.

Compared with BE scoring, SvdH JSN scoring is more structure-oriented, as it primarily depends on the relative spacing and configuration between adjacent bones instead of localized erosive patterns. The model must therefore capture differences in joint space width and joint geometry from radiographic appearance.

Since the score labels are inherently ordered, this task is also formulated as a 5-level ordinal classification problem. We adopt the same ordinal classification formulation as in SvdH BE scoring, where the model predicts a series of ordered binary thresholds and derives the final score accordingly.

The task is particularly challenging due to the subtle visual differences between adjacent severity levels. JSN often manifests as gradual narrowing of joint space, which can be difficult to quantify under projection effects, anatomical overlap, and variations in imaging quality. As a result, reliable scoring requires the model to capture fine-grained structural relationships between adjacent bones in a consistent and clinically meaningful manner, making SvdH JSN scoring a challenging ordinal prediction task.

## E Implementation Details

### E.1 Hand Bone Structure Segmentation

All radiographs were processed in a patch-wise manner using random cropping with a patch size of  $512 \times 512$ , where 70% of the sampled patches were constrained to contain foreground regions. For each radiograph, 16 patches were randomly sampled per epoch. Model training employed the AdamW optimizer with a weight decay of  $1 \times 10^{-2}$ . The initial learning rate was set to  $1 \times 10^{-4}$  and decayed using a cosine annealing schedule (CosineAnnealingLR). Training was conducted for up to 200 epochs with a batch size of 8 and standard data augmentation techniques. All experiments were conducted with a fixed random seed for reproducibility. Early stopping was applied based on the validation Dice score with a patience of 15 epochs.

## E.2 Hand BE Segmentation

All radiographs were processed in a patch-wise manner using random cropping with a patch size of  $256 \times 256$ , where 70% of the sampled patches were constrained to contain foreground regions. For each radiograph, 24 patches were randomly sampled per epoch. Although three-class BE annotations are available, we restrict the benchmark to the SvdH-defined BE category (i.e., SvdH-BE-90) in this setting. Benchmark results using all classes are provided in Appendix F.2.2. For each radiograph, 24 patches were randomly sampled per epoch. Model training employed the AdamW optimizer with a weight decay of  $1 \times 10^{-2}$ . The initial learning rate was set to  $1 \times 10^{-4}$  and decayed using a cosine annealing schedule (CosineAnnealingLR). Training was conducted for up to 200 epochs with a batch size of 16 and standard data augmentation techniques. All experiments were conducted with a fixed random seed for reproducibility. Early stopping was applied based on the validation Dice score with a patience of 20 epochs. For nnUnet, we adopted its default experimental planning and training pipeline, where preprocessing, network architecture, and hyperparameters are automatically configured based on the dataset. The model was trained for 500 epochs following the standard nnUnet setting, and all other configurations, including data sampling strategies, were kept unchanged.

## E.3 Scoring of SvdH BE

All joint crops were processed in an image-wise manner and resized to  $224 \times 224$ . Model training employed an ordinal classification formulation with 4 binary thresholds optimized by BCEWithLogit-sLoss. The AdamW optimizer was used with a weight decay of  $1 \times 10^{-3}$ . The initial learning rate was set to  $1 \times 10^{-4}$  and decayed using a cosine annealing schedule (CosineAnnealingLR). Training was conducted for 200 epochs with a batch size of 32. All experiments were conducted with a fixed random seed for reproducibility.

## E.4 Scoring of SvdH JSN

All joint crops were processed in an image-wise manner and resized to  $224 \times 224$ . Model training employed an ordinal classification formulation with 4 binary thresholds optimized by BCEWithLogit-sLoss. The AdamW optimizer was used with a weight decay of  $1 \times 10^{-3}$ . The initial learning rate was set to  $1 \times 10^{-4}$  and decayed using a cosine annealing schedule (CosineAnnealingLR). Training was conducted for 200 epochs with a batch size of 32. All experiments were conducted with a fixed random seed for reproducibility.

# F Detailed Analysis of Experimental Results

## F.1 Hand Bone Structure Segmentation

### F.1.1 Overall and Bone-wise Results

Quantitative results for hand bone structure segmentation are summarized in Table 12 and Table 13, with qualitative comparisons shown in Fig. 13 and Fig. 14. Overall, supervised models achieve strong segmentation performance across most anatomical structures. In Table 12, SwinUNETR obtains the highest Bone Mean DSC of 97.25%, followed closely by UMambaEnc with 97.24% and SwinUMamba with 97.23%. The corresponding All Mean DSC values are also highly similar, with SwinUNETR and UMambaEnc both reaching 97.32%, and SwinUMamba reaching 97.31%. These small differences indicate that the general whole-bone segmentation task is already relatively well handled by supervised models.

The bone-wise results show that large and clearly visible bones are segmented with particularly high accuracy. The radius and ulna reach approximately 98–99% DSC for the best supervised models, and most metacarpal, proximal phalangeal, middle phalangeal, and distal phalangeal bones also achieve DSC values around or above 98%. In contrast, smaller or anatomically crowded structures remain more difficult. The sesamoid bones show the lowest DSC among all categories, with the best result only reaching 81.62% for SwinUNETR. Several carpal bones, including the trapezoid, lunate, trapezium, scaphoid, and pisiform/triquetrum, also show lower performance than long bones, reflecting the effect of small structure size, low contrast, and dense anatomical overlap around the wrist.

Table 12: DSC for hand bone structure segmentation on all anatomical structures. Bone Mean denotes the average over all bone categories except soft tissue, while All Mean denotes the average over all categories. The best result in each column is highlighted in **bold**, and the second-best result is underlined.

Model	Cap	Radius	Ulna	Ham	Lu	Pis&Tri	Sca	Tm
<b>Supervised Models</b>								
UNet	96.26±7.44	98.73±0.76	98.73±1.21	96.44±2.27	95.27±7.23	96.67±2.96	96.70±3.00	96.06±5.07
UNet++	97.13±2.65	98.83±0.71	98.82±1.22	96.81±1.66	95.86±4.60	96.99±2.41	97.13±3.19	96.44±2.60
SegFormer	96.28±3.63	98.64±0.63	98.55±1.18	96.07±1.91	95.29±3.86	96.06±2.32	96.10±3.18	95.52±4.17
TransUNet	97.19±2.23	<b>98.92±0.60</b>	98.84±1.14	96.97±1.47	<u>96.33±4.22</u>	97.09±2.30	97.24±2.41	96.48±2.99
SwinUNETR	97.10±3.12	<b>98.92±0.61</b>	<b>98.87±1.11</b>	97.02±1.61	96.18±4.14	97.19±1.82	97.30±2.36	<b>96.62±3.01</b>
UMambaEnc	<b>97.34±2.18</b>	98.88±0.63	98.85±1.24	96.99±1.61	96.25±4.02	97.20±2.08	97.22±3.60	96.56±3.42
SwinUMamba	97.10±3.02	<b>98.92±0.59</b>	<u>98.85±1.16</u>	<b>97.14±1.62</b>	<b>96.42±4.23</b>	<b>97.23±1.84</b>	<b>97.38±2.12</b>	<b>96.74±2.16</b>
MambaVision	95.56±3.82	98.16±0.73	98.21±1.16	95.32±1.92	94.52±3.96	95.51±2.81	95.11±3.36	94.98±3.22
<b>Foundation Models</b>								
SAM(Box)	91.50±4.91	92.22±15.45	97.66±6.41	85.50±7.23	85.91±5.53	94.33±3.63	89.79±4.50	81.54±4.86
SAM(Point)	75.54±29.15	90.80±13.66	96.15±12.13	69.69±27.91	74.37±27.16	89.03±20.23	73.14±28.31	62.06±25.67
MedSAM(Box)	82.08±7.97	83.49±7.87	87.14±11.83	77.22±7.92	76.25±7.65	84.38±6.76	78.11±8.10	81.24±6.86
<b>Supervised Models</b>								
UNet	94.14±8.22	98.34±2.11	97.95±3.78	97.65±4.52	97.93±2.80	98.39±1.10	97.94±4.93	97.61±4.43
UNet++	94.88±3.51	98.68±0.74	98.45±1.48	98.22±1.40	98.35±1.06	98.56±0.70	98.28±2.30	98.58±1.18
SegFormer	94.12±6.29	98.35±0.52	98.01±1.69	97.88±1.36	97.93±1.62	98.17±0.87	97.82±4.13	98.27±1.54
TransUNet	94.92±2.86	98.69±0.62	98.53±1.01	98.24±1.43	98.31±1.24	98.55±0.72	98.44±0.97	98.70±0.70
SwinUNETR	94.96±3.43	98.67±1.18	98.56±1.08	98.26±1.29	<b>98.44±0.81</b>	98.57±0.72	98.44±1.30	<b>98.71±0.86</b>
UMambaEnc	<b>95.12±2.64</b>	98.75±0.56	<b>98.58±1.03</b>	98.23±1.97	98.40±1.01	98.57±0.76	98.33±2.32	98.65±1.61
SwinUMamba	94.96±4.85	<b>98.79±0.56</b>	<b>98.58±1.06</b>	<b>98.33±1.37</b>	98.41±1.19	<b>98.62±0.84</b>	<b>98.53±0.76</b>	98.68±1.21
MambaVision	93.46±3.02	98.15±0.57	97.94±1.17	97.61±1.22	97.74±0.85	97.95±0.69	97.65±2.90	98.24±1.30
<b>Foundation Models</b>								
SAM(Box)	84.77±6.09	97.66±0.87	95.98±8.10	94.77±7.80	93.85±3.87	96.64±3.09	97.27±1.42	97.51±1.25
SAM(Point)	49.54±22.38	76.81±13.64	85.68±16.44	90.38±12.84	91.32±11.65	90.15±17.01	72.04±14.17	74.12±10.69
MedSAM(Box)	74.93±12.71	89.16±8.93	87.82±8.22	89.52±7.03	84.85±9.22	80.96±9.60	83.31±8.35	89.69±7.06
<b>Supervised Models</b>								
UNet	97.23±6.24	97.38±4.31	97.94±2.00	96.67±5.40	95.59±9.54	96.19±6.68	96.39±7.60	97.34±2.54
UNet++	98.63±1.52	98.35±2.61	98.34±0.85	98.34±1.08	98.37±1.22	98.22±2.17	97.64±4.19	97.67±1.08
SegFormer	98.34±2.02	98.16±2.09	97.95±1.07	97.97±0.81	97.98±1.53	97.95±0.96	96.85±7.18	97.16±1.03
TransUNet	98.59±1.45	98.40±2.21	98.28±0.97	98.10±1.04	98.21±2.07	98.22±1.50	97.61±4.09	97.65±1.07
SwinUNETR	98.67±1.30	98.42±1.95	98.45±0.81	98.40±0.90	98.26±1.89	98.23±1.70	<b>97.72±4.04</b>	97.68±1.40
UMambaEnc	98.60±1.67	98.47±1.93	98.35±1.20	<b>98.42±1.03</b>	98.38±1.95	98.38±1.04	97.55±4.34	97.57±1.24
SwinUMamba	<b>98.70±1.26</b>	<b>98.62±1.12</b>	<b>98.46±1.08</b>	<b>98.42±0.86</b>	<b>98.47±1.51</b>	<b>98.39±0.98</b>	97.71±5.19	<b>97.79±1.24</b>
MambaVision	98.26±1.43	98.17±1.42	97.86±1.20	97.79±0.70	97.85±1.53	97.80±1.41	96.60±6.28	96.47±3.08
<b>Foundation Models</b>								
SAM(Box)	97.63±1.61	97.59±1.18	97.26±1.08	96.29±1.64	96.50±1.60	96.32±2.10	94.84±2.62	95.96±1.69
SAM(Point)	72.25±9.03	71.94±7.55	73.46±7.42	70.98±21.11	68.20±19.83	74.48±18.72	83.29±19.09	58.98±15.39
MedSAM(Box)	88.91±8.07	86.74±8.87	80.02±7.15	82.93±9.01	84.97±8.11	83.23±8.05	75.95±8.81	79.31±7.92
<b>Supervised Models</b>								
UNet	95.85±6.05	95.50±5.70	96.23±6.42	96.17±4.47	78.26±13.19	99.50±0.19	96.26±2.77	96.37±2.68
UNet++	97.23±4.86	97.33±2.23	97.45±1.43	<b>96.75±4.28</b>	80.47±12.92	99.37±0.84	97.13±1.40	97.21±1.36
SegFormer	96.73±1.29	97.01±1.07	96.98±1.45	95.94±3.56	78.32±12.63	99.25±0.39	96.56±1.53	96.65±1.48
TransUNet	97.40±1.38	97.40±2.19	97.37±3.30	96.71±3.63	79.82±12.91	99.51±0.20	97.14±1.19	97.22±1.15
SwinUNETR	97.52±1.42	97.52±1.46	97.44±1.55	96.43±5.04	<b>81.62±13.29</b>	<b>99.52±0.23</b>	<b>97.25±1.22</b>	<b>97.32±1.18</b>
UMambaEnc	97.49±1.91	97.68±1.35	97.51±1.30	96.45±6.06	81.27±13.64	99.49±0.34	97.24±1.36	<b>97.32±1.32</b>
SwinUMamba	<b>97.61±1.73</b>	<b>97.73±1.25</b>	<b>97.54±1.22</b>	<b>96.78±5.37</b>	78.82±13.78	<b>99.52±0.28</b>	97.23±1.27	97.31±1.23
MambaVision	96.66±1.50	96.85±1.53	96.66±1.57	95.43±3.90	80.46±13.75	99.38±0.20	96.31±1.40	96.41±1.35
<b>Foundation Models</b>								
SAM(Box)	95.98±2.44	96.25±1.92	96.26±1.73	95.33±2.17	71.73±31.65	17.81±37.99	93.27±2.28	90.76±2.51
SAM(Point)	75.66±21.10	77.54±20.23	79.55±20.46	84.29±20.90	65.01±36.68	47.05±44.90	76.43±9.35	75.45±9.21
MedSAM(Box)	75.21±11.00	78.58±9.05	77.96±9.14	70.51±10.12	58.00±28.70	65.70±6.48	81.12±4.58	80.61±4.42

Table 13: NSD for bone segmentation on all hand bone structures. Bone Mean denotes the average over all bone categories except soft tissue, while All Mean denotes the average over all categories. The best result in each column is highlighted in **bold**, and the second-best result is underlined.

Model	Cap	Radius	Ulna	Ham	Lu	Pis&Tri	Sca	Tm
<b>Supervised Models</b>								
UNet	81.38±14.19	90.71±6.63	97.76±4.47	81.61±13.33	78.77±15.69	86.98±12.57	85.00±14.02	80.69±12.47
UNet++	84.55±13.38	91.89±6.24	97.98±4.54	83.93±11.48	80.59±15.40	88.48±11.75	87.88±12.96	82.06±12.25
SegFormer	77.55±14.00	89.75±6.36	97.14±4.70	77.29±12.34	75.89±16.68	81.11±13.82	79.59±14.16	74.84±11.95
TransUNet	84.75±12.57	<b>93.10±5.50</b>	98.39±3.86	84.99±11.18	83.46±14.87	89.50±11.06	88.55±12.91	82.59±11.97
SwinUNETR	84.60±13.52	92.89±5.80	98.38±3.87	85.55±11.64	81.82±15.19	89.00±11.46	88.66±12.50	<u>83.74±12.18</u>
UMambaEnc	<b>85.83±12.88</b>	92.67±5.86	98.39±4.14	85.10±11.88	82.73±15.71	89.44±11.75	88.91±11.83	83.35±11.94
SwinUMamba	84.46±12.91	<u>92.94±5.58</u>	<b>98.49±3.81</b>	<b>86.72±11.58</b>	<b>83.49±15.02</b>	<b>89.68±10.93</b>	<b>89.30±13.00</b>	<b>84.10±11.85</b>
MambaVision	69.01±14.41	83.87±7.17	94.30±5.85	69.39±12.86	70.48±18.40	78.00±13.55	71.50±16.87	69.95±11.81
<b>Foundation Models</b>								
SAM(Box)	60.98±15.95	75.02±11.28	95.95±9.85	47.07±15.69	60.51±13.81	75.70±14.67	66.29±14.32	47.16±10.43
SAM(Point)	47.26±28.07	69.53±17.68	93.59±15.42	35.58±22.76	53.46±23.64	71.51±22.38	51.34±27.66	32.88±19.14
MedSAM(Box)	24.74±12.82	29.13±13.37	44.97±20.50	22.28±11.13	24.38±11.36	32.74±14.74	26.20±12.34	29.69±11.66

Model	Td	MC1	MC2	MC3	MC4	MC5	PP1	PP2
<b>Supervised Models</b>								
UNet	74.96±16.05	95.33±6.97	94.54±8.74	91.81±8.88	95.26±7.17	96.84±4.57	95.40±7.75	95.38±10.68
UNet++	76.87±15.48	96.38±4.78	95.74±5.18	93.29±5.53	96.25±4.95	97.52±3.29	96.05±6.24	97.43±5.86
SegFormer	72.03±16.24	94.57±4.20	93.84±5.11	91.31±6.35	94.00±6.64	94.94±4.85	94.88±6.99	97.08±5.93
TransUNet	76.23±15.25	96.64±4.11	96.19±4.35	93.82±5.45	96.37±5.14	97.71±3.53	96.90±4.68	98.09±3.86
SwinUNETR	76.98±15.44	96.74±4.57	96.19±4.83	93.70±5.46	96.71±4.37	97.69±3.28	96.98±4.70	98.09±4.30
UMambaEnc	<u>77.64±15.51</u>	<u>97.13±3.82</u>	96.26±4.77	93.68±5.80	96.72±4.63	97.57±3.44	<u>96.68±6.03</u>	<b>98.26±4.51</b>
SwinUMamba	<b>78.00±15.32</b>	<b>97.34±3.45</b>	<b>96.41±4.76</b>	<b>94.28±5.38</b>	<b>96.95±4.34</b>	<b>98.08±3.24</b>	<b>97.22±4.28</b>	98.22±4.64
MambaVision	64.94±15.64	91.76±5.13	91.75±5.29	89.26±6.41	91.91±6.30	92.77±5.16	91.58±6.67	96.12±5.77
<b>Foundation Models</b>								
SAM(Box)	41.82±17.90	90.26±5.22	86.01±7.75	79.02±5.95	79.05±7.91	86.80±8.63	89.70±6.87	91.12±5.83
SAM(Point)	19.96±14.74	59.40±15.70	69.88±18.72	71.82±15.08	76.01±13.92	77.15±20.69	57.32±14.45	60.74±10.48
MedSAM(Box)	24.99±13.70	41.61±16.76	42.74±16.23	50.46±17.44	39.53±17.58	29.32±14.70	31.42±16.93	49.56±21.37

Model	PP3	PP4	PP5	MP2	MP3	MP4	MP5	DP1
<b>Supervised Models</b>								
UNet	94.78±12.30	94.75±9.85	96.40±6.21	94.43±9.31	91.39±13.89	92.44±12.53	94.15±10.63	94.40±6.87
UNet++	98.18±4.91	97.99±4.74	98.09±3.17	97.97±4.03	97.27±5.47	97.92±5.01	96.91±7.67	95.35±5.45
SegFormer	97.00±6.43	97.34±4.94	96.27±4.33	97.48±3.89	96.22±5.89	96.70±4.72	<u>94.87±9.66</u>	94.26±5.74
TransUNet	98.03±4.70	98.03±3.96	97.63±3.13	96.47±5.02	96.74±5.43	97.43±5.02	96.55±7.39	95.25±5.43
SwinUNETR	98.14±4.73	98.04±4.28	<u>98.29±3.33</u>	98.26±3.31	97.17±5.41	97.64±4.99	96.91±6.65	95.64±5.68
UMambaEnc	<u>98.26±4.81</u>	<u>98.39±3.92</u>	98.13±3.22	<b>98.60±3.74</b>	<u>97.82±5.28</u>	<u>97.95±5.17</u>	96.61±7.47	95.11±5.56
SwinUMamba	<b>98.38±4.53</b>	<b>98.48±3.84</b>	<b>98.58±3.38</b>	98.42±3.18	<b>97.96±4.30</b>	<b>98.37±3.75</b>	<b>97.25±7.84</b>	<b>95.88±5.18</b>
MambaVision	96.47±5.67	96.76±5.27	95.52±4.90	95.44±4.97	94.87±6.37	95.64±5.97	91.79±9.51	90.88±8.15
<b>Foundation Models</b>								
SAM(Box)	91.61±7.10	92.41±6.16	91.79±7.08	87.18±7.18	85.91±6.73	86.59±7.30	83.99±8.42	89.98±5.84
SAM(Point)	59.93±9.17	60.20±8.60	61.81±7.81	53.00±20.49	48.63±18.56	56.96±19.69	69.91±21.77	50.14±13.53
MedSAM(Box)	48.09±22.10	42.77±22.58	27.67±12.66	38.34±17.33	39.05±18.09	34.06±16.35	25.99±11.22	28.89±11.45

Model	DP2	DP3	DP4	DP5	Ses	Soft	Bone Mean	All Mean
<b>Supervised Models</b>								
UNet	93.30±11.04	91.92±12.15	93.45±10.60	95.27±8.49	70.37±16.41	92.89±6.95	90.33±6.00	90.41±5.82
UNet++	96.45±7.72	95.81±6.73	96.16±5.95	<u>96.53±7.66</u>	73.10±15.55	91.44±9.45	92.57±4.16	92.54±4.05
SegFormer	95.77±6.13	95.26±6.33	95.35±6.64	94.53±8.95	68.43±16.37	90.16±6.60	89.84±4.51	89.85±4.40
TransUNet	96.55±6.15	96.62±5.65	96.23±6.06	96.52±7.22	73.38±15.61	93.28±7.50	92.85±3.97	92.87±3.88
SwinUNETR	96.97±5.91	96.35±6.20	96.38±5.39	96.13±8.13	74.75±16.67	93.72±7.01	93.05±4.07	93.07±3.96
UMambaEnc	97.05±5.53	96.83±5.44	96.41±5.63	95.86±8.52	<b>75.91±15.99</b>	92.96±7.69	93.22±4.19	93.21±4.08
SwinUMamba	<b>97.16±5.69</b>	<b>96.98±5.24</b>	<b>96.48±5.59</b>	<b>96.89±7.44</b>	72.70±16.16	<b>94.06±7.08</b>	<b>93.42±3.96</b>	<b>93.44±3.86</b>
MambaVision	94.62±7.59	94.41±7.30	93.66±7.35	92.58±8.77	74.48±17.63	89.43±7.54	87.02±4.58	87.10±4.48
<b>Foundation Models</b>								
SAM(Box)	92.75±8.24	91.76±7.70	92.04±7.73	92.29±7.43	68.89±32.58	20.55±30.86	79.99±4.87	78.01±4.72
SAM(Point)	60.96±21.75	61.51±22.31	67.32±22.91	80.32±22.82	62.55±36.80	34.74±42.51	60.02±8.92	59.18±8.81
MedSAM(Box)	35.23±14.68	32.85±13.87	34.83±13.47	27.63±11.21	37.42±23.10	9.13±5.13	34.36±8.69	33.52±8.37



Figure 13: Hand bone structure segmentation results (A).

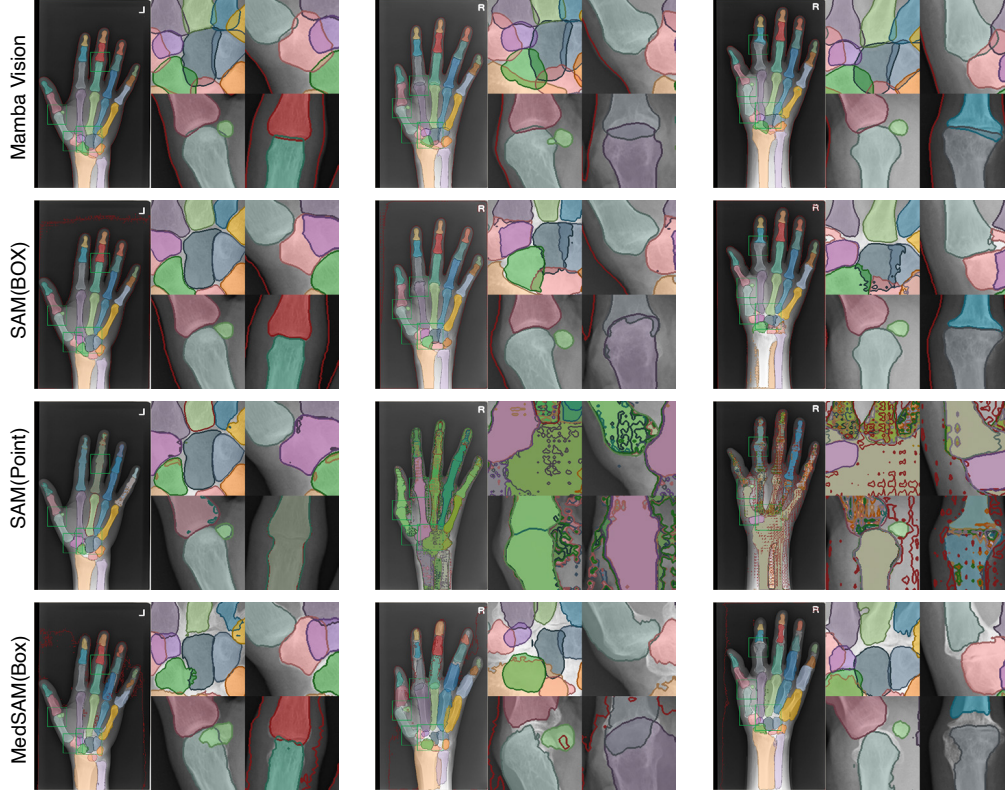


Figure 14: Hand bone structure segmentation results (B).

The NSD results in Table 13 make the boundary-level differences more apparent. SwinUMamba achieves the best Bone Mean NSD of 93.42% and All Mean NSD of 93.44%, while UMambaEnc ranks second with 93.22% Bone Mean NSD and 93.21% All Mean NSD. This suggests that although SwinUNETR slightly leads in Bone Mean DSC, SwinUMamba provides more accurate boundary alignment overall. The advantage is especially meaningful for small bones and joint-adjacent structures, where minor contour shifts can substantially affect anatomical consistency.

Qualitative results in Fig. 13 and Fig. 14 support these quantitative findings. Supervised models generally preserve the global hand skeleton and produce coherent masks for large bones and phalanges. However, visible differences appear around the wrist and metacarpal bases, where boundaries between adjacent bones are weak or partially overlapped. Models with stronger NSD performance produce smoother and more anatomically consistent contours, whereas weaker models show more fragmented masks, boundary leakage, or missing small structures. Foundation models are less reliable in these qualitative examples, especially in Fig. 14, where predictions often become coarse, fragmented, or misaligned in small and overlapping bones.

### F.1.2 Segmentation of Overlapping Regions

Quantitative results for anatomically overlapping regions are shown in Table 14 and Table 15, with qualitative examples provided in Fig. 13 and Fig. 14. Compared with the overall bone-wise results in Table 12 and Table 13, overlap-specific performance drops substantially, showing that projection overlap is one of the main bottlenecks in hand bone structure segmentation. While supervised models reach more than 97% Bone Mean DSC on all bones, their overlap DSC values are much lower, and several difficult bone pairs fall below 60%.

The difficulty varies across anatomical pairs. Relatively simple overlaps, such as Cap-Sca, Radius-Lu, Ham-MC5, and Tm-Td, obtain high DSC values for the best supervised models. For example, SwinUMamba achieves 89.55% on Cap-Sca, 89.10% on Ham-MC5, and 91.29% on Tm-Td, while SwinUNETR achieves 88.24% on Radius-Lu. These results indicate that current models can handle some overlap regions when the local anatomical structure remains clear. In contrast, severe overlap

Table 14: Overlap DSC performance on overlapping regions. The best results in each column are highlighted in **bold**, and the second-best values are underlined.

Model	Cap-Sca	Cap-Td	Cap-MC3	Radius-Lu	Radius-Sca	Ham-MC4	Ham-MC5
<b>Supervised Models</b>							
UNet	87.31±10.90	62.96±23.94	49.57±24.83	85.80±12.88	83.25±11.98	64.95±22.20	87.20±6.99
UNet++	88.70±10.91	64.52±23.23	55.41±24.21	87.75±12.80	84.54±12.22	65.31±22.37	87.51±6.39
SegFormer	85.33±10.83	61.65±22.59	48.49±24.80	84.53±12.99	81.21±12.07	61.57±21.51	84.73±6.95
TransUNet	89.25±10.80	65.64±23.37	<b>57.34±23.73</b>	88.20±11.62	85.41±11.17	64.71±22.23	88.11±6.34
SwinUNETR	89.26±10.28	64.81±24.40	57.03±24.18	<b>88.24±12.55</b>	85.32±11.50	65.73±22.66	88.50±6.28
UMambaEnc	89.37±10.27	<b>65.69±24.54</b>	56.35±23.43	88.17±11.95	<u>85.67±10.97</u>	<b>67.21±21.34</b>	87.89±7.47
SwinUMamba	<b>89.55±10.82</b>	64.60±22.95	54.63±24.60	87.24±11.90	<b>86.19±10.82</b>	63.46±22.96	<b>89.10±5.91</b>
MambaVision	81.15±11.35	57.98±24.41	41.88±21.92	76.29±13.03	74.88±11.55	53.89±19.36	81.73±7.68
<b>Foundation Models</b>							
SAM(Box)	8.08±21.36	1.06±6.35	0.00±0.00	0.03±0.46	0.89±5.02	0.00±0.03	1.38±6.62
SAM(Point)	2.41±6.57	0.54±1.85	0.12±0.80	0.11±0.52	1.20±4.48	0.21±1.58	2.92±8.72
MedSAM(Box)	13.53±25.04	2.50±9.72	0.88±4.46	32.57±24.80	24.45±22.48	0.10±1.16	2.60±9.52

Model	Lu-Sca	Sca-Tm	Tm-Td	Tm-MC1	Tm-MC2	Td-MC2	MC2-MC3
<b>Supervised Models</b>							
UNet	72.15±20.51	72.49±22.39	90.27±9.04	75.92±17.86	81.30±13.94	40.83±23.72	71.15±15.33
UNet++	73.04±21.30	75.95±19.06	90.32±8.79	77.96±17.93	82.67±13.42	41.30±23.68	73.39±15.34
SegFormer	69.51±21.94	71.14±20.24	89.26±7.54	74.61±16.82	78.26±14.18	36.47±22.59	68.50±15.32
TransUNet	75.13±20.68	76.08±19.16	90.97±6.85	78.40±16.34	83.03±12.63	42.01±23.34	74.59±15.48
SwinUNETR	74.61±20.01	<b>77.36±19.68</b>	90.95±8.88	78.20±18.11	83.43±13.22	<u>43.09±24.21</u>	74.53±14.63
UMambaEnc	74.18±20.32	76.50±19.72	90.97±7.75	78.62±17.59	83.59±11.86	42.21±23.77	73.54±15.22
SwinUMamba	<b>75.51±21.41</b>	75.36±19.76	<b>91.29±7.39</b>	<b>79.19±16.90</b>	<b>84.30±12.25</b>	<b>46.11±25.04</b>	<b>75.22±15.12</b>
MambaVision	62.40±23.29	66.34±20.10	87.66±8.88	65.21±18.48	76.81±13.97	33.08±22.12	63.01±14.20
<b>Foundation Models</b>							
SAM(Box)	7.01±16.36	1.60±7.68	52.86±14.47	1.00±6.49	5.14±10.60	1.72±5.63	0.00±0.00
SAM(Point)	1.80±4.36	0.99±2.84	27.22±14.68	0.62±3.51	6.93±10.89	1.34±3.21	0.01±0.06
MedSAM(Box)	3.29±11.78	1.87±8.95	49.71±29.48	7.20±12.84	4.61±12.89	2.73±7.15	0.49±3.74

Table 15: Overlap NSD performance on overlapping regions. The best results in each column are highlighted in **bold**, and the second-best values are underlined.

Model	Cap-Sca	Cap-Td	Cap-MC3	Radius-Lu	Radius-Sca	Ham-MC4	Ham-MC5
<b>Supervised Models</b>							
UNet	80.24±17.63	70.53±26.21	67.18±25.00	77.34±19.49	77.69±18.74	70.97±27.15	80.27±15.83
UNet++	84.39±16.05	73.21±24.91	70.79±24.41	81.41±18.85	79.38±17.31	72.04±26.62	80.99±15.38
SegFormer	74.55±18.24	67.72±24.68	67.21±23.89	74.76±18.86	74.06±17.29	67.20±25.79	73.83±16.81
TransUNet	85.34±16.45	73.18±26.09	71.51±24.29	82.21±18.28	82.00±17.99	72.55±25.98	82.81±15.13
SwinUNETR	84.87±16.83	72.91±25.43	71.21±25.32	<b>82.52±18.78</b>	81.81±16.53	72.70±27.02	<b>83.79±14.87</b>
UMambaEnc	85.16±16.02	<b>74.25±25.93</b>	<b>72.26±24.39</b>	82.48±18.29	81.82±16.56	<b>73.65±26.93</b>	82.26±16.08
SwinUMamba	<b>86.21±16.43</b>	73.50±25.03	71.86±24.44	78.72±19.22	<b>82.51±18.71</b>	72.11±27.05	85.91±14.02
MambaVision	63.42±19.83	63.95±26.13	60.39±24.54	59.27±19.73	63.08±19.05	58.41±25.32	64.87±18.52
<b>Foundation Models</b>							
SAM(Box)	6.67±15.26	1.71±7.70	0.02±0.34	0.07±1.20	1.53±4.89	0.00±0.00	2.78±9.44
SAM(Point)	3.12±8.42	1.69±4.55	0.80±3.34	0.25±1.30	2.47±6.44	0.47±2.06	3.86±8.73
MedSAM(Box)	11.54±15.79	5.59±13.10	1.87±7.78	16.85±12.86	16.04±12.69	0.53±3.57	3.55±9.03

Model	Lu-Sca	Sca-Tm	Tm-Td	Tm-MC1	Tm-MC2	Td-MC2	MC2-MC3
<b>Supervised Models</b>							
UNet	66.02±26.99	72.09±26.71	74.54±17.65	79.94±20.52	69.66±21.88	59.20±31.21	75.55±19.23
UNet++	68.97±27.56	77.07±23.58	74.89±17.54	82.66±20.64	71.85±21.36	59.95±32.04	79.90±18.33
SegFormer	62.74±26.44	70.72±24.50	67.47±17.33	77.10±19.72	61.76±20.63	57.24±31.40	73.87±17.97
TransUNet	72.75±26.21	75.34±24.99	75.67±17.09	83.59±18.55	73.04±20.46	59.65±31.42	80.80±18.09
SwinUNETR	70.66±26.42	<b>78.71±23.34</b>	77.04±17.76	83.14±19.68	74.59±21.53	61.43±31.32	<b>80.93±18.75</b>
UMambaEnc	71.64±26.16	78.40±23.95	76.15±17.08	<b>83.61±19.53</b>	74.61±20.17	60.61±31.77	79.97±18.58
SwinUMamba	<b>73.91±25.96</b>	78.10±23.87	<b>77.54±16.93</b>	84.77±18.78	<b>76.82±20.65</b>	<b>61.82±32.34</b>	81.75±19.06
MambaVision	54.59±25.07	60.66±25.57	60.97±16.95	64.36±20.78	56.63±21.64	51.65±30.93	68.36±19.40
<b>Foundation Models</b>							
SAM(Box)	8.20±14.51	2.13±7.78	23.74±13.54	1.30±6.46	6.95±12.42	3.77±10.89	0.00±0.00
SAM(Point)	3.73±7.47	2.81±6.82	7.19±7.57	1.22±5.38	7.64±11.34	4.81±8.77	0.05±0.46
MedSAM(Box)	2.63±8.02	2.81±8.43	22.04±16.66	11.03±14.27	4.59±10.24	6.18±12.02	1.16±6.40

Table 16: Spearman correlation results between bone segmentation-derived overlap size and the ground-truth total SvdH JSN score on the Test set. Significance levels:  $*p < 0.05$ ,  $**p < 0.01$ ,  $***p < 0.001$ .

Model	Spearman $\rho$	$p$ -value	Significance
<b>Supervised Models</b>			
Unet	-0.1234	0.0440	*
Unet++	-0.1184	0.0533	–
SegFormer	-0.1251	0.0411	*
TransUNet	-0.1163	0.0576	–
SwinUNETR	-0.1193	0.0515	–
UMambaEnc	-0.1198	0.0506	–
SwinUMamba	-0.1195	0.0511	–
MambaVision	-0.1063	0.0830	–
<b>Foundation Models</b>			
SAM(Box)	-0.1270	0.0382	*
SAM(Point)	0.0704	0.2516	–
MedSAM(Box)	0.0246	0.6896	–

pairs show much lower performance. Cap-MC3, Ham-MC4, and Td-MC2 are particularly difficult, with the best DSC values reaching only 57.34%, 67.21%, and 46.11%, respectively. These regions involve weak boundaries and heavy superimposition, making accurate separation of adjacent bones difficult.

Among supervised models, SwinUMamba provides the most balanced performance across overlapping regions. It achieves the best DSC on several representative pairs, including Cap-Sca, Radius-Sca, Ham-MC5, Lu-Sca, Tm-Td, Tm-MC1, Tm-MC2, Td-MC2, and MC2-MC3. UMambaEnc is also competitive, achieving the best DSC on Cap-Td and Ham-MC4, while SwinUNETR performs best on Radius-Lu and Sca-Tm. This suggests that models with stronger contextual modeling and boundary representation are more robust under anatomical ambiguity.

The NSD results in Table 15 further highlight the importance of boundary accuracy. SwinUMamba achieves the best NSD on many overlap pairs, including Cap-Sca, Radius-Sca, Ham-MC5, Lu-Sca, Tm-Td, Tm-MC1, Tm-MC2, Td-MC2, and MC2-MC3. However, even the best NSD values remain far below the corresponding whole-bone NSD values in Table 13, showing that overlap regions are highly sensitive to boundary shifts. Qualitative results in Fig. 13 and Fig. 14 show the same pattern: errors are concentrated around the wrist and metacarpal bases, where models may merge neighboring bones, leak across boundaries, or miss thin visible structures.

Foundation models perform poorly in overlap-specific evaluation. In Table 14 and Table 15, SAM(Box), SAM(Point), and MedSAM(Box) obtain near-zero values on many overlap pairs, especially Cap-MC3, Ham-MC4, and MC2-MC3. Although MedSAM(Box) performs slightly better on some larger overlaps, such as Radius-Lu and Tm-Td, it remains far below supervised models. This confirms that prompt-based foundation models do not reliably resolve fine-grained anatomical overlap in hand radiographs.

Overall, the results indicate that supervised models already achieve strong performance for general hand bone structure segmentation, especially on large bones and clearly visible anatomical regions. The remaining challenges are therefore concentrated less on coarse whole-bone localization and more on fine-grained anatomical details, including small structures, subtle boundary variations, and instance separation in densely arranged regions. In particular, overlapping regions remain the main bottleneck: although current models can recover the overall hand skeleton, they still struggle to assign accurate boundaries when adjacent bones are heavily superimposed. Future work should therefore focus on overlap-aware and anatomy-aware segmentation, for example by introducing stronger boundary supervision, anatomical relationship modeling, topology-aware constraints, or prior-guided strategies that improve the separation of neighboring bones under projection ambiguity.

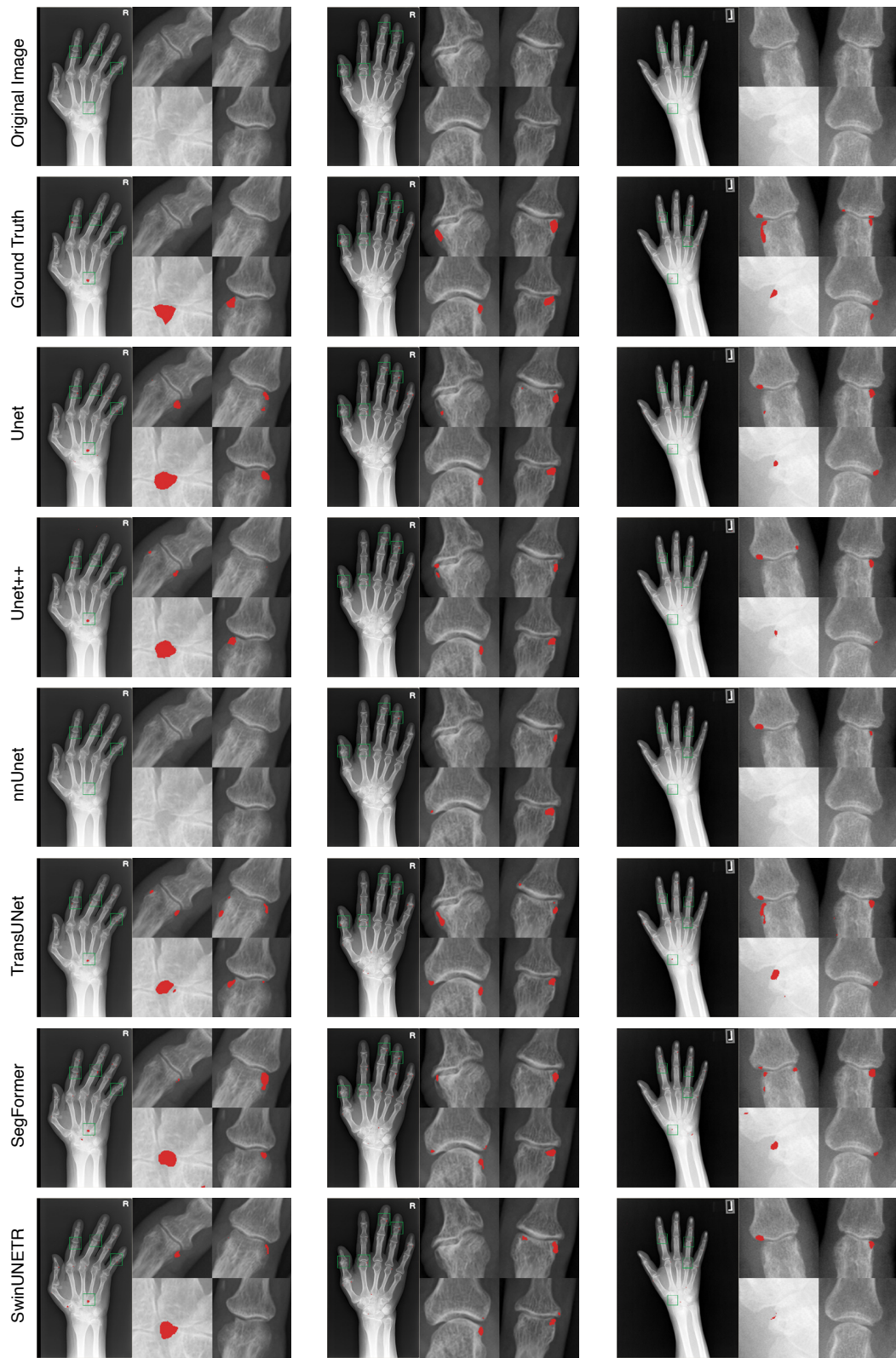


Figure 15: SvdH-BE-90 segmentation results (A).

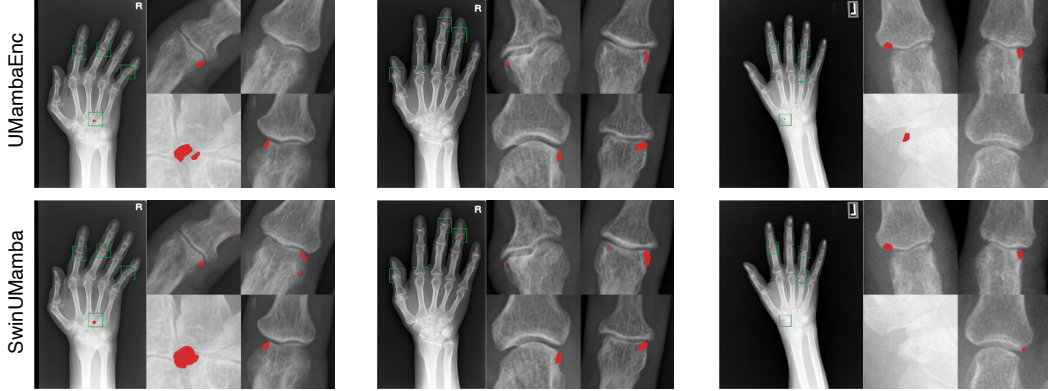


Figure 16: SvdH-BE-90 segmentation results (B).

### E.1.3 Correlation Analysis Between Bone Segmentation-Derived Overlap Size and Ground-Truth Total SvdH JSN Score

The clinical relevance of overlap size was evaluated using Spearman’s rank correlation analysis with the total JSN score. As summarized in Table 16, the associations between predicted overlap size and total JSN score were generally weak across models. Among the supervised models, Unet ( $\rho = -0.1234$ ,  $p = 0.0440$ ) and SegFormer ( $\rho = -0.1251$ ,  $p = 0.0411$ ) showed statistically significant correlations, whereas the remaining supervised models did not reach statistical significance. For the foundation models, SAM(Box) also exhibited a weak but significant negative correlation ( $\rho = -0.1270$ ,  $p = 0.0382$ ), while SAM(Point) and MedSAM(Box) showed no significant association.

These findings indicate that predicted overlap size alone has limited monotonic association with total JSN severity. Although several models reached nominal statistical significance, the small absolute correlation coefficients suggest that overlap size is not a strong standalone surrogate for JSN score. This may be because the total JSN score reflects localized joint-space narrowing patterns, whereas overlap size represents a global area-based measurement. Therefore, overlap size should be interpreted as a complementary structural descriptor rather than a direct proxy for JSN severity.

## E.2 Hand BE Segmentation

We evaluate BE segmentation using two complementary settings: SvdH-BE-90 and multi-class BE segmentation. The former focuses on high-confidence, clinically defined erosions, while the latter includes multiple BE categories (e.g., SvdH-BE-90, SvdH-BE-50, and Non-SvdH-BE), reflecting different confidence levels and definition criteria. Results from both settings show that BE segmentation remains highly challenging due to small lesion size, low contrast, and ambiguous boundaries. Together, these two protocols provide a more comprehensive evaluation, covering both reliable clinical targets and broader erosion patterns.

### E.2.1 SvdH-BE-90 Segmentation

Qualitative results for SvdH-BE-90 segmentation are shown in Fig. 15 and Fig. 16. The visual comparisons show that SvdH-defined erosion segmentation remains highly challenging even when models are trained specifically for this task. Across different cases, the predicted masks are generally sparse and unstable, and many small erosion regions are either missed or only partially detected. This is particularly evident in low-contrast regions, where the boundary between true cortical erosion and normal anatomical variation is visually ambiguous.

The results also reveal a strong tendency toward either under-detection or over-segmentation. Some models produce conservative predictions and miss subtle erosion regions, while others generate scattered false-positive masks around cortical edges, joint spaces, or overlapping bone structures. This indicates that SvdH-BE-90 segmentation is not only a small-target segmentation problem, but also a fine-grained discrimination problem: the model must distinguish clinically meaningful erosions from normal radiographic irregularities. In Fig. 15 and Fig. 16, even relatively successful predictions

Table 17: Multi-class BE segmentation results obtained on the Test set.

Model	DSC $\uparrow$ (%)	NSD $\uparrow$ (%)	REC $\uparrow$ (%)	PREC $\uparrow$ (%)	VOE $\downarrow$ (%)	MSD $\downarrow$ (pix)	#P (M)	Time (ms)
Unet	12.78 $\pm$ 11.41	8.22 $\pm$ 7.08	9.58 $\pm$ 10.01	7.27 $\pm$ 7.37	92.45 $\pm$ 7.62	<b>206.61<math>\pm</math>106.07</b>	7.94	365.42
Unet++	<b>14.48<math>\pm</math>10.80</b>	9.65 $\pm$ 7.16	11.72 $\pm$ 9.90	<b>7.96<math>\pm</math>7.81</b>	91.48 $\pm$ 6.96	<b>220.90<math>\pm</math>99.59</b>	2.41	772.82
TransUNet	<b>14.53<math>\pm</math>11.71</b>	9.59 $\pm$ 8.06	14.16 $\pm$ 11.64	7.10 $\pm$ 7.72	<b>91.28<math>\pm</math>8.30</b>	236.23 $\pm$ 109.68	105.32	849.10
SegFormer	9.75 $\pm$ 9.41	6.18 $\pm$ 5.70	10.37 $\pm$ 10.24	4.60 $\pm$ 5.80	94.35 $\pm$ 6.35	231.40 $\pm$ 99.01	21.88	272.00
SwinUNETR	13.13 $\pm$ 10.16	7.78 $\pm$ 5.96	13.03 $\pm$ 11.05	6.17 $\pm$ 5.96	92.36 $\pm$ 6.53	230.94 $\pm$ 100.65	25.14	826.32
UMambaEnc	14.14 $\pm$ 10.41	8.46 $\pm$ 6.26	<b>15.38<math>\pm</math>11.99</b>	6.20 $\pm$ 5.82	91.76 $\pm$ 7.06	239.12 $\pm$ 96.71	4.58	780.26
SwinUMamba	12.25 $\pm$ 9.68	<b>10.72<math>\pm</math>8.27</b>	11.11 $\pm$ 10.16	5.76 $\pm$ 5.70	92.95 $\pm$ 6.06	226.17 $\pm$ 103.98	59.89	1361.45

Table 18: Segmentation results of three categories of BE on the Test set. (a) DSC (%), (b) NSD (%).

Model	SvdH-BE-90	SvdH-BE-50	Non-SvdH-BE	Model	SvdH-BE-90	SvdH-BE-50	Non-SvdH-BE
Unet	15.55 $\pm$ 12.83	7.70 $\pm$ 11.21	22.98 $\pm$ 27.89	Unet	16.15 $\pm$ 14.46	5.43 $\pm$ 9.26	2.79 $\pm$ 12.76
Unet++	<b>18.50<math>\pm</math>12.17</b>	8.06 $\pm$ 13.43	21.13 $\pm$ 23.72	Unet++	<b>18.07<math>\pm</math>13.95</b>	5.65 $\pm$ 11.01	3.26 $\pm$ 12.03
TransUNet	16.81 $\pm$ 11.42	<b>9.74<math>\pm</math>14.67</b>	<b>32.15<math>\pm</math>32.49</b>	TransUNet	16.62 $\pm$ 12.88	<b>5.82<math>\pm</math>10.43</b>	<b>4.89<math>\pm</math>17.90</b>
SegFormer	11.67 $\pm$ 9.47	5.58 $\pm$ 9.86	24.32 $\pm$ 28.44	SegFormer	12.04 $\pm$ 10.65	3.68 $\pm$ 7.05	2.65 $\pm$ 11.31
SwinUNETR	16.81 $\pm$ 11.83	6.89 $\pm$ 11.11	24.84 $\pm$ 22.11	SwinUNETR	16.58 $\pm$ 13.39	4.30 $\pm$ 7.80	2.46 $\pm$ 9.19
UMambaEnc	16.61 $\pm$ 11.44	9.67 $\pm$ 12.21	22.17 $\pm$ 24.87	UMambaEnc	16.56 $\pm$ 12.92	<b>6.09<math>\pm</math>9.34</b>	2.53 $\pm$ 10.93
SwinUMamba	<u>17.03<math>\pm</math>11.79</u>	7.23 $\pm$ 12.37	-	SwinUMamba	<u>17.09<math>\pm</math>13.35</u>	4.98 $\pm$ 8.80	-

often show imperfect boundary alignment, suggesting that lesion localization and precise contour delineation remain difficult to optimize simultaneously.

Future work should therefore focus on improving the balance between sensitivity and false-positive control for clinically defined BE regions. Promising directions include lesion-aware sampling, hard negative mining, boundary-sensitive supervision, and anatomy-guided segmentation. Incorporating bone structure priors or joint-level SvdH context may also help models distinguish true erosion regions from normal cortical variations and projection artifacts.

## F.2.2 Multi-class BE segmentation

Multi-class BE segmentation results are summarized in Table 17 and Table 18, with qualitative examples shown in Fig. 17 and Fig. 18. Compared with SvdH-BE-90 segmentation alone, the multi-class setting is more difficult because the model must simultaneously segment SvdH-BE-90, SvdH-BE-50, and Non-SvdH-BE regions. As shown in Table 17, all models obtain low overall performance, with the best DSC reaching only 14.53% for TransUNet and the best NSD reaching 10.72% for SwinUMamba. These results indicate that separating different erosion categories remains highly challenging.

Different models show different strengths across metrics. TransUNet achieves the best overall DSC and VOE, suggesting relatively better region overlap, while SwinUMamba obtains the highest NSD, indicating better boundary agreement. UMambaEnc reaches the highest recall of 15.38%, showing stronger sensitivity to possible erosion regions, whereas UNet++ achieves the highest precision of 7.96%. However, the absolute precision and recall values remain low for all models, showing that multi-class BE segmentation is still dominated by missed detections and false positives.

The class-wise results in Table 18 further show that different BE categories have different levels of difficulty. SvdH-BE-90 is the most stable category, with UNet++ achieving the best DSC of 18.50% and NSD of 18.07%. In contrast, SvdH-BE-50 is more difficult, with the best DSC only reaching 9.74% and the best NSD only 6.09%. Non-SvdH-BE obtains a higher DSC for some models, especially TransUNet with 32.15%, but its NSD remains low, indicating that models may capture approximate lesion areas without accurately delineating their boundaries. The qualitative results in Fig. 17 and Fig. 18 are consistent with this pattern, showing frequent category confusion, missed small lesions, and scattered predictions around anatomically complex regions.

Future work on multi-class BE segmentation should address both lesion detection and category discrimination. Beyond improving binary erosion localization, models need stronger clinical and anatomical priors to distinguish SvdH-defined erosions from non-SvdH erosive changes. Multi-task learning with bone segmentation, joint ROI localization, or SvdH scoring may provide useful contextual constraints. In addition, class-balanced optimization, uncertainty-aware supervision, and category-specific hard example mining may help reduce confusion between visually similar BE categories.

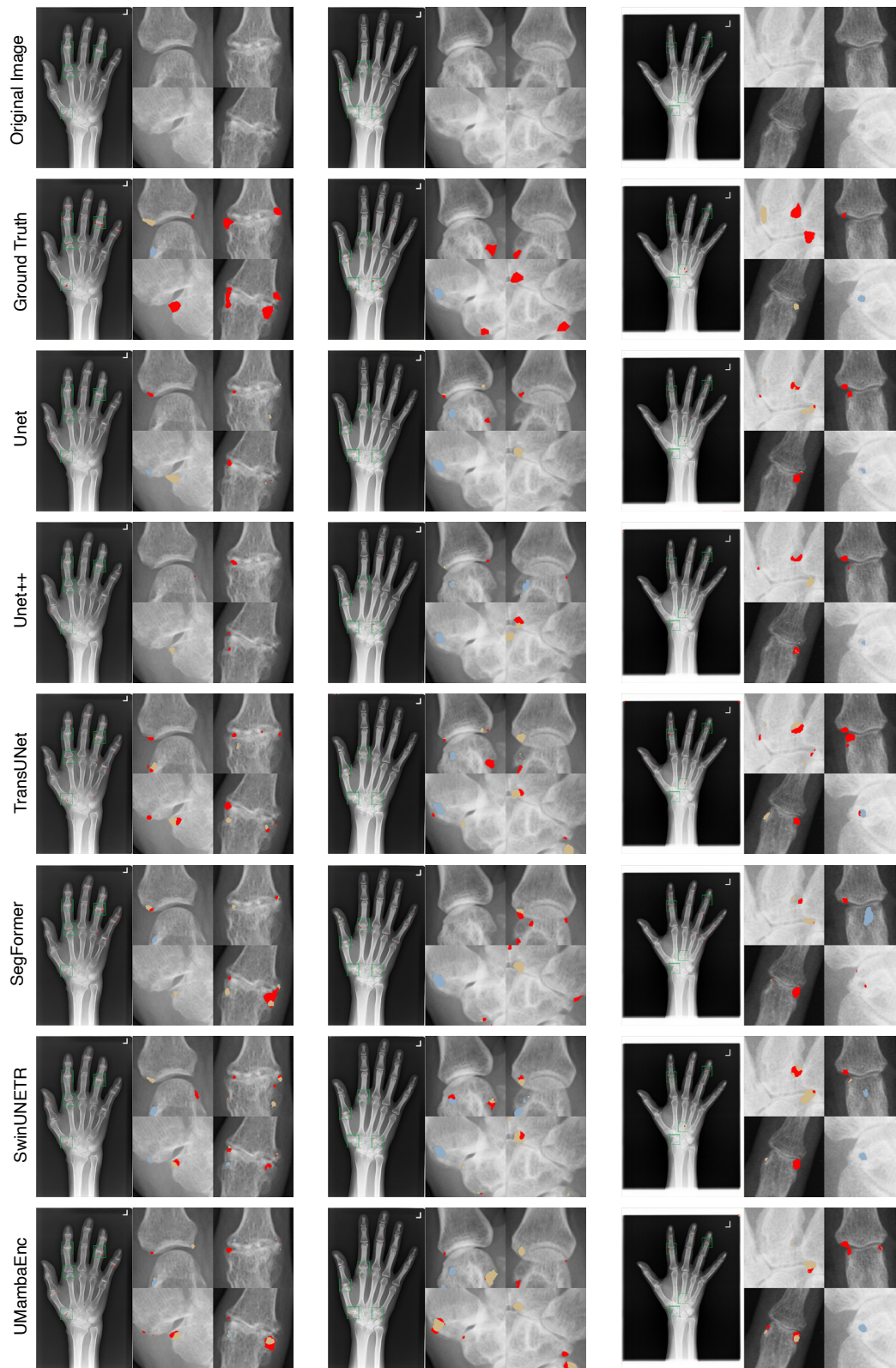


Figure 17: Multi-class BE segmentation results (A).

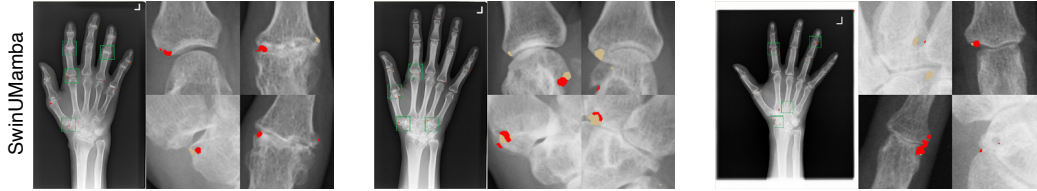


Figure 18: Multi-class BE segmentation results (B).

Table 19: Spearman correlation results between predicted BE size and the ground-truth total SvdH BE score on the Test set. Significance levels:  $*p < 0.05$ ,  $**p < 0.01$ ,  $***p < 0.001$ .

Model	Spearman $\rho$	$p$ -value	Significance
Unet	0.3222	< 0.001	***
Unet++	0.2533	< 0.001	***
SegFormer	0.1358	0.0265	*
TransUNet	0.3980	< 0.001	***
SwinUNETR	0.1359	0.0264	*
UMambaEnc	0.3742	< 0.001	***
SwinUMamba	0.3279	< 0.001	***

### F.2.3 Correlation Analysis Between Predicted BE Size and Ground-Truth Total SvdH BE Score

The association between predicted BE size and the total BE score was further examined using Spearman’s rank correlation. As shown in Table 19, all BE segmentation models exhibited positive correlations with the total BE score, indicating that larger predicted erosion areas were generally associated with higher clinical erosion severity. The strongest correlations were observed for TransUNet ( $\rho = 0.3980$ ,  $p < 0.001$ ) and UMambaEnc ( $\rho = 0.3742$ ,  $p < 0.001$ ), followed by SwinUMamba ( $\rho = 0.3279$ ,  $p < 0.001$ ) and Unet ( $\rho = 0.3222$ ,  $p < 0.001$ ). In contrast, SegFormer and SwinUNETR showed weaker but still statistically significant associations ( $\rho = 0.1358$ ,  $p = 0.0265$  and  $\rho = 0.1359$ ,  $p = 0.0264$ , respectively).

These results suggest that predicted BE size captures clinically relevant information related to bone erosion severity. However, the moderate magnitude of the correlations indicates that BE size should not be regarded as a complete substitute for total BE score. This is expected because the clinical BE score reflects joint-specific erosion patterns and ordinal severity grades, whereas the predicted BE size is a global area-based measurement. Therefore, BE size can serve as a useful quantitative imaging descriptor complementary to established clinical scoring.

## F.3 Scoring of SvdH BE

### F.3.1 Joint-level Results and Confusion Matrices

Tables 20 and 21 report the joint-level QWK and BACC results for the SvdH BE scoring task on the test set. Overall, the results show clear heterogeneity across anatomical locations, indicating that BE scoring difficulty is strongly joint-dependent.

For joint-level QWK, the models show noticeable performance variation across anatomical sites. Higher agreement is generally observed for joints such as Lu, MCP-I, MCP-M, and Ulna, where several models achieve relatively strong ordinal consistency. In contrast, IP, CMC-T, PIP-S, and Tr are more challenging, with lower QWK values across many methods. Among the evaluated models, MedMamba achieves the best overall QWK reported in the Mean column and shows strong performance across several key joints, particularly MCP-T, MCP-I, PIP-I, and PIP-M. ResNet also demonstrates competitive joint-level ordinal agreement, especially on Ulna, Lu, MCP-I, MCP-M, and PIP-M, suggesting relatively robust performance across different joint types.

For joint-level BACC, the results show a similar pattern. ResNet obtains the highest overall BACC reported in the Mean column, indicating stronger balanced classification ability across joints, while MedMamba also achieves competitive performance and performs well on several MCP and PIP joints. In general, joints with clearer and more reliable visual patterns tend to achieve better BACC, whereas

Table 20: SvdH BE score classification QWK results for each joint on the Test set. The best results in each column are highlighted in **bold**, and the second-best values are underlined. Mean denotes the overall QWK computed over all BE scoring samples.

Model	Radius	Ulna	IP	Lu	MCP-T	MCP-I	MCP-M	MCP-R
ResNet	0.3032	<u>0.5499</u>	0.0490	0.6623	0.3796	<u>0.6758</u>	<b>0.5981</b>	0.3030
DenseNet	<b>0.4157</b>	<u>0.5603</u>	0.0978	<b>0.7208</b>	0.3160	0.6037	0.4368	0.3090
EfficientNetV2	<u>0.3733</u>	0.3754	0.0992	0.5226	0.3539	0.4233	<u>0.5582</u>	0.2219
MobileViT	0.2028	<b>0.6522</b>	0.0888	0.6346	<u>0.4151</u>	0.6387	<u>0.4208</u>	0.2594
LeViT	0.1547	0.2423	0.0330	0.4599	0.3505	0.4502	0.2458	0.1029
EfficientFormer	0.3162	0.4493	0.1205	0.5749	0.3877	0.5759	0.4158	<b>0.3358</b>
ConvNeXtV2	0.2126	0.3191	<b>0.2653</b>	0.4435	0.3752	0.6216	0.3226	0.1725
MedMamba	0.3364	0.5497	<u>0.1908</u>	<u>0.6781</u>	<b>0.5138</b>	<b>0.7087</b>	0.5275	<u>0.3214</u>
MambaVision	0.3561	<u>0.5793</u>	0.0740	0.5189	0.3660	0.6396	0.5094	0.3102

Model	MCP-S	CMC-T	PIP-I	PIP-M	PIP-R	PIP-S	Sca	Tr	Mean
ResNet	<b>0.5228</b>	0.1367	<u>0.3301</u>	<u>0.5011</u>	<b>0.3573</b>	0.2093	0.3063	0.2069	0.4408
DenseNet	0.4185	0.2770	<u>0.2665</u>	0.4488	0.2922	<b>0.2125</b>	<u>0.3294</u>	0.1039	0.3905
EfficientNetV2	0.3947	0.0967	0.2847	0.3472	0.1318	0.1209	0.1485	<b>0.3560</b>	0.3358
MobileViT	0.3514	0.1190	0.2594	0.4505	0.2184	0.1568	0.2846	0.0898	0.3920
LeViT	0.1354	-0.0347	0.0987	0.2821	0.0803	0.1029	0.1861	<u>0.2538</u>	0.2346
EfficientFormer	0.3942	<b>0.2956</b>	0.2464	0.4478	0.1914	0.1168	0.2703	0.2080	0.3504
ConvNeXtV2	0.3549	-0.0244	0.2650	0.4387	0.0693	0.1073	0.1316	0.2188	0.3058
MedMamba	0.3629	<u>0.2801</u>	<b>0.4392</b>	<b>0.5045</b>	<u>0.3188</u>	0.1936	<b>0.3622</b>	0.2331	<b>0.4522</b>
MambaVision	<u>0.4457</u>	0.1472	0.2087	0.3563	0.2618	0.1825	0.3098	0.1759	0.3667

Table 21: SvdH BE score classification BACC results (%) for each joint on the Test set. The best results in each column are highlighted in **bold**, and the second-best values are underlined. Mean denotes the overall BACC computed over all BE scoring samples.

Model	Radius	Ulna	IP	Lu	MCP-T	MCP-I	MCP-M	MCP-R
ResNet	25.07	<b>41.46</b>	19.55	31.51	41.54	38.20	<b>41.73</b>	36.99
DenseNet	<b>30.03</b>	25.81	20.15	<b>33.26</b>	40.77	34.44	<u>35.08</u>	<u>39.77</u>
EfficientNetV2	<u>29.53</u>	24.33	19.75	26.12	42.29	33.45	35.04	25.42
MobileViT	23.29	<u>39.86</u>	21.01	26.04	<u>43.71</u>	32.65	27.08	26.33
LeViT	23.45	26.87	20.00	22.40	42.69	26.70	25.83	25.99
EfficientFormer	21.49	36.13	20.11	24.30	42.71	27.21	26.17	32.71
ConvNeXtV2	24.74	31.65	<b>21.77</b>	19.69	42.59	33.58	26.20	26.16
MedMamba	25.07	29.89	<u>21.41</u>	28.18	<b>47.74</b>	<b>40.82</b>	25.41	34.12
MambaVision	23.95	30.99	20.00	30.89	41.12	33.57	31.23	<b>39.89</b>

Model	MCP-S	CMC-T	PIP-I	PIP-M	PIP-R	PIP-S	Sca	Tr	Mean
ResNet	<b>34.05</b>	21.52	27.29	37.38	<u>32.81</u>	21.18	26.60	<b>25.89</b>	<b>35.87</b>
DenseNet	<u>30.48</u>	<b>41.31</b>	31.25	<u>37.93</u>	29.48	<b>26.49</b>	21.46	21.53	33.06
EfficientNetV2	25.42	22.10	<u>33.43</u>	30.42	20.92	19.96	22.17	<u>25.87</u>	30.67
MobileViT	27.51	20.21	28.28	35.70	<b>33.70</b>	22.40	26.87	23.81	31.88
LeViT	25.63	19.85	22.24	22.45	26.08	20.06	22.95	24.77	25.66
EfficientFormer	27.03	<u>26.42</u>	21.55	34.46	23.65	20.81	22.13	22.27	27.32
ConvNeXtV2	25.30	20.46	31.52	33.76	20.86	18.67	20.83	22.79	28.15
MedMamba	25.54	20.29	<b>42.30</b>	<b>40.92</b>	31.89	<u>25.50</u>	<u>29.74</u>	23.65	<u>34.91</u>
MambaVision	25.58	21.14	26.47	25.73	25.48	21.99	<b>33.10</b>	24.46	30.59

smaller or anatomically ambiguous joints remain difficult. This suggests that BE scoring performance is affected not only by model architecture, but also by joint-specific anatomical structure and lesion characteristics.

The joint-wise confusion matrices in Figs. 19, 20, and 21 further illustrate these differences. Joints with better quantitative results show clearer diagonal patterns, while more difficult joints have predictions concentrated in the lower BE scores or scattered across neighboring classes. This indicates that many errors are related to under-recognition of positive or severe erosion grades, especially in joints where lesions are small, subtle, or visually ambiguous.

These joint-level results further confirm that BE score classification remains highly heterogeneous across anatomical locations. The relatively low performance on several small or ambiguous joints suggests that improving joint-specific feature learning and ordinal-aware classification is important

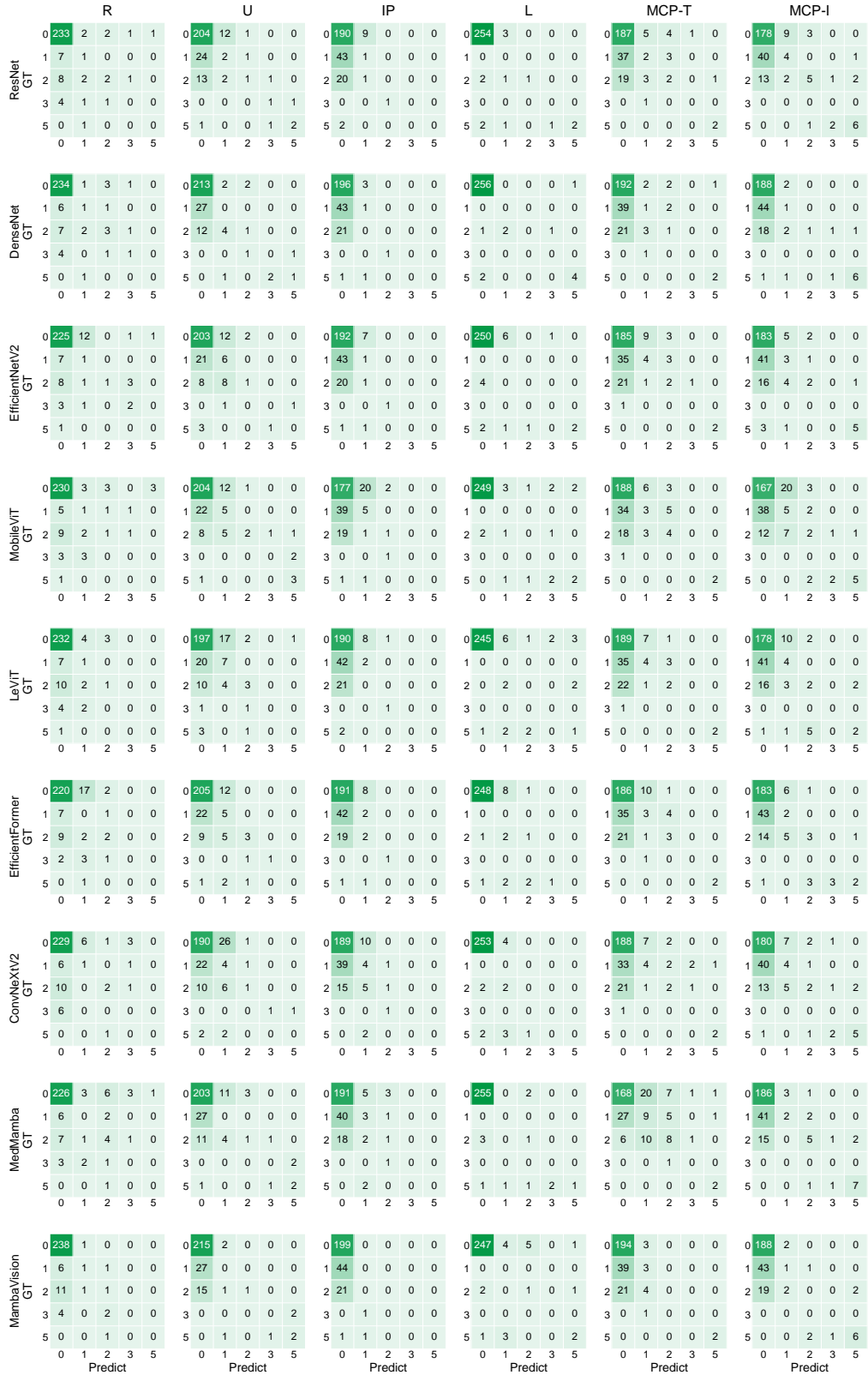


Figure 19: Joint-wise confusion matrices of SvdH BE scoring (A)

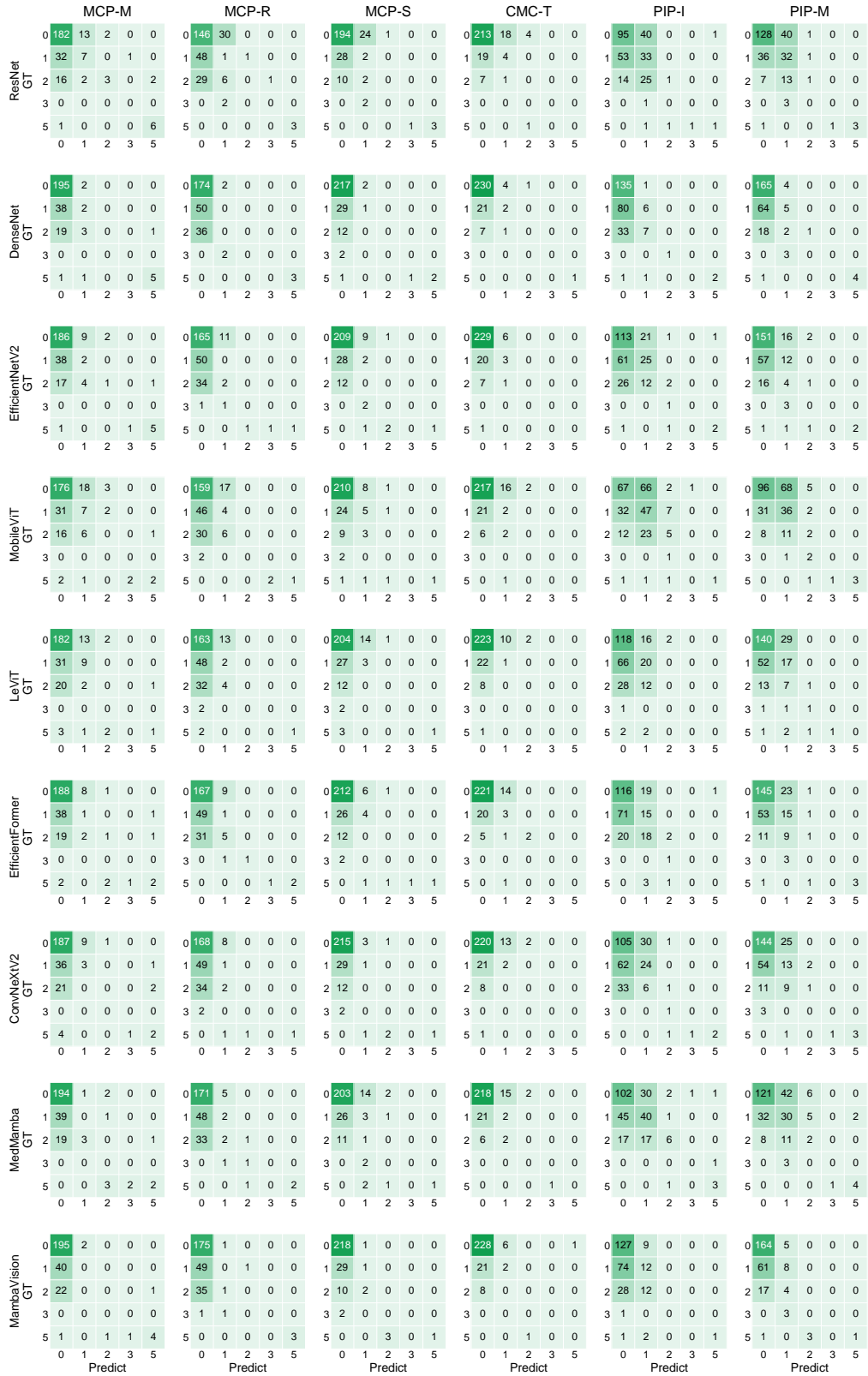


Figure 20: Joint-wise confusion matrices of SvdH BE scoring (B)

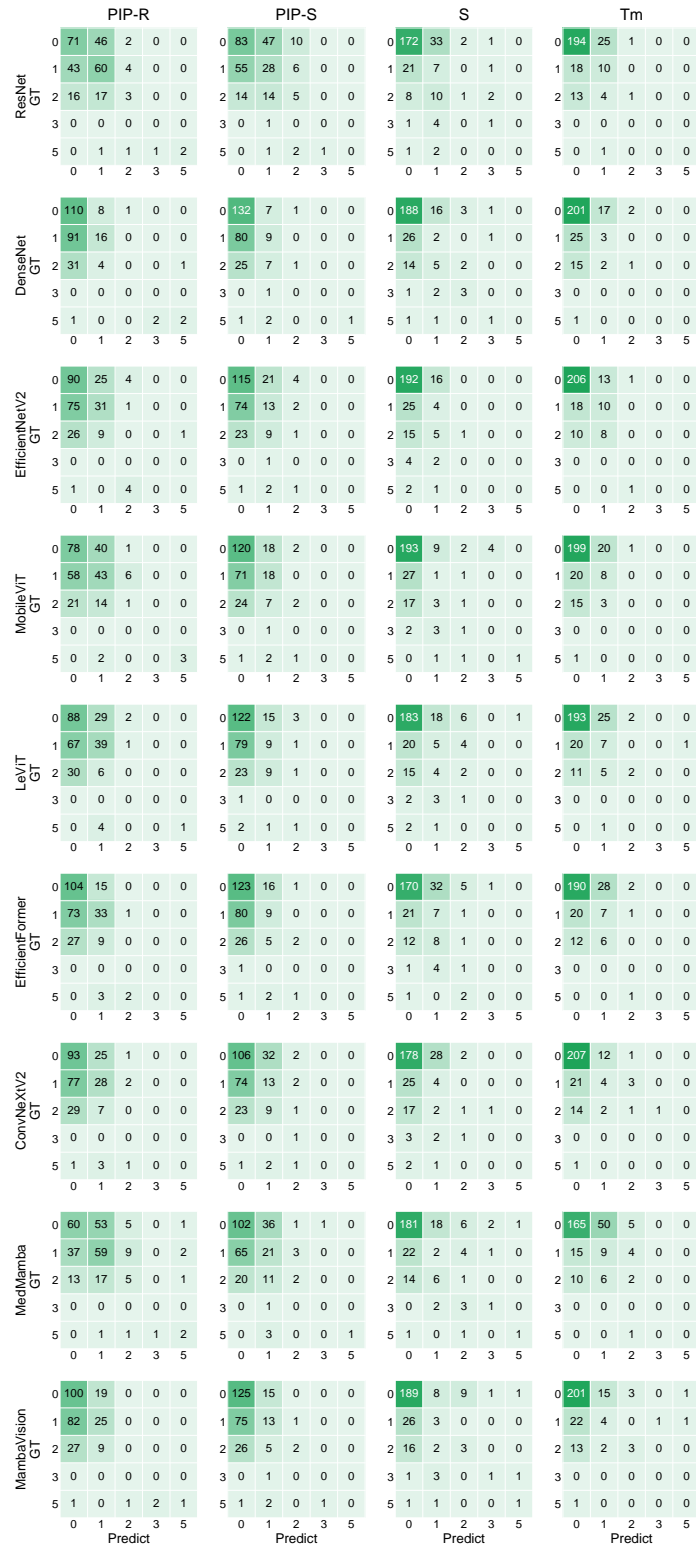


Figure 21: Joint-wise confusion matrices of SvdH BE scoring (C)

Table 22: Spearman correlation results between predicted SvdH BE scores and ground-truth SvdH BE scores on the Test set. Significance levels:  $*p < 0.05$ ,  $**p < 0.01$ ,  $***p < 0.001$ .

Model	Spearman $\rho$	$p$ -value	Significance
ResNet	0.4708	< 0.001	***
DenseNet	0.3447	< 0.001	***
EfficientNetV2	0.2923	< 0.001	***
MobileViT	0.4679	< 0.001	***
LeViT	0.3236	< 0.001	***
EfficientFormer	0.4120	< 0.001	***
ConvNeXtV2	0.3206	< 0.001	***
MedMamba	0.4692	< 0.001	***
MambaVision	0.5063	< 0.001	***

for more reliable BE assessment. Future work may benefit from anatomy-aware models that better capture local structural differences across hand and wrist regions. In addition, ordinal-aware loss functions, ranking-based learning strategies, and more effective class-imbalance handling may help reduce severe grading errors and improve recognition of underrepresented positive grades. Incorporating multi-joint contextual information, anatomical priors, and uncertainty estimation could further improve robustness for subtle or ambiguous erosive changes.

### F.3.2 Correlation Analysis Between Predicted and Ground-Truth SvdH BE Scores

To assess the consistency between model predictions and clinical evaluation, Spearman’s rank correlation analysis was conducted between the predicted BE scores and the reference total BE scores. As shown in Table 22, all models exhibited statistically significant positive correlations with the clinical BE scores ( $p < 0.001$ ), indicating that the predicted scores were generally aligned with expert annotations. The strongest association was achieved by MambaVision ( $\rho = 0.5063$ ), followed by ResNet ( $\rho = 0.4708$ ), MedMamba ( $\rho = 0.4692$ ), and MobileViT ( $\rho = 0.4679$ ). EfficientFormer also showed a moderate correlation ( $\rho = 0.4120$ ), whereas the remaining models demonstrated weaker but still significant associations.

These results suggest that the BE score prediction models capture clinically meaningful ranking information related to bone erosion severity. However, the correlations were moderate rather than high, indicating that model predictions are not fully interchangeable with expert-derived BE scores. This may reflect the ordinal and joint-specific nature of clinical BE scoring, as well as the difficulty of aggregating local erosion patterns into a total score. Therefore, predicted BE scores should be interpreted as clinically informative estimates rather than direct replacements for expert assessment.

## F.4 Scoring of SvdH JSN

### F.4.1 Joint-level Results and Confusion Matrices

Tables 23 and 24 report the joint-level QWK and BACC results for the SvdH JSN scoring task on the test set. Overall, the results show clear joint-dependent performance differences, suggesting that JSN scoring difficulty varies substantially across anatomical locations.

For joint-level QWK, the models show relatively high agreement on MCP joints and several wrist-related joints, indicating that JSN patterns in these regions can be captured more reliably. In particular, MCP-I, MCP-M, MCP-R, MCP-S, STT, SR, and CMC-M generally achieve stronger ordinal consistency across different architectures. In contrast, PIP joints, especially PIP-S, as well as CMC-R, are more challenging, with noticeably lower QWK values across many models. Among the evaluated methods, MobileViT achieves the best overall QWK reported in the Mean column, while ResNet, DenseNet, EfficientFormer, and MedMamba also show competitive joint-level ordinal agreement.

For joint-level BACC, the results follow a similar trend. MobileViT obtains the strongest overall BACC reported in the Mean column and performs well across both MCP and wrist-related joints, suggesting relatively robust classification ability under class imbalance. ResNet, LeViT, EfficientFormer, and MedMamba also achieve competitive BACC, showing that several architectures can provide reasonably balanced predictions across anatomical sites. However, performance remains

Table 23: SvdH JSN score classification QWK results for each joint on the Test set. The best results in each column are highlighted in **bold**, and the second-best values are underlined. Mean denotes the overall QWK computed over all JSN scoring samples.

Model	MCP-T	MCP-I	MCP-M	MCP-R	MCP-S	PIP-I	PIP-M	PIP-R
ResNet	<b>0.5400</b>	<u>0.9124</u>	0.7464	0.6870	0.6739	0.3068	0.5391	0.3344
DenseNet	0.4686	0.8513	0.7236	0.6918	0.6694	0.4250	0.4572	0.4241
EfficientNetV2	0.3823	0.9042	0.7207	0.5914	0.6612	0.5419	0.3261	0.4720
MobileViT	<u>0.5188</u>	<b>0.9129</b>	0.7759	<b>0.7211</b>	<b>0.7187</b>	0.3170	<b>0.5683</b>	0.3042
LeViT	0.4692	0.8438	<b>0.8382</b>	0.6800	<u>0.6742</u>	0.4127	0.4513	0.4056
EfficientFormer	0.4702	0.8763	0.7067	<u>0.7052</u>	0.6587	0.5310	<u>0.5397</u>	<b>0.5596</b>
ConvNeXtV2	0.4619	0.8968	<u>0.8130</u>	0.5962	0.4747	<u>0.5498</u>	0.4453	0.4645
MedMamba	0.4739	0.9033	0.7181	0.7001	0.6245	<b>0.5588</b>	0.5148	0.4405
MambaVision	0.5058	0.7873	0.7975	0.5752	0.5538	0.3477	0.4300	0.3408

Model	PIP-S	STT	SC	SR	CMC-M	CMC-R	CMC-S	Mean
ResNet	0.1058	<b>0.7203</b>	<b>0.5521</b>	<b>0.6464</b>	<u>0.5986</u>	0.3160	0.4843	0.5884
DenseNet	<u>0.3139</u>	<u>0.6853</u>	<u>0.5138</u>	0.6276	0.5669	<b>0.3856</b>	<b>0.5042</b>	0.5829
EfficientNetV2	<b>0.3676</b>	0.6686	0.3052	0.5380	0.4974	0.2186	0.4048	0.5393
MobileViT	0.1950	0.6754	0.4546	0.6171	<b>0.6316</b>	0.3370	0.4521	<b>0.5967</b>
LeViT	0.1214	0.5220	0.3236	0.5668	0.4214	<u>0.3760</u>	0.4691	0.5445
EfficientFormer	0.2928	0.6731	0.4889	<u>0.6283</u>	0.5886	0.2821	0.4644	<u>0.5919</u>
ConvNeXtV2	0.2189	0.4722	0.3581	0.4618	0.3070	0.1290	0.1737	0.5151
MedMamba	0.2960	0.6409	0.4303	0.6257	0.4956	0.2622	<u>0.4859</u>	0.5738
MambaVision	0.0988	0.6745	0.4678	0.6080	0.4954	0.3543	0.4741	0.5457

Table 24: SvdH JSN score classification BACC results (%) for each joint on the Test set. The best results in each column are highlighted in **bold**, and the second-best values are underlined. Mean denotes the overall BACC computed over all JSN scoring samples.

Model	MCP-T	MCP-I	MCP-M	MCP-R	MCP-S	PIP-I	PIP-M	PIP-R
ResNet	<u>50.75</u>	<u>55.49</u>	37.57	39.65	43.49	28.80	36.95	28.27
DenseNet	46.13	40.82	24.85	39.83	46.92	<b>29.54</b>	25.04	<u>36.02</u>
EfficientNetV2	44.97	<b>56.83</b>	27.69	23.83	39.15	27.16	19.80	27.82
MobileViT	<b>53.16</b>	54.08	35.43	<b>55.13</b>	<u>49.30</u>	25.74	32.70	21.68
LeViT	46.89	52.82	<u>41.57</u>	<u>49.83</u>	<b>53.58</b>	26.00	31.03	28.85
EfficientFormer	50.04	49.08	<b>42.19</b>	41.39	45.89	21.76	<b>41.37</b>	31.65
ConvNeXtV2	37.99	50.91	33.91	22.61	29.35	25.32	35.03	<b>39.21</b>
MedMamba	50.48	49.41	33.74	35.25	40.45	28.82	<u>39.21</u>	32.07
MambaVision	45.02	43.08	35.35	21.48	35.90	<u>29.49</u>	30.32	23.85

Model	PIP-S	STT	SC	SR	CMC-M	CMC-R	CMC-S	Mean
ResNet	20.53	41.09	31.56	32.32	32.52	26.56	<b>35.56</b>	39.51
DenseNet	22.01	32.53	31.56	35.52	36.41	<b>27.99</b>	<u>35.19</u>	36.44
EfficientNetV2	21.50	29.32	30.26	31.17	30.54	22.93	29.61	32.83
MobileViT	<u>22.51</u>	<u>43.62</u>	30.82	<b>57.83</b>	<b>56.84</b>	<u>27.24</u>	27.87	<b>42.80</b>
LeViT	21.07	34.17	<u>38.12</u>	<u>37.24</u>	<u>49.21</u>	25.76	31.52	<u>40.62</u>
EfficientFormer	21.42	33.31	33.69	28.92	35.61	25.12	33.01	39.25
ConvNeXtV2	21.78	29.48	25.55	25.04	22.42	21.39	23.56	32.51
MedMamba	<b>27.88</b>	38.10	32.86	30.43	25.57	25.11	26.16	38.66
MambaVision	19.97	<b>57.73</b>	<b>45.73</b>	32.06	40.37	27.14	32.40	34.62

uneven across joints, with some PIP and CMC joints showing lower balanced accuracy, indicating that class imbalance and subtle visual differences still affect JSN recognition.

The joint-wise confusion matrices in Figs. 22, 23, and 24 further illustrate these joint-specific patterns. Joints with stronger quantitative performance tend to show clearer diagonal alignment, while more difficult joints have predictions concentrated in lower JSN scores or confused between neighboring grades. This suggests that many errors come from mild or moderate narrowing cases, where the visual difference between adjacent JSN grades is subtle.

These joint-level results further show that JSN classification is highly joint-dependent. While several models achieve strong performance on MCP and wrist-related joints, smaller or more ambiguous joints remain difficult. Future work should therefore focus on ordinal-aware learning strategies that better preserve the ordered nature of JSN grades, together with joint-specific modeling approaches

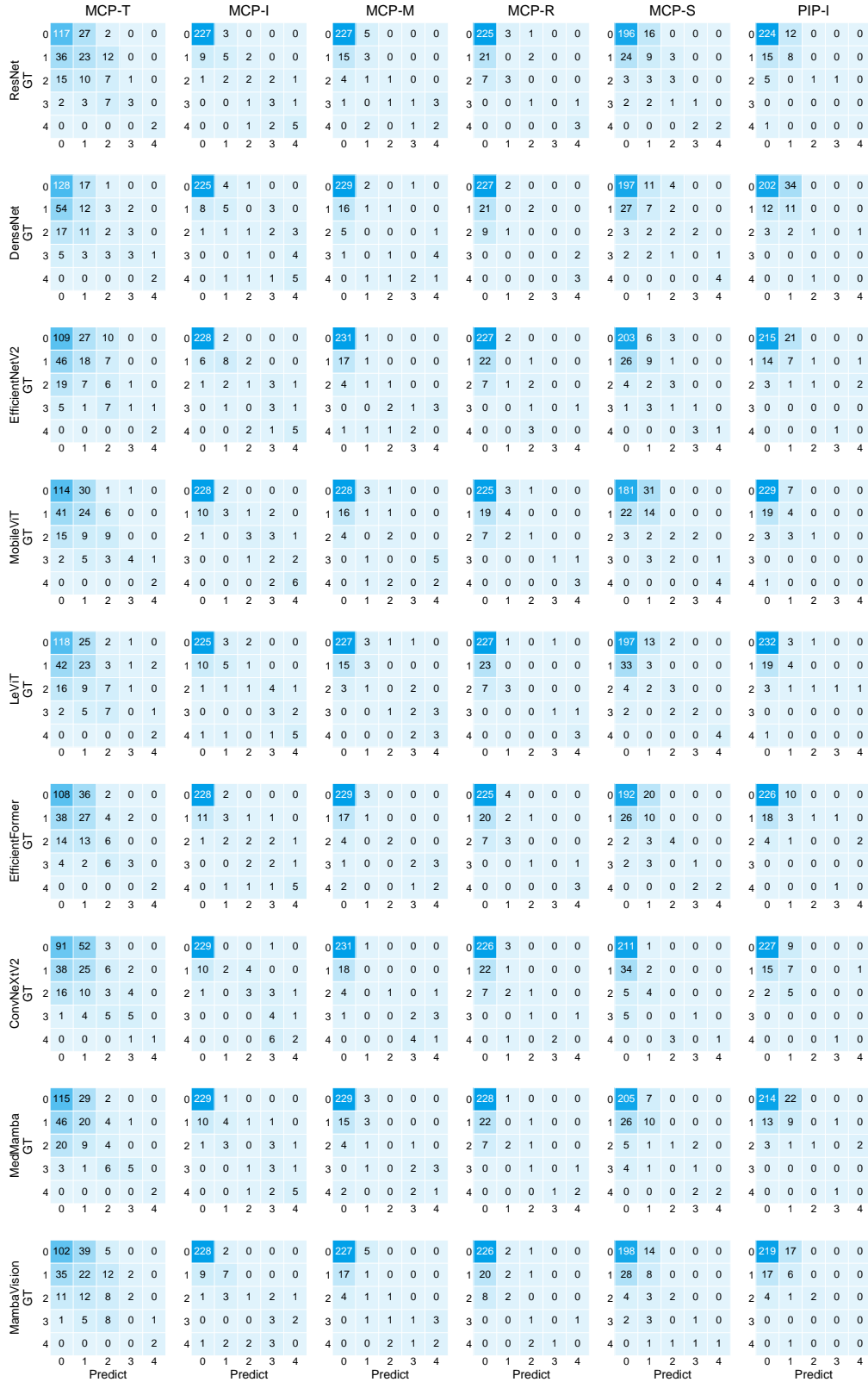


Figure 22: Joint-wise confusion matrices of SvdH JSN scoring (A).

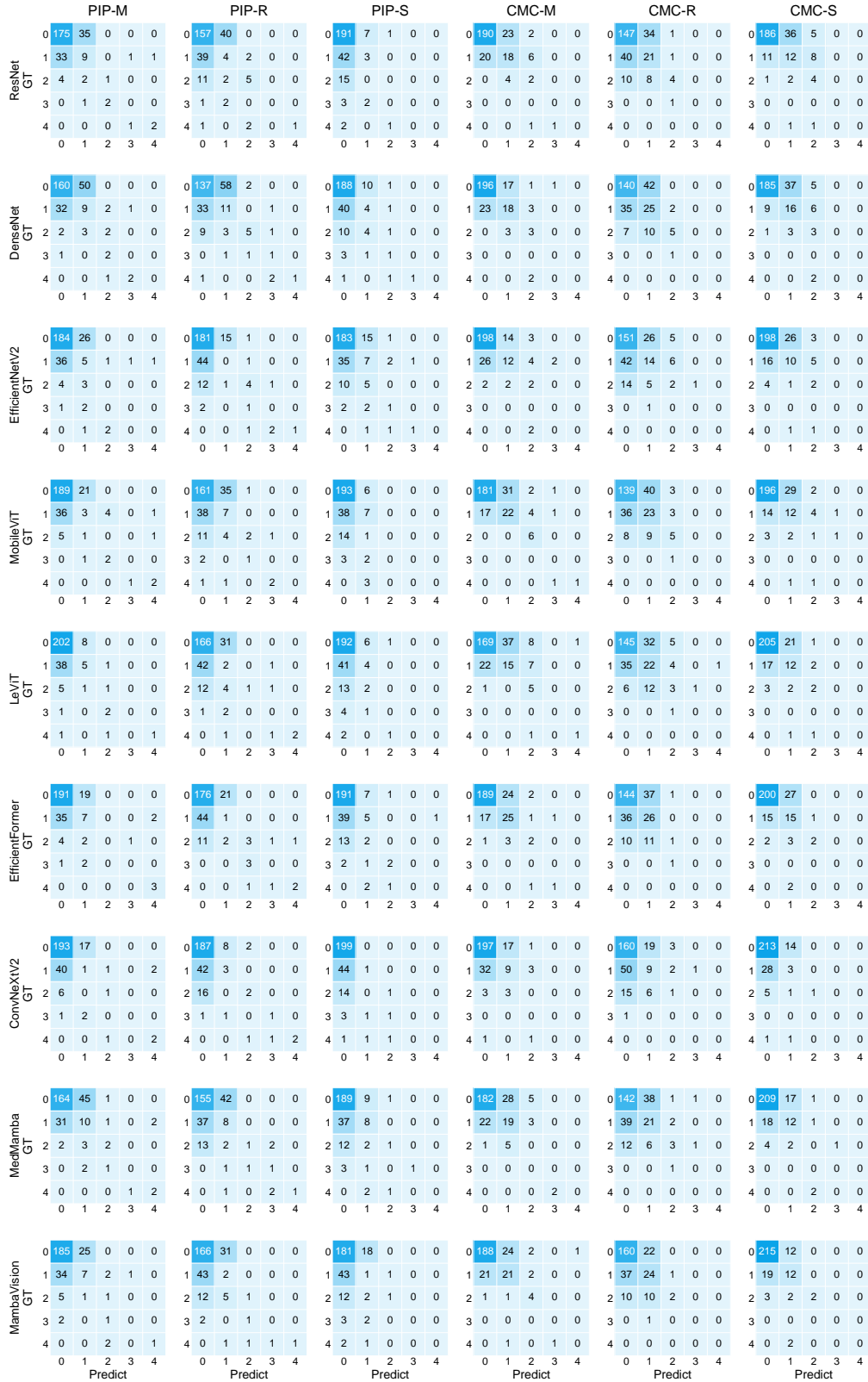


Figure 23: Joint-wise confusion matrices of SvdH JSN scoring (B).

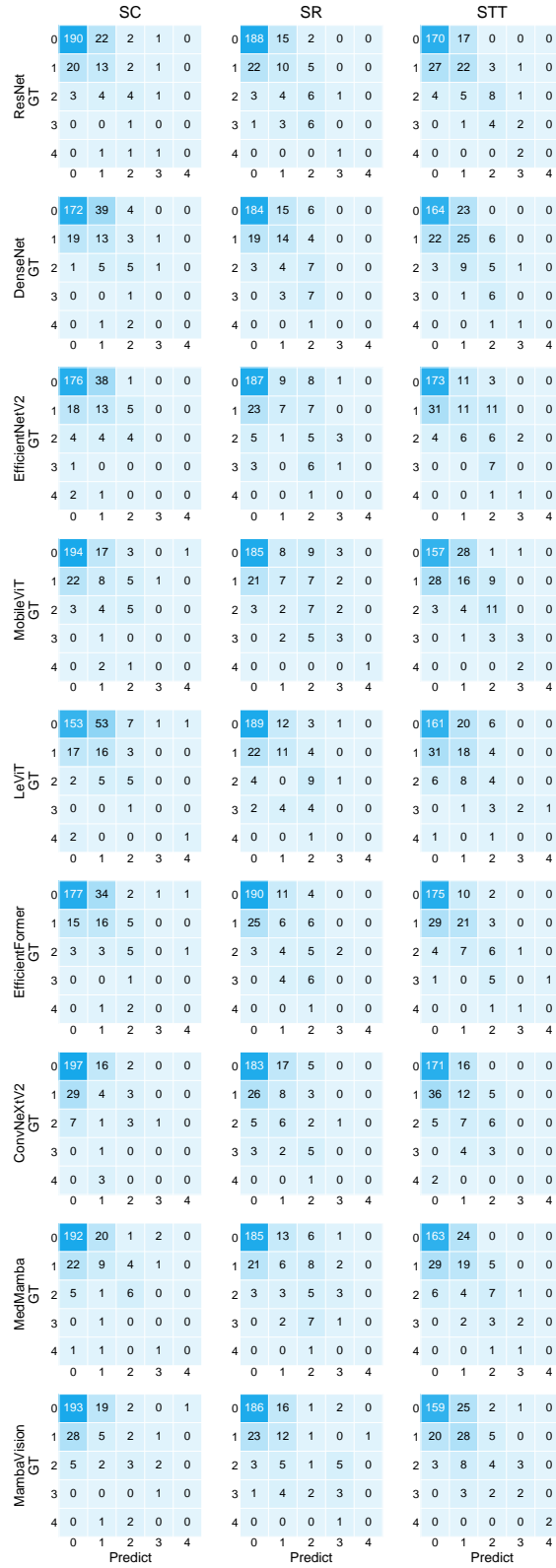


Figure 24: Joint-wise confusion matrices of SvdH JSN scoring (C).

Table 25: Spearman correlation results between predicted SvdH JSN scores and ground-truth SvdH JSN scores on the Test set. Significance levels: \* $p < 0.05$ , \*\* $p < 0.01$ , \*\*\* $p < 0.001$ .

Model	Spearman $\rho$	$p$ -value	Significance
ResNet	0.5610	< 0.001	***
DenseNet	0.5395	< 0.001	***
EfficientNetV2	0.5580	< 0.001	***
MobileViT	0.5765	< 0.001	***
LeViT	0.5658	< 0.001	***
EfficientFormer	0.5986	< 0.001	***
ConvNeXtV2	0.4792	< 0.001	***
MedMamba	0.5308	< 0.001	***
MambaVision	0.5184	< 0.001	***

that account for anatomical differences across regions. More effective solutions for class imbalance, such as cost-sensitive learning, adaptive re-weighting, or balanced sampling, may also help improve sensitivity to underrepresented positive grades. Incorporating anatomical priors, multi-joint contextual information, and uncertainty-aware prediction could further improve robustness, especially for subtle or ambiguous JSN changes.

#### F.4.2 Correlation Analysis Between Predicted and Ground-Truth SvdH JSN Scores

The relationship between predicted JSN scores and reference total JSN scores was analyzed using Spearman’s rank correlation. As shown in Table 25, all models demonstrated statistically significant positive correlations with the clinical JSN scores ( $p < 0.001$ ), indicating that the predicted scores preserved the relative ordering of joint space narrowing severity. The strongest correlation was achieved by EfficientFormer ( $\rho = 0.5986$ ), followed by MobileViT ( $\rho = 0.5765$ ), LeViT ( $\rho = 0.5658$ ), ResNet ( $\rho = 0.5610$ ), and EfficientNetV2 ( $\rho = 0.5580$ ). ConvNeXtV2 showed the lowest correlation among the evaluated models, but still maintained a significant positive association ( $\rho = 0.4792$ ,  $p < 0.001$ ).

These results suggest that the JSN score prediction models capture clinically meaningful ranking information related to joint space narrowing severity. Compared with BE score prediction, the JSN correlations were generally higher, indicating better consistency between model predictions and expert-derived JSN scores. Nevertheless, the correlations remain moderate rather than near-perfect, suggesting that predicted JSN scores should be interpreted as supportive quantitative estimates rather than direct substitutes for expert clinical assessment.

## G Discussion

The benchmark results reveal a consistent performance gap across tasks, indicating that fine-grained pathological analysis remains substantially more challenging than global anatomical modeling. These challenges are fundamentally rooted in both the characteristics of radiographic imaging and the pathological nature of RA.

From an imaging perspective, 2D radiographs inherently suffer from projection-induced ambiguity, limited contrast, and the absence of depth information. From a disease perspective, RA manifests through subtle, heterogeneous, and progressively evolving structural changes, which are often difficult to localize and quantify. These factors jointly impose intrinsic limitations on all downstream tasks.

At the task level, distinct challenges can be observed. For hand bone structure segmentation, although overall performance is high, projection-induced overlap—particularly in anatomically dense regions such as the wrist—significantly obscures boundaries and degrades accuracy in overlap-sensitive regions. In addition, severe structural damage in advanced RA, including bone deformation and collapse, further complicates reliable delineation.

For BE analysis, the primary difficulty lies in the ambiguous and subjective nature of lesion annotation. Erosive lesions are typically small, irregular, and locally indistinct, especially in early-stage RA where radiographic signals are weak. As a result, annotation often depends on expert interpretation, introducing inter-observer variability and uncertainty in the ground truth. This ambiguity limits both the reliability of supervision and the upper bound of achievable performance.

For SvdH-based scoring, additional challenges arise from its semi-quantitative and ordinal nature. The scoring criteria are inherently coarse and subject to interpretation, particularly at boundary levels between adjacent grades. Moreover, the distribution of scores is highly imbalanced, with a long-tail effect where severe cases are relatively rare in modern clinical cohorts. These factors introduce both label ambiguity and data imbalance, making accurate prediction difficult and further weakening the assumption that ground truth labels are fully reliable.

These observations also reflect several limitations of the current evaluation and dataset. Although the dataset is collected from multiple institutions, it remains geographically concentrated and demographically limited, which may affect generalization. Furthermore, the inherent ambiguity in BE and SvdH annotations introduces uncertainty into both training and evaluation, meaning that the provided labels should be interpreted as approximations rather than absolute ground truth. Finally, while multiple tasks are included, they are treated independently, without explicitly modeling the structural and pathological relationships between them, which may limit the ability to capture clinically relevant interactions.

These findings suggest that, despite strong progress in anatomical segmentation, fine-grained pathological analysis remains a key bottleneck for automated RA assessment. Addressing this challenge will likely require improvements not only in model design, but also in data representation, annotation protocols, and task formulation.

## **H Broader Impact**

This work introduces a large-scale, multi-task evaluation and dataset for RA analysis based on hand radiographs. By providing anatomically detailed annotations and clinically grounded evaluation protocols, the dataset has the potential to facilitate the development of computer-aided diagnosis systems that improve the efficiency and consistency of RA assessment. In particular, automated analysis of BE and JSN may assist clinicians in early detection and longitudinal monitoring, which are critical for timely intervention and improved patient outcomes [15]. The public release of such a dataset may also promote reproducible research and lower the barrier for developing structure-aware and clinically interpretable models in medical imaging.

RAM-H1200 is intended for evaluating structure-aware segmentation, lesion-level BE quantification, and joint-level SvdH scoring, but not for evaluating standalone RA diagnosis, treatment recommendation, or deployment readiness across unseen populations. However, several potential risks and limitations should be considered. First, the dataset is collected from a limited number of institutions and may not fully represent the diversity of imaging protocols, populations, and disease presentations encountered in broader clinical practice. Models trained on this dataset may therefore exhibit reduced generalization performance when deployed in unseen environments. Second, annotation of BE and JSN involves inherent subjectivity, particularly in early-stage cases, which may introduce bias into both model training and evaluation. Third, automated systems developed using this dataset should not be used as standalone diagnostic tools, as incorrect predictions may lead to misinterpretation of disease severity and potentially impact clinical decision-making.

To mitigate these risks, we emphasize that this dataset is intended for research purposes and should be used to develop assistive tools rather than replace expert judgment. Future work may incorporate more diverse multi-center data, uncertainty modeling, and human-in-the-loop validation to improve robustness and reliability. Careful evaluation under different clinical settings is necessary before any real-world deployment.